Universidade de Aveiro
Departamento de
Electrónica, Telecomunicações e Informática,
2019

Ana de Resende
Gomes de Pinho

Cintilação Troposférica nas bandas Ka e Q

Tropospheric Scintillation in the Ka and Q bands

Ana de Resende Gomes de Pinho

Cintilação Troposférica nas bandas Ka e Q

Tropospheric Scintillation in the Ka and Q bands

Dissertação apresentada à Universidade de Aveiro para cumprimento dos requisitos necessários à obtenção do grau de Mestre em Engenharia Eletrónica e Telecomunicações, realizada sob a orientação científica da Professora Doutora Susana Mota (co-orientadora), Professora Auxiliar do Departamento de Eletrónica, Telecomunicações e Informática da Universidade de Aveiro e do Professor Doutor Armando Rocha (orientador), Professor Auxiliar do Departamento de Eletrónica, Telecomunicações e Informática da Universidade de Aveiro.

O júri / The jury

Presidente / President	**Professor Doutor Telmo Reis Cunha** Professor Auxiliar da Universidade de Aveiro
Arguente principal / Main examiner	**Professor Doutor Telmo Rui Carvalhinho Cunha Fernandes** Professor Adjunto do Instituto Politécnico de Leiria
Co-orientador / Co-advisor	**Professora Doutora Susana de Jesus Mota** Professora Auxiliar da Universidade de Aveiro

agradecimentos / acknowledgements

Em primeiro lugar gostava de agradecer ao professor Armando Rocha pela incansável orientação durante a elaboração desta dissertação e por todo o tempo que despendeu a ajudar-me. Agradeço também à professora Susana Mota por toda a atenção e ajuda que me prestou nesta etapa. Agradeço ao Departamento de Electrónica, Telecomunicações e Informática e ao Instituto de Telecomunicações de Aveiro pelas condições de trabalho proporcionadas.

À minha mãe e ao meu pai, o maior obrigado do mundo, por me mostrarem o verdadeiro significado da palavra resiliência.

À minha avó Célia e ao meu avô Zé por provarem todos os dias que a felicidade está nas pequenas coisas da vida.

À minha família Resende que me acompanhou sempre e que mostrou que a união faz a força. Em especial, à Alice e à Rita por tudo.

Por último, um agradecimento especial a todos os meus amigos e colegas que me ajudaram de uma forma ou de outra durante o meu percurso académico.

Palavras chave Cintilação, Banda Ka, Banda Q, Interferências construtivas e destrutivas do sinal.

Resumo

O aumento das comunicações via satélite tem sido um fenómeno global e continuado. Com este crescimento e o aumento da demanda dos consumidores por novas tecnologias com taxas transmissão de dados superiores levou à necessidade de um estudo detalhado do canal de propagação a frequências cada vez mais elevadas.

Esta dissertação pretende estudar um fenómeno, chamado cintilação, que os sinais de rádio sofrem ao atravessar a atmosfera. Este estudo usa como suporte experimental dois sinais distintos medidos em Aveiro: um na banda Ka e outro na banda Q. Os dados experimentais foram recolhidos de 2016 até agora, sendo que foram reunidos cerca de 20 GB de dados.

A teoria de suporte do fenómeno de cintilação é apresentada para que se possa entender a sua origem e influência nos sinais propagados. A campanha experimental recolheu medidas de amplitude a 8 amostras/s as quais foram processadas com o objetivo de extrair a cintilação.

A cintilação é a base de toda análise feita nesta dissertação. Alguns parâmetros de cintilação são comparados com modelos já bem conhecidos da literatura. Adicionalmente, este trabalho estabelece uma relação entre o comportamento da cintilação com parâmetros meteorológicos e sua variação a curto e longo prazo. Estudaram-se ainda as distribuições estatísticas dos desvanecimentos e dos reforços do sinal de cintilação. Os desvanecimentos podem impactar negativamente a qualidade do sinal recebido.

Keywords Scintillation, Ka-band, Q-band, Fade, Enhancement.

Abstract

The growth of satellite communications and the demand for services with higher bandwidth and adequate quality of service requires higher frequencies and the research on the propagation channel has become a necessity.

This dissertation intends to study an impairment phenomenon, named scintillation, that radio signals suffer crossing the earth's atmosphere. The study is supported experimentally by a set o propagation data collected in Aveiro: one at the Ka-band and other at the Q-band. These experimental data have been collected from 2016 until now and the total volume of data is about 20 GB.

The theory behind scintillation is presented, in order to understand its physical basis and the influence on the signals. Experimental measurements were conducted to collect the signals amplitude at 8 S/s and process them with the aim of extracting the final scintillation signal.

This signal is the base of every analysis done in this dissertation. The measured scintillation parameters are compared with some well-known models from literature. Additionally, this work establishes a relation between scintillation behavior with meteorological parameters and their correlation in a short and long term basis. The fades and enhancements distributions of the scintillation were calculated. The fades distribution can negatively impact the CNR at the reception.

Contents

List of Figures

List of Tables

List of Acronyms

CCDF Complementary Cumulative Distribution Function

CDF Cumulative Distribution Function

CPA Copolar Attenuation

CNR Carrier-to-Noise Ratio

DLPC Downlink Power Control

DETI Departamento de Electrónica Telecomunicações e Informática

DRR Data Rate Reduction

EIRP Effective Isotropic Radiated Power

ESA European Space Agency

FD Frequency Diversity

FMT Fade Mitigation Techniques

FSS Fixed Satellite Service

HC Hierarchical Coding

HM Hierarchical Modulation

ITU - R International Telecommunication Union - Radiocommunication Sector

IT-Av Instituto de Telecommunicações-Polo de Aveiro

OD Orbital Diversity

OMT OrthoMode Transducer

PDF Probability Distribution Function

PIMTS Propagation Impairment Mitigation Techniques

SBS Spot Beam Shaping

SD Site Diversity

TD Time Diversity

ULPC Uplink Power Control

USAT Ultra Small Aperture Terminal

VSAT Very Small Aperture Terminal

XPD Cross-Polarization Discrimination

List of Symbols

χ	Scintillation amplitude	(dB)
χ^+	Scintillation amplitude positive values - Fades	(dB)
χ^-	Scintillation amplitude negative values - Enhancements	(dB)
σ_χ^2	Scintillation variance	(dB^2)
σ_χ	Scintillation intensity (standard deviation)	(dB)
σ_{pre}	Reference standard scintillation with antenna and link contributions	(dB)
σ_{ref}	Reference standard deviation in scintillation models	(dB)
σ_{tm}^2	Variance induced by the thermal noise	(dB^2)
θ	Antenna elevation angle	$(^\circ)$
N	Radio refractivity	(ppm)
N_{dry}	Dry radio refractivity	(ppm)
N_{wet}	Wet radio refractivity	(ppm)
n	Refractive index	
n	Scintillation spectrum slope	
RH	Relative humidity	(%)
T	Temperature	$(^\circ C)$
ρ	Water vapour density	(g/m^3)
e	Pressure of the water vapour content	(hPa)
P_d	Dry pressure of the atmosphere	(hPa)
P	Total pressure of the atmosphere	(hPa)
h	Turbulence height	(m)
f	Frequency	(Hz) or (GHz)
k	Wavenumber	(m^{-1})
k_0	Free-space wavenumber	(m^{-1})
λ	Wavelength	(m)
$W_\chi(f)$	Power spectral density	(dB^2/Hz)
V	Sphere volume	(m^3)
ϵ_0	Medium dielectric constant	
ϵ_r	Relative dielectric constant	
a	Sphere radius	(m)
L_0	Input range dimension	(m)
l_0	Dissipation range dimension	(m)
C_n^2	Refractive index structure constant	$(m^{-\frac{2}{3}})$
$D_n(\rho)$	Refractive index structure function	
L	Path length from earth to turbulence	(m)
F_n	Fresnel radius	(m)

$R(\tau)$	Auto-correlation function	
f_s	Scintillation frequency	(Hz)
f_0	Fresnel frequency	(Hz)
f_c	Corner frequency	(Hz)
G(x)	Smoothing gain	
D_e	Effective antenna diameter	(m)
D	Antenna physical diameter	(m)
η	Antenna aperture efficiency	(%)
a_e	Earth's effective radius	(m)
v_t	Wind transverse velocity	(m/s)
f_a	Sampling frequency	(S/s)
P	Time percentage	(%)
W_{hc}	Average water content of heavy clouds	(kg/m^2)

Chapter 1

Introduction

1.1 Motivation

Millimetre wave propagation studies remain a matter of great interest, based on the exponential evolution in the use of satellite communications and the renewed interest in the framework of the use of millimetre waves in 5G as a (but not only) space segment.

The frequency band congestion of the reserved bands for satellite communications, L (1 /2GHz), S (2/4 GHz), C (4/6 GHz), X (8/12 GHz), Ku (12/18 GHz) and Ka (26/40 GHz) highlights even more the interest in the choice of high frequencies, as an alternative [3]. The development of microwave circuits and antennas technology are opening the exploration of the higher frequencies Q/V bands where the bandwidth is more generous and so opens the possibility of providing services requiring high data rates.

The satellite solution is evolving with the increasing use of Medium Earth Orbit (MEO) and also the Low Earth Orbit (LEO) satellites whose costs are significantly lower than the Geosynchronous Equatorial Orbit (GEO) ones. These lower orbits provide significantly shorter path delays opening new markets where shorter latency is required. The use of satellites can also be a part of the arriving 5G mobile communications to provide an extended coverage even in very remote zones [4].

However, the use of millimetre waves, either on satellite or terrestrial communications in general (with the increased interest in the 5G) [5] are subject to increased impairments [6] due to gases attenuation (often slowly varying), clouds or fog and the sporadic occurrence of rain. These atmospheric phenomena have an increased impact on the received noise, received signal amplitude, interference with other systems, depolarization and fluctuations of the amplitude, being this last one caused by refractive index irregularities in the always turbulent atmosphere. These effects are more acute at higher frequencies so usually a given quality of service cannot be achieved by just implementing fade margins.

The above impairments must be characterized from several viewpoints either to make adequate link budgets and provide an estimation of the quality of service, or to design propagation impairment mitigation techniques that can reduce the impact of the propagation channel. Several experiments have been made, mainly in Europe and often supported by the European Space Agency (ESA), along the years to characterize experimentally the atmospheric propagation channel that surely has a substantial climate dependence and so deserves large scale propagation campaigns. To cite a few, we can recall the measurement campaigns with the OTS satellite [7], the Olympus satellite (with 3 beacon frequencies) [8] and the ITALSAT

satellite [9] with beacons at 40 and 50 GHz. However, this last experiment had a very limited participation.

The propagation channel models have been, along the successive experiments, developed, tested and improved. Such models involve not only static aspects of the channel – percentage of the time a certain propagation parameter has been exceeded- but, as well, the dynamic aspects such as fade duration, rate of change of attenuation, etc. One aspect that has not been addressed so frequently, also because experimental data is scarce, is the scintillation phenomena: the scintillation, is a non-absorptive phenomena characterized by the fluctuation of the signal around an average amplitude that has a relatively high frequency spectral content in this context (up to 1 to 2 Hz when compared to about 0.01 to 0.025 Hz of the fades induced by rain). The scintillation can cause adverse effects in satellite communications availability and disturb propagation impairment mitigation techniques.

At the location of Aveiro, known by IT-Av for projects, two propagation beacons are being measured along the last 3 years in two converging links. One beacon is the Q-band beacon (39.402 GHz) radiated by the Alphasat satellite and, the other one, is a Ka-band beacon (19.68 GHz) radiated by the Ka-Sat satellite. This thesis is devoted to the analysis of the scintillation phenomena measured in this two links.

1.2 Structure

This dissertation is structured in 7 chapters. The present chapter gives a brief explanation why scintillation is important and why deserves to be studied.

Chapter 2 starts by introducing the propagation effects caused by the atmosphere and emphasizes scintillation; follows with a description of the main meteorological parameters that are relevant for the propagation phenomena in general, adding more details on the characterization of scintillation; and ends with a description of the techniques used to mitigate the propagation effects.

Chapter 3 goes deeper on the theory behind scintillation: it is explained what is scintillation in a mathematical and physical basis. Briefly, the general scattering theory is addressed and put in context with scintillation. The scintillation spectrum is also described in this chapter.

Chapter 4 explores details on the available models to predict scintillation and gives further information about their implementation. In addition, it is included a section with the statistical theory behind this subject.

Chapter 5 presents preliminary experimental results, beginning with a description of the equipment that supports the study. Here, it is portrayed all the data that runs through the system and the process how scintillation is extracted from the input signal and how it is stored.

Chapter 6 is dedicated to the scintillation analysis. It starts by relating the meteorological parameters with the scintillation standard deviation. Then, the scintillation parameters distribution is studied for the two frequencies bands, compared with models and some conclusions are drawn. The scintillation diurnal behaviour is explored in detail. It is followed by the study of the scintillation frequency scaling and its spectrum. The spectral study rises a deeper analysis of the wind velocity impact on scintillation.

Chapter 7 is the last and gives an overview of all results. Here, conclusions are presented and possible guidelines for future work are drawn.

1.3 State of the art

The scintillation is still a weakly characterized phenomenon and plays an important role in telecommunications systems, because, it conditions the cumulative distributions of attenuation or impact the calculation of the link budgets. The phenomena cannot be studied together with attenuation, because, the physical mechanisms that cause them have a substantially different dynamics. Thus, attenuation and scintillation are modelled independently, and their impact on attenuation statistics is performed later, as it can be seen in the ITU model [10].

Most of the scintillation results are presented in a simple statistical form to characterize the amplitude and the standard deviation. The effort to analyze hourly variability and spectrum characterization has been limited. The experimental arrangement of having two converging links at the receiving point is also a differentiating aspect of this work.

On the other hand, the existing models are almost always anchored in the same dependence on wet index of refraction of the atmosphere: an approximation that requires probably a refreshment. This dissertation focuses, in a first stage, in the evaluation of some experimental models for the amplitude and standard deviation distributions, to evaluate their suitability to our climate. Also, except for a few papers, certain aspects of the scintillation spectrum such as the roll-off factor and the corner frequency have not been subject to a detailed analysis. The analysis of such parameters in two converging links with concurrent data seems not to have been done. Also, the autocorrelation of the scintillation intensity has not been addressed, in spite of being a parameter that can last several hours and repeat itself along several days.

The cross correlation of the scintillation intensity at the two links is also explored and, as far as it is known, this has not been the subject of any previous analysis.

Chapter 2

Millimeter wave propagation

2.1 Introduction

The aim of this chapter is to give an overview of the impairments that the electromagnetic waves encounter during its propagation through the troposphere in slant paths. The first section begins by explaining, qualitatively, the main effects that the troposphere causes on electromagnetic waves, such as: the attenuation; depolarisation; and, scintillation. The following section (2.3) describes the most important meteorological parameters that affect the wave propagation and, consequently, deserve complementary measurements. The propagation impairment mitigation techniques (PIMTS) that are available to counteract the aforementioned effects, are briefly described, also in this chapter.

2.2 Troposphere effects on electromagnetic waves propagation

At frequencies higher than 10 GHz some meteorological phenomena occurring in the troposphere have a great impact on electromagnetic waves [11]. Wave interactions with hydrometers - like rain drops, cloud droplets or hail - cause energy absorption and scattering that reduces the wave amplitude and changes the polarisation of the signal.

For an Earth-space path the most relevant impairments for propagation loss are:

- Attenuation;
- Depolarisation;
- Scintillation.

This section describes briefly the three phenomena listed above.

2.2.1 Attenuation

Atmospheric gases have usually a minor contribution to attenuation that is mostly caused by precipitation and clouds. However, with the frequency increase and lower elevation angles, atmospheric gases must be considered for systems with low attenuation margin, such as, very small aperture terminal (VSATs). The oxygen and water vapour are the main gases contributing to the attenuation. The water vapour molecules have a local absorption peak close to 22.2 GHz, on the other hand, oxygen has also a local absorption peak at 60 GHz due to

a complex resonance of the oxygen molecule (just referring frequencies below 100 GHz). The recommendation ITU-R P.676-9 gives the necessary instructions to estimate these attenuation contributions [10].

Attenuation due to hydrometers, such as rain, clouds, fog and snow, are due essentially to the power absorption at lower microwave frequencies but, at higher, frequencies the scattering contribution becomes also important [1].

For high fade margin systems, rain attenuation is the dominant impairment. However, for low margin systems and higher frequencies, clouds and scintillation represent, as referred above, an important impairment [12].

Clouds and fog consist of suspended droplets of liquid water, named as hydrosols. Hydrosols attenuation is more severe for systems operating above 20 GHz. Clouds can be made either of water droplets or ice particles. However, ice contribution for attenuation is usually neglected as the ice dielectric constant is mostly real. The main focus is on the almost spherical water droplets with a diameter less than 100μm [12]. The interaction of the wave with these drops can be estimated through the Rayleigh scattering theory, at least up to 40 GHz.

Another possible impairment is multipath propagation observed for very low elevation angles and special atmospheric conditions. This can cause severe amplitude variations with very deep fades.

Ultimately, the dominant impairment above 10 GHz is caused by rain. Rain is a complex mix of several families of drops with distinct radius, shapes and orientations that change from rain event to rain event and from climate to climate. Several models are used to predict rain attenuation but, in this section, only the ITU-R Rain Attenuation Model [10] is referred since it is the most widely accepted and tested.

2.2.2 Depolarisation

Polarisation of an electromagnetic wave specifies the geometrical orientation of the wave oscillations. In general, the polarisation direction is given by the electric field vector.

In satellite communications, another impairment is depolarisation, which means, that some power of the original (transmitted) polarisation is transferred to the orthogonal polarisation [1][12]. The signal received in the same polarisation of the transmitted one is called copolar and the one received in the orthogonal polarisation is called crosspolar.

Depolarisation is basically the modification of the radiowave polarisation, caused by a population of non spherical hydrometeors with a preferred orientation, such as rain and ice particles (for frequencies above 3 GHz), as can be seen in Figure 2.1. Such propagation medium has two principal orthogonal planes that it will not cause depolarization if the electric field is aligned along these planes. However, due to the distinct propagation constants along these planes, any other wave will be depolarized. This phenomenon generates interference or crosstalk between channels, in systems using the same frequency and two orthogonal polarization's to double the capacity [12].

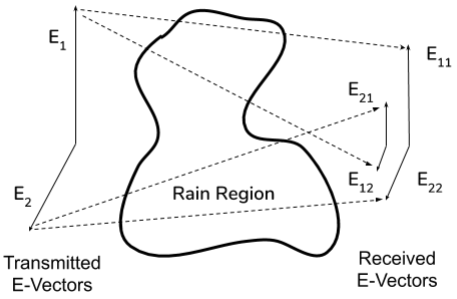

Figure 2.1: XPD illustration for differential attenuation.

The depolarization is often characterized by the depolarization ratio -relationship between the received amplitude in the crosspolar channel and the copolar channel amplitude- or the the corresponding value in logarithmic units being called, *XPD* (crosspolar discrimination).

$$XPD = -20 \log \left(\frac{A_{cx}}{A_{co}} \right) \quad (dB) \tag{2.1}$$

where A_{cx} and A_{co} are the electrical field amplitudes, respectively, for the cross-polar polarization (undesired) and for the original polarization (desired).

The rain causes depolarization because the falling rain drops became distorted: they assume an oblate shape and the minor axis of the drop can be tilted (canting angle) from the vertical due to the vertical wind gradient. The distortion, often characterized by an axial ratio, depends of the size of drops. Such medium, has distinct propagation constants - specific attenuation and phase constant - along the minor axis and the orthogonal one (as mentioned above). Therefore, the *XPD* is a complex function of the link parameters and the raindrop size distribution found along the propagation path.

Another source of depolarization comes from the ice crystals that only cause differential phase shift along the aforementioned principal planes. Ice crystals sizes range from 0.1 to 1 mm and are usually modelled as dishes or needles that are aligned in the horizontal plane, with the needles randomly oriented in this plane. However, electric fields in thunderstorms can cause preferred orientation of the needles in the horizontal plane, giving rise to fast changes of the XPD.

2.2.3 Scintillation

As an electromagnetic wave travels an atmospheric turbulent path, from the satellite to the earth receiver, it crosses air masses with different values of temperature, humidity and pressure that are evolving with time. All these turbulent mixing of air masses with different characteristics lead to random variations of the refractive index of the medium. At the receiver antenna aperture the wave front arrives distorted in phase and amplitude, leading to fluctuations of the received signal around a mean value that is called scintillation (as referred above). The amplitudes above the mean value are called enhancements and the ones below are called fades.

Next, the refractive index of the clear sky atmosphere is discussed.

Refractive Index

As mentioned before, the index of refraction, $n(r,t)$ is a function of time and space. Its temporal dependence is related to the mixing dynamics of the air masses and the wind. Besides that, its spatial structure and evolution is based on fluid mechanics laws. Hence, some kind of structural description of this medium, surely in a statistical basis, is needed before some electromagnetic related parameters are introduced. In this section a description of the relation between atmospheric parameters and the refractive index is presented.

The index of refraction is given by:

$$n = \sqrt{\varepsilon} = \frac{c}{v} \tag{2.2}$$

where ε is the dielectric constant of the medium: in this case, the atmosphere. The constant c is the speed of light in the vacuum and, finally, v is the speed of the wave in the medium. At the Earth surface, n is close to unity: around 1.00025 and 1.00040 [13]. A practical way to address n is to use the scaled quantity called the radio refractivity N:

$$n = 1 + N \times 10^{-6} \tag{2.3}$$

The refractivity, N (in parts per million) is given by:

$$N = 77.6\frac{P_d}{T} + 72\frac{e}{T} + 3.75 \times 10^5 \frac{e}{T^2} \tag{2.4}$$

where,

P_d: dry pressure of the atmosphere (hPa)

P: total pressure of the atmosphere (hPa)

e: pressure of the water vapour content (hPa)

T: absolute temperature (K).

The first term of N represents the dry contributions to N:

$$N_{dry} = 77.6\frac{P_d}{T} \tag{2.5}$$

that is due to an almost constant contribution of the essentially constant atmosphere composition. The remaining terms are due to the water vapour component that is variable. This contribution is called N_{wet} and it is very important for this dissertation because it introduces the time and space variability of the refractivity.

$$N_{wet} = 72\frac{e}{T} + 3.75 \times 10^5 \frac{e}{T^2} \tag{2.6}$$

The index of refraction varies with the altitude:

$$n(h) = 1 + N_0 \times 10^{-6} \times e^{-\frac{h}{h_0}} \tag{2.7}$$

N_0: radio refractivity average value at sea level

h_0: the corresponding height in kilometres.

The reference values, which depend on the type of climate, are [10]:

$$N_0 = 315$$
$$h_0 = 7.35 \text{ km}$$

Paying attention to equation (2.7) we can easily confirm that *n(h)* decreases with the altitude because the atmosphere becomes less dense. For this reason, scintillation is stronger in lower altitudes of the troposphere, and also, because the atmosphere is not able to retain so much water vapour with low temperatures as it could at the Earth surface. Therefore, even when turbulence originates from a higher level of the atmosphere, differences between refractive indexes due to adjacent air masses are insignificant in comparison with the differences at the atmospheric boundary layer [14].

2.3 Meteorological phenomena

Most of the atmospheric phenomena impacting millimetre wave propagation comes from several type of hydrometeors, which can be observed as precipitation. Therefore, hydrometeors are particles of water (liquid or solid) formed in the troposphere with dimensions ranging from small droplets to large hail stones [15]. Figure 2.2 shows the different types of hydrometeors and respective sizes.

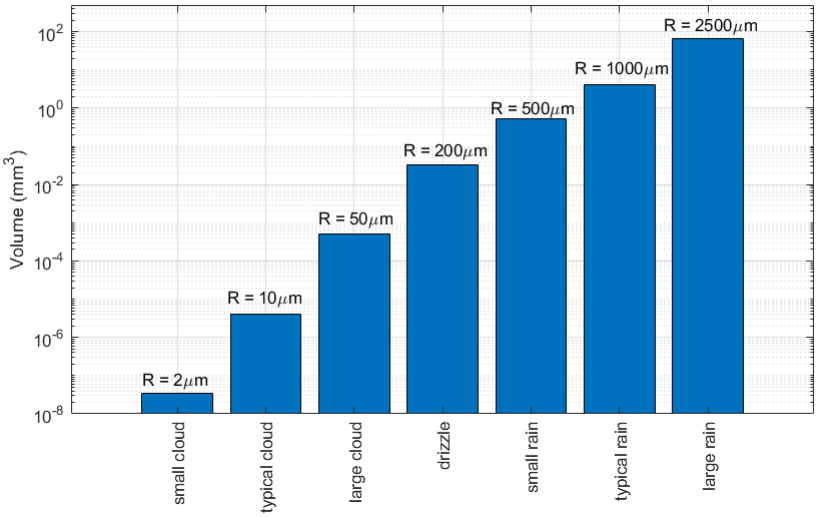

Figure 2.2: Types of hydrometeors and corresponding radius, R.

A detailed description of the hydrometeors types is now given.

2.3.1 Clouds

Clouds formation occurs when air reaches its saturation point and, tiny particles of ice or water become suspended in the atmosphere due to the drag and rising air forces. The saturation point corresponds to the maximum amount of water vapour that air can contain at a certain temperature. The processes that cause this saturation are the cooling of the air and the increase of the water vapour. Clouds can be characterised according to their aspect,

the altitude at which they occur, the size, number and spatial distribution of their particles and wind fields in the atmosphere, as displayed in Table 2.1.

Table 2.1: Differentiation of cloud types [2].

	Altitude	**Composition**
Cirrus, cirrostratus	>6000 m	ice crystals
Altostratus, altocumulus	from 2000 m to 6000 m	droplets of water or ice, if the temperature is low enough
Stratocumulus, nimbostratus	<2000 m	water droplets
Cumulus, cumulonimbus	Vertical development	droplets of water or ice

2.3.2 Fog

Fog formation is based on the same principles of the clouds formation. The main difference between them is their relative altitude. Clouds have their base above the Earth's surface, while fogs have their root at ground level. The ideal conditions for fog formation are the relative humidity being near to 100 percent and horizontal visibility reduced to below one kilometre. Horizontal visibility is the maximum distance that an object can be seen and identified with the naked eye. Beyond this distance, it urges to use the aid of measuring equipment, employing either a transmissometer or a diffusiometer [11].

Clouds and fog can be very important for low elevation links and are particularly important at very high frequencies, mainly for free space optical communications that are now being explored in the context of 5G [16]. The effect of the fog on signal attenuation is only significant from frequencies above 100 GHz [11], a range that is out of the scope of this dissertation.

2.3.3 Precipitation

Precipitation occurs when the hydrometeors suspended in the clouds are heavy enough to fall and, and these usually larger droplets, are developed by a collision-coalescence process and the Bergeron process [2]. The collision-coalescence is caused by an aggregation process due to drops collision.

The droplets size growth is proportional to the time spent in the cloud. The larger the cloud and the greater the upward air current, the longer the droplets will stay in the cloud.

"Hot" clouds are clouds whose temperature is greater than $0°C$. In tropical regions this type of clouds is very common and causes large periods of precipitation. They are exposed to strong upward wind currents that "push" the drops in altitude. The drops at an higher altitude will spend more time in the cloud and will grow in size through successive collisions.

Unlike "hot" clouds, "cold" clouds lie at a much higher altitude with temperatures of about $40°C$ negative. Precipitation formation is based on the Bergeron phenomenon [17] where ice crystals grow overtime with the aggregation of water droplets in their vicinity (accretion).

Thus, regardless of the type of cloud, the higher the cloud, the longer time has the hydrometeor to grow resulting in higher rain rates.

2.3.4 Rain

The fall of particles of water in the liquid state is called rain. Figure 2.3 shows that the rain drops have radius size close to 2 mm and the particles in the clouds about 0.02 mm

[15]. The small cloud droplets can increase their size by a hundred times through the process of coalescence, aggregation or accretion. In the case of rain only the coalescence process is relevant, the rest portray the precipitation of particles in the solid state.

Rain plays a key role in the water cycle; it is responsible for returning water to the ground.

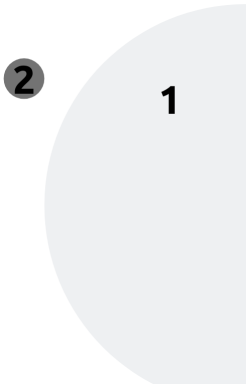

Figure 2.3: Representation of the relation between sizes of the water droplet (1) and the constituent droplet of the cloud (2).

The rain rate is measured in mm/h by rain gauges using several types of sensors: optical, ultrasound and mechanical (drop counter, tipping bucket, impact). The rain can be classified, based on its occurrence, in two categories:

- Stratiform: weak rainfall occurring in large areas;
- Convective: very brief and intense rain in small areas.

2.3.5 Hail, ice and snow

For temperatures below a certain value, the hydrometeors change from their liquid state to the solid state. It should be noted that the droplets in the atmosphere can remain in the liquid state at temperatures significantly below $0°C$.

The hail originates from the cumulonimbus clouds where, by accretion, the ice pellets reach a considerable size to precipitate. Solid ice stones can either be transparent or partially opaque and of variable size and density. Its size can vary between that of a pea and a golf ball [2].

2.4 Propagation impairment mitigation techniques (PIMTS)

As the satellite industry develops the usage of VSAT/USAT increases. This kind of systems belong to the Fixed Satellite Service (FSS) that now demands for higher frequency bands. The characterization of the impairments, for the higher frequency spectrum, is essential to develop methods that can ensure the quality of service, which the customer demands. For frequencies above 10 GHz, several fade mitigation techniques (FMT) must be adopted [18].

These are split into three categories:

- EIRP control techniques;

- Adaptive transmission techniques;
- Diversity protection schemes.

Briefly, all of the three techniques have in common some functionalities: all of them sense the link quality, based on the measurements of the propagation conditions, and then adjust some of the link characteristics. A comprehensive report on such systems can be found in [19].

The first type of techniques mentioned, simply adjust the carrier power or the antenna gain, in order to compensate the power losses due to propagation effects. When the EIRP control technique is carried out on board of the satellite, is called a downlink power control (DLPC). For the opposite situation, the technique is known as uplink power control (ULPC), i.e., when it is applied in the ground, at the earth station. Another technique, which takes advantage of the adjustment of the antenna gain and is also applied on-board the satellite, is the spot beam shaping (SBS).

The second category of techniques, instead of focusing on the carrier power/ antenna gain variation, modifies the signal processing or transmission, where the link has been compromised. This category is split into other three categories:

- Hierarchical coding (HC);
- Hierarchical modulation (HM);
- Data rate reduction (DRR).

The last type of FMTs explores the limited size of rain cells and consists of switching to another satellite or other ground station separated by a few km. This category is divided into, site diversity (SD) or orbital diversity (OD), which are dependent on the type of rain occurring at the site. Changing to a lower frequency -frequency diversity (FD)- or repeating the message later -time diversity (TD)- are two other techniques.

Chapter 3

Scintillation

A brief description of the atmosphere, that is the transmission channel used on satellite communications, was made in the previous chapter. It is essential to understand the effects of the atmosphere on an electromagnetic wave. Being the atmosphere in constant change, even when no liquid or frozen water is observed (rain, fog, clouds, etc), the random fluctuations of the dielectric constant of atmosphere will, surely, cause random fluctuations of the received signal in amplitude and phase: this phenomenon is called scintillation (phase fluctuations are more difficult to measure than amplitude ones). The propagation through this random continuum medium was addressed mainly by Chernov (1960) and Tatarski (1961).

Therefore, in this chapter we introduce this propagation topic, whose theory is quite complex because it involves fluid mechanics and the solution of Maxwell equations in random media. Section 3.1 introduces the scintillation and its parameters, section 3.2 describes the interaction of an electromagnetic wave with a particle, section 3.3 summarizes the basic theory of the propagation crossing a turbulent medium and section 3.4 details the description of the turbulent medium and how it impacts the scintillation. Scintillation characterization starts in section 3.5 with a description of the scintillation variance, followed by section 3.6 with the spectral behaviour of the scintillation amplitude.

3.1 Scintillation characterization

According to the previous chapter, turbulence affects millimeter wave propagation by amplifying and reducing the wave intensity arriving to the antenna and by scattering some power outside the incident beam direction. As a result, the signal received strength suffers fast fluctuations (with respect to other effects such as rain attenuation), called scintillation [20]. In the time domain, this phenomenon is characterized by rapid fluctuations in amplitude and phase due to the sum of a number of uncorrelated contributions along the medium [20].

At the Earth station, the signal amplitude is $A(t)$ and, under clear sky conditions, A_0 is the mean signal level. The scintillation amplitude is given by [21]:

$$\chi(t) = 20log_{10}\left(\frac{A(t)}{A_0}\right) \quad (dB) \tag{3.1}$$

This approach, describes scintillation as a log-amplitude variation χ, in dB, through the ratio of the signal amplitude and the mean amplitude.

As an illustration, Figure 3.1a gives an example of an event occurring in May 12^{th}, 2018 collected at the Q-band and Ka-band by the AlphaSat and Ka-Sat receivers, respectively. It is noticeable, the amplitude fluctuating around a zero mean value. Amplitude values above the mean are called *fades* and values bellow the mean value are called *enhancements* (following the pre-processed data). Some authors also characterize the phenomena by using the peak-to-peak amplitude in fixed time windows: from 1 to 5 minutes. In this relatively long lasting event (5 minutes) the peak-to-peak variations were 2.84 dB.

Another parameter used to characterize the scintillation phenomena is the standard deviation, σ_χ (dB) (also called scintillation intensity) or the variance, σ_χ^2 (dB^2) of the log-amplitude fluctuations usually calculated in 1 to 5 minutes time windows. Theoretical expressions that relates the variance with properties of the turbulent medium in certain conditions of well-developed turbulence are described in a following section. As an example, Figure 3.1b shows the scintillation variation for a selected 5 minutes period.

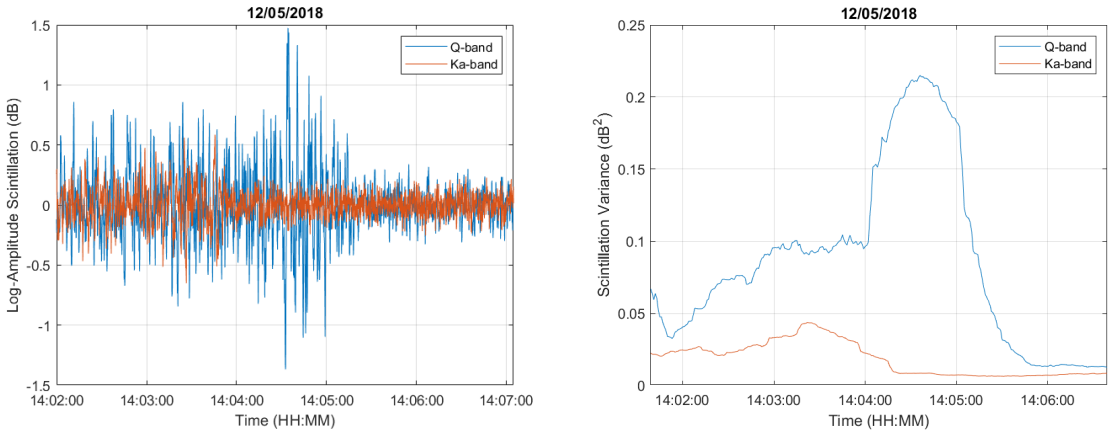

(a) Log-amplitude scintillation during 5 minutes. **(b)** Scintillation Variance during 5 minutes.

Figure 3.1: Scintillation during 5 minutes.

Following the time domain analysis, a spectral characterization of the phenomena is also used by computing the power spectral density $W_\chi(f)(dB^2/Hz)$ of the amplitude fluctuation χ. Usually the scintillation spectrum is calculated in 1 to 5 minutes sliding time windows during stationary periods of the phenomenon, which must not be shorter than 10 minutes. As an example, the spectrum depicted in Figure 3.2 was calculated using a Welch's power spectral density estimator with 10 minutes segments applied to two concurrent 30 minutes time series at Q-band and Ka-band [22].

The spectrum exhibits a typical trend that is predicted by the theory: a flat value up to 0.3 to 0.4 Hz; and then, a linear decay followed by a new irreducible ground floor, which is due to the measurement noise floor of the equipment. It can be observed the higher intensity of the phenomenon at Q-Band.

Further, in this chapter, a detailed description of scintillation's spectrum is presented.

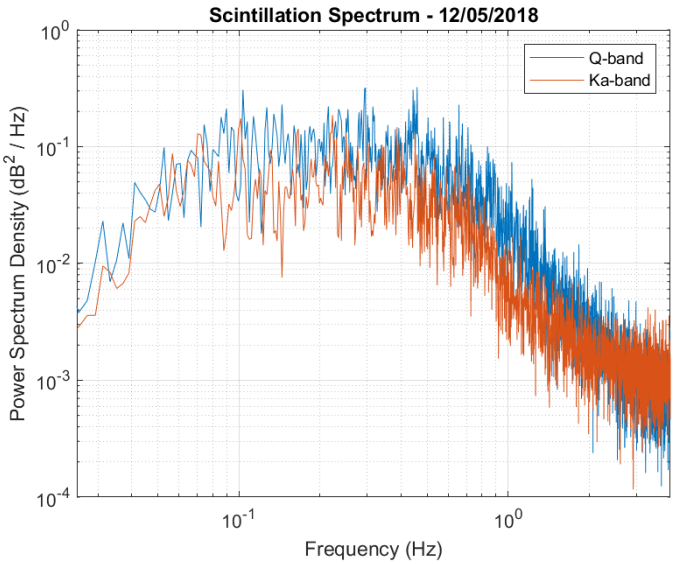

Figure 3.2: Scintillation Spectrum.

3.2 Scattering theory

In satellite communications, the electromagnetic wave traveling through the atmosphere faces adverse conditions due to the interaction with particles. The wavefront induces electromagnetic fields in the particle that acts like a lossy antenna: some of the power of the wave is absorbed inside the particle and some is scattered, that is, radiated in all directions. The wavefront intensity is, consequently, reduced ahead of the particle. The scattering phenomenon depends on the size, shape, frequency and dielectric constant of the particle.

In the presence of a scatterer, the electromagnetic fields at the position $\mathbf{r}$ are described by the following equation:

$$\mathbf{E}(\mathbf{r}) = \mathbf{E_i}(\mathbf{r}) + \mathbf{E_s}(\mathbf{r}) \tag{3.2}$$

$$\mathbf{H}(\mathbf{r}) = \mathbf{H_i}(\mathbf{r}) + \mathbf{H_s}(\mathbf{r}) \tag{3.3}$$

where, $\mathbf{E_i}(\mathbf{r})$, $\mathbf{H_i}(\mathbf{r})$ are the incident wave fields and $\mathbf{E_s}(\mathbf{r})$, $\mathbf{H_s}(\mathbf{r})$ are the scattered wave fields.

The scattering occurring in a single particle, surrounded by a medium with dielectric constant ε_0, is geometrically represented in Figure 3.3.

An incident plane wave going along the $\mathbf{u_i}$ direction, has an incident field with E_i amplitude:

$$\mathbf{E_i}(\mathbf{r}) = E_i \mathbf{u_e} e^{jk_0 \mathbf{u_i} \cdot \mathbf{r}} \tag{3.4}$$

where, $\mathbf{u_e}$ defines the wave polarization, k_0 is the free-space wavenumber and $\mathbf{r}$ is the vector from the particle to the observer.

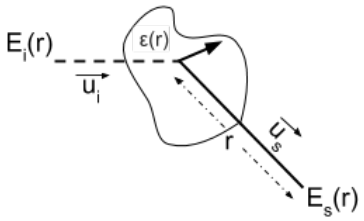

Figure 3.3: Scattering of a single particle.

The observer is considered to be in a far-field zone of the particle if the following condition is verified:

$$r > \frac{2l^2}{\lambda} \tag{3.5}$$

where λ is the wavelength and l is the diameter of the particle. The scattered field, assuming $E_i = 1$ is given by:

$$\mathbf{E_s}(r) = \mathbf{f}(\hat{\mathbf{u}}_\mathbf{s}, \hat{\mathbf{u}}_\mathbf{i})\frac{e^{jk_0 r}}{r} \tag{3.6}$$

The function $\mathbf{f}(\hat{\mathbf{u}}_\mathbf{s}, \hat{\mathbf{u}}_\mathbf{i})$ is generally known as the scattering amplitude and its value can be obtained from the calculations of the scattered field [23]. A closed form expression for the scattering amplitude can be obtained but it requires to know the fields inside the particle. The complexity of the determination of the field inside the particle led to a few approximations that are often enough, otherwise, except for a sphere, a numerical computation must be performed. An interesting case is the scattering of a sphere that has been studied by Mie [24]. Mie developed a theory that gives the scattering amplitudes for an arbitrary sized sphere, but, involves the calculation of special functions that can reach a very high order for large particles if a good accuracy is needed. If the particle size is much larger than the wavelength the geometrical optics approach can be used. Now, the most used approaches and their range of validity to calculate the scattering of a sphere, or eventually other shape, are described.

3.2.1 Rayleigh scattering

When particles are much smaller than the wavelength λ, the Rayleigh approximation can be used up to a radius $a = 0.05\lambda$ ($k_0 a < 1$) [23].

The electric field E inside the particle can then be approximated by the electrostatic formulation [25] and is given by:

$$\mathbf{E} = \frac{3}{\varepsilon_r + 2}\mathbf{E_i} \quad \mathbf{E_i} = \mathbf{u_e}E_i \tag{3.7}$$

where $\mathbf{u_e}$ is the unit vector in the direction of the incident wave polarization.

The scattering amplitude function is given:

$$\mathbf{f}(\mathbf{u_s}, \mathbf{u_i}) = \frac{k_0^2}{4\pi}[-\mathbf{u_s} \times (\mathbf{u_s} \times \mathbf{u_e})]\frac{3(\varepsilon_r - 1)}{\varepsilon_r + 2}V \tag{3.8}$$

where V is the volume of a sphere with radius a:

$$V = \frac{4\pi a^3}{3} \tag{3.9}$$

After simplifying the vector cross products, note that $[-\mathbf{u_s} \times (\mathbf{u_s} \times \mathbf{u_e})] = \sin\alpha$ the scattering amplitude is given by:

$$\mathbf{f}(\mathbf{u_s}, \mathbf{u_i}) = \frac{k_0^2}{4\pi} \frac{3(\varepsilon_r - 1)}{\varepsilon_r + 2} V \sin\alpha \tag{3.10}$$

where α is the angle between $\mathbf{u_e}$ and $\mathbf{u_s}$ and is measured from the direction of the electric field: that is the scattering amplitude pattern follows a Hertz dipole radiation diagram. Figure 3.4 shows this relation.

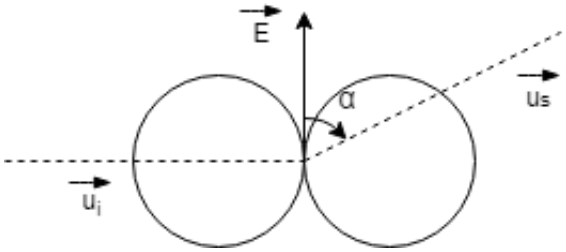

Figure 3.4: Dipole radiation pattern.

It is interesting to observe the dependence of the scattering amplitude with the wavelength (it explains the red sunset and the blue of the sky) and the volume of the particle.

3.2.2 Rayleigh-Debye scattering (Born approximation)

For a scatterer whose relative dielectric constant is near to unity, the electric field is approximately equal to the incident field.

$$\mathbf{E}(\mathbf{r}) \approx \mathbf{E_i}(\mathbf{r}) \tag{3.11}$$

The following condition is required for this approximation:

$$(\varepsilon_r - 1) k_0 2a \ll 1 \tag{3.12}$$

meaning that the added phase shift of the wave, after travelling all the particle, with respect to the travelling in the absence of the particle, is relatively small.

For an homogeneous sphere with radius a the scattering amplitude is [25]:

$$\mathbf{f}(\mathbf{u_s}, \mathbf{u_i}) = \frac{k_0^2}{4\pi} [-\mathbf{u_s} \times (\mathbf{u_s} \times \mathbf{u_e})] (\varepsilon_r - 1) V F(k_s) \tag{3.13}$$

where $F(k_s)$ is a function that depends on the shape of the scatterer. The function has been computed for disks and spheres and the solutions can be found in [25]. For a sphere the solution gives:

$$F(k_s) = \frac{3}{k_s^3 a^3} [\sin(k_s a) - k_s \cos(k_s a)] \tag{3.14}$$

where $k_s = 2ksin(\theta/2)$ and θ is the angle between the incident and scattered waves: see Figure 3.5. If $\theta = 0$ we are observing the forward direction and for $\theta = \pi$ we have the backward direction (backward scattering that is useful for mono-static radar equations).

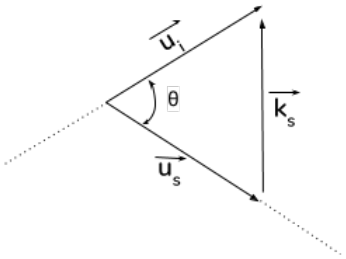

Figure 3.5: Relation between $\mathbf{u_i}$ and $\mathbf{u_s}$.

We can compute now the scattering amplitude of small bubbles, in the vacuum, with relative dielectric constant of $\epsilon_r = 1.00004$, radius $a = 1$, $a = 5$ and $a = 25$ mm and at a frequency of $f = 39.4$ GHz. Figure 3.6 shows the normalized radiation diagram for these three bubbles. As we can observe, the scattering is most predominantly in the forward direction like an endfire array of antennas.

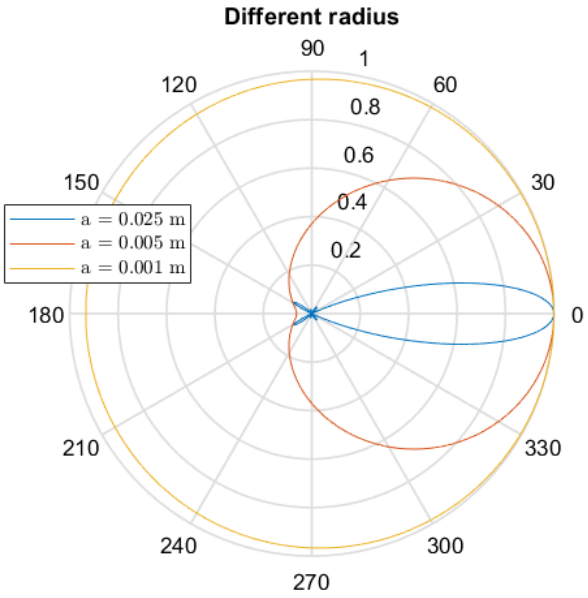

Figure 3.6: Radiation diagram for three bubbles with different radius.

As can be seen, with the size increase the scattering pattern becomes more directive and for larger sizes it develops side lobes. It must be noted that the scattering amplitudes increase 125 times each time the radius increases 5 times.

The starting point for the scattering amplitude calculation is the choice of the model that best describes the particular case: the decision is made based on the size, frequency and refraction index. Knowing the wave propagation frequency and the particle size, it is clear,

from Figure 3.7, which model to use. It is also clear that with the increase of the particle size, the scattering pattern becomes more directional, exhibiting a maximum scattering amplitude in the forward direction, and with side lobes appearing.

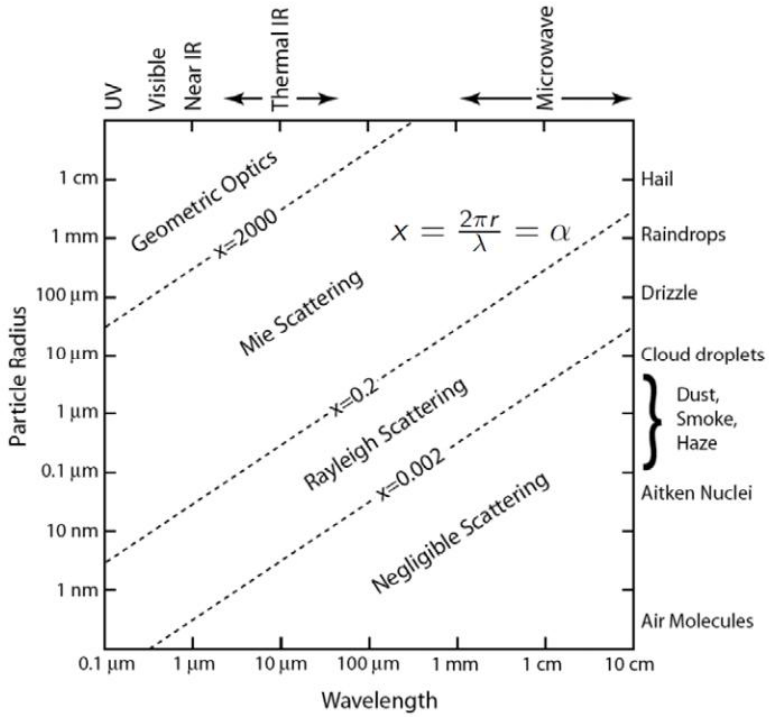

Figure 3.7: Scattering theories. [1]

These approximations take into account the scattering caused by hydrometeors that exist in the atmosphere. In fact, for scintillation applications we will have a far much more complex propagation medium than a set of regular single spherical bubbles with a specific index of refraction. The irregularities are spread along the path: we have bubbles of several sizes, bubbles embedded in larger size bubbles, different refractive indexes, fields that have already been scattered, impinging the bubbles and so on. We have in fact a random continuum and some kind of statistical description of the refractive index structure of the atmosphere is needed.

A simpler way to understand the turbulence development and spectrum is to imagine a bridge and its pillars seating in a river. The river's current goes against the pillars full of energy, however this causes at the other side of the pillars turbulence next to them. In fact, this creates swirls and inside this swirls smaller ones, which go with the flow and against each other, dissipating energy. Far ahead the water flow ceases to have irregularities. For the atmosphere we can think of layers with distinct wind velocities or instabilities of rising volumes of air (buoyancy) introducing energy at large dimensions (the input range), L_0, typically from 100 to 300 m and, then, this energy is converted to eddies, whose dimensions are successively smaller down to l_0 (a few mm or cm) where the energy is dissipated (the dissipation range).

3.3 Waves through turbulence

However, an analytic solution of the turbulence characteristics cannot be achieved, being the statistical approach the only possible. The atmosphere is known to be an inhomogeneous random medium characterized by a refractive index $n(r,t)$ which is a stochastic function of space and time. On the other hand, taking into account its sub-regions, it can be considered locally homogeneous and isotropic. The problem within this matter relies on a resolution based on approximations. The effects of this time varying turbulent medium on the propagated wave requires the resolution of the Maxwell wave equation that, by is turn, must need in some way the statistical characterization of the time and spatial index of refraction along the propagation path.

An electromagnetic wave crossing a turbulent layer, where the (small) refractive index changes with time and space, must be described by the well know Maxwell equation:

$$\nabla^2 E + k^2[1 + \delta\varepsilon(r,t)]E = 0 \tag{3.15}$$

where $\delta\varepsilon$ represents a perturbation in the dielectric constant. The solution of this equation follows a method developed by Rytov's that has been widely described and experimentally validated [26].

3.4 Kolmogorov spectrum

In figure 3.8, L_0 represents the external turbulence ranging from a few meters to about one km, l_0 represents the inner turbulence (in the order of millimetres) and h the height at which the turbulence takes place.

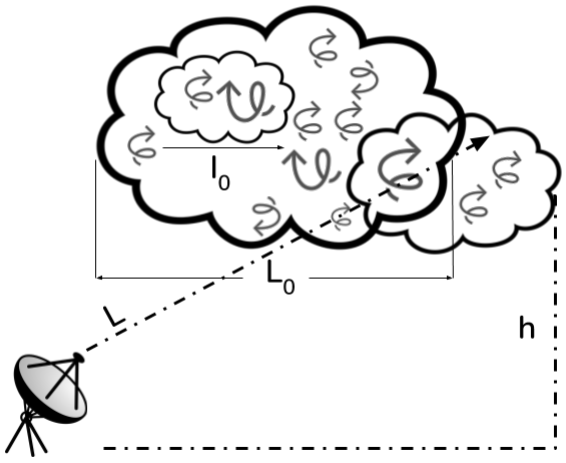

Figure 3.8: Link through a turbulent path.

A typical method to measure the turbulence intensity is given by a structure parameter: C_{n}^2 [27].

Freezing the atmosphere in time, and letting it be dragged by the wind, is usually a scenario used in scintillation theory. A relationship between the refractive index at one point

and the refractive index in a neighbour point at a distance r is required and, then, the frozen hypotheses is used to derive the spectral characteristics of the scintillation. The, so-called refractive-index structure function, is usually defined:

$$D_n(\rho) = \left\langle \left[\delta n(r,t) - \delta n(r+\rho,t)\right]^2 \right\rangle \tag{3.16}$$

Assuming t = 0, static turbulence, the above expression can be written as:

$$D_n(\rho) = \left\langle \left|\delta n(r) - \delta n(r+\rho)\right|^2 \right\rangle \tag{3.17}$$

where <> denotes an ensemble average, $n(r)$ is the refractive index at position r and $n(r+\rho)$ the refractive index at distance ρ from r.

If the spatial difference ρ, in between the two points is larger than the inner scale of turbulence, given by l_0 but smaller compared to the outer scale, L_0, Kolmogorov showed that the structure function of the velocity field in the inertial subrange satisfies a universal 2/3 power law.

$$D_n(\rho) = C_n^2 |\rho|^{\frac{2}{3}} \tag{3.18}$$

Naturally, if ρ is equal to zero, therefore $D_n(\rho) = 0$. Increasing ρ, the value of the structure $D_n(\rho)$ increases too. C_n^2 represents the refractive-index structure constant, which is a measure of inhomogeneity of refractive index.

For a homogeneous and isotropic medium, the spectrum of irregularities of the refraction index is given by:

$$\Phi_n(\kappa) = \frac{1}{2\pi^2 k} \int_0^\infty B_n(r) sin(\kappa r) dr \tag{3.19}$$

being the ensemble average $B_n(r,r') =< \delta n(r,t)\delta n(r',t) >$ the spatial covariance of refractive index fluctuations. As a three dimensional Fourier transform relates the covariance of the refractive index of fluctuations with the spectrum of fluctuations, the following relationship holds [28]:

$$B_n(r) = \frac{4\pi}{r} \int_0^\infty \kappa \Phi_n(\kappa) \sin(\kappa r) d\kappa \tag{3.20}$$

where r represents the position of the turbulence eddy, and κ is the physical quantity corresponding to the angular/spatial wave number, defined by $\frac{2\pi}{l}$. In the presence of a homogeneous medium the form of the $\Phi_n(\kappa)$ spectrum, is equivalent to $\Phi_v(\kappa)$ spectrum, which represents the speed of all atmospheric fluctuations.

To summarize $\Phi_v(\kappa)$ represents the amount of energy released by the turbulence bubbles/eddies of dimension l. This energy comes from the circulation of the air masses and it is directly related to the region of origin. For small values of κ, corresponding to the outer scale, the introduction of kinetic energy results in the development of the turbulence. However, the mathematical description of the spectrum is not defined. This zone is referred to as Input Range.

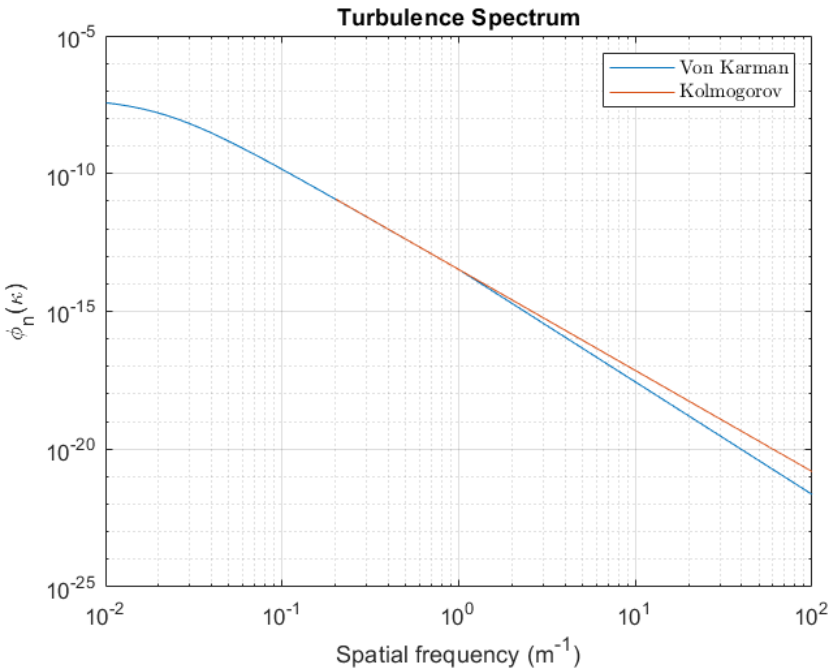

Figure 3.9: Kolmogorov and von Karman spectrum's.

Increasing the value of κ, means to consider irregularities from L_0 to l_0, whose turbulence behaviour is known. The spectrum of this sub-region, that is known by Inertial Subrange, is proportional to $\kappa^{-\frac{11}{3}}$.

Large swirls are considered unstable, leading to their splitting and transferring energy to eddies of lower dimensions until they become so small that the viscosity becomes relevant and the energy is dissipated. The dissipation region begins at the wave number corresponding to $\kappa_0 = \frac{2\pi}{l_0}$. Again, the spectrum shape is fully known, but decays faster than in the Inertial Subrange. By putting together, all sub regions in an equation, the spectrum global equation is:

$$\Phi_n(\kappa) = \begin{cases} \text{unknown}, & \kappa < \frac{2\pi}{L_0} \\ 0, & \kappa > \frac{2\pi}{l_0} \\ 0.033 C_n^2 \kappa^{\frac{-11}{3}}, & \frac{2\pi}{L_0} < \kappa < \frac{2\pi}{l_0} \end{cases} \tag{3.21}$$

Alternatively, another expression, that can be used is the von Karman approach [21], [29]:

$$S(\kappa) = \frac{\alpha(\mathrm{n}) e^{-(2\kappa/\kappa_m)}}{(1/L_0^2 + \kappa^2)^{\mathrm{n}/2}} \tag{3.22}$$

with the factor $\alpha(\mathrm{n})$ begin function of the exponent n:

$$\alpha(\mathrm{n}) = \frac{\Gamma(\mathrm{n}-1)}{4\pi^2} \sin\frac{\pi(\mathrm{n}-3)}{2} C_n^2 \quad 3 \leq \mathrm{n} \leq 5 \tag{3.23}$$

where $\Gamma(.)$ is a gamma function, $\kappa_m = \frac{5.91}{l_0}$ and the values l_0 and L_0 are the limit values of possible eddy sizes. The value n corresponds to the slope of the spectrum and will be further mentioned in other situations.

In Figure 3.9 are displayed the two approaches to the turbulence spectrum, based on equations (3.21), (3.22): Kolmogorov and von Karman. The similarity between the two approaches is evident.

Until this point, C_n^2 was considered to be constant throughout all turbulent path. Obviously it is a very blunt approximation of the refractive index in-homogeneity. Considering more realist assumptions for the C_n^2 distribution, three different models, illustrated in figure 3.10, are presented next [26].

C_n^2 characterization

- Slab model

The turbulence is homogeneous along all the propagation path L.

$$C_n^2(z) = C_n^2 \begin{cases} 1, & 0 < z \leqslant L \\ 0, & L > z \end{cases} \tag{3.24}$$

- Thin layer model

In this case, eddies are only located at a layer with thickness of ΔL at an altitude L.

$$C_n^2(z) = C_n^2 \begin{cases} 1, & L < z < L + \Delta L \\ 0, & others \end{cases} \tag{3.25}$$

- Exponential layer model

Finally, this model follows an exponential evolution. The layers close to the Earth's surface are the most turbulent decreasing exponentially along the path.

$$C_n^2(z) = C_n^2(0) \exp\left(- \frac{z}{L} \right) \tag{3.26}$$

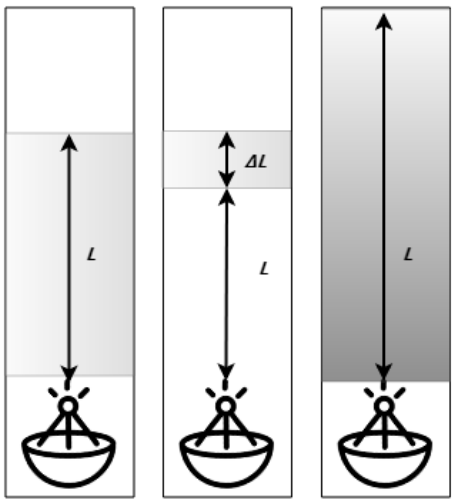

Figure 3.10: Slab model - Thin layer model - Exponential layer model.

The refractive index structure constant value ranges from $10^{-15}m^{-2/3}$ to $10^{-12}m^{-2/3}$. On turbulent layers, the value is estimated to be about $10^{-12}m^{-2/3}$ [21].

Under a long period, turbulence is a non-stationary process. However, if it is measured in smaller periods (between 10 a 15 minutes) it can be considered stationary.

3.5 Scintillation variance

As a result of the three described approaches to the refractive index structure C_n^2 along the path, the variance of the scintillation amplitude has three different equations [26].

A widely known expression to calculate the scintillation variance for a homogeneous path of length L, assuming a point receiver, is given by [25]:

$$\sigma^2(\chi) = 2\pi k^2 L \int_0^\infty \kappa S(\kappa) f(\kappa) d\kappa \quad (dB^2) \tag{3.27}$$

where $S(\kappa)$ is given by (3.22). To understand the above equation, it is interesting to note that the radius of the first Fresnel zone is given by $\sqrt{\lambda L}$ which is equivalent to have $\sqrt{(2\pi L/k)}$. If the size of the eddies outgrows the size of the first Fresnel zone, their contribution to the signal fluctuations decrease due to the high-pass filter function [23]:

$$f(\kappa) = 1 - \frac{[\sin{(\kappa(L/k)^{1/2})}]^2}{[\kappa(L/k)^{1/2}]^2} \tag{3.28}$$

Regarding the slab model, the scintillation variance is given by [26]:

$$\begin{aligned} \sigma^2(\chi) &= 0.307 C_n^2 k^{\frac{7}{6}} L^{\frac{11}{6}} \quad (Np)^2 \\ &= 0.307 (20 log_{10} e)^2 C_n^2 k^{7/6} L^{11/6} \quad (dB)^2 \\ &= 23.387 C_n^2 k^{7/6} L^{11/6} \quad (dB)^2 \end{aligned} \tag{3.29}$$

For the thin model:

$$\begin{aligned} \sigma^2(\chi) &= 0.563 C_n^2 k^{\frac{7}{6}} L^{\frac{5}{6}} \Delta L \quad (Np)^2 \\ &= 42.475 C_n^2 k^{\frac{7}{6}} L^{\frac{5}{6}} \Delta L \quad (dB)^2 \end{aligned} \tag{3.30}$$

Finally, for the exponential model:

$$\begin{aligned} \sigma^2(\chi) &= 0.530 C_n^2(0) k^{\frac{7}{6}} L \quad (Np)^2 \\ &= 39.986 C_n^2(0) k^{\frac{7}{6}} L \quad (dB)^2 \end{aligned} \tag{3.31}$$

All situations above assume $l_0 << \sqrt{\lambda L} << L_0$: basically it means that the first Fresnel zone diameter is smaller than the outer scale but larger than the inner scale.

However in the range of scales larger than L_0, ($\sqrt{\lambda L} >> L_0$), an assumption is made considering the random refractive index field statistically homogeneous and isotropic for all scales [30]. In this case, Tatarski showed a dependence between log-amplitude fluctuations of scintillation and the wavenumber k^2.

$$\chi^2 = \overline{(\Delta n)^2} k^2 L L_{\mathrm{n}} \quad (dB) \tag{3.32}$$

Provided that the variance is given by:

$$\sigma^2 = 75.45\overline{(\Delta n)^2}k^2 L L_{\mathrm{n}} \quad (dB^2) \tag{3.33}$$

with $\overline{(\Delta n)^2}$ being the mean square of the refractive index fluctuations and lastly, L_n is the integral scale of turbulence [30].

3.5.1 Analysis of Fresnel radius for the experimental scenario

An electromagnetic wave is made of the contribution of the wave fields in a previous area, usually, defined by circles with the following radius:

$$F_n = \sqrt{\frac{n\lambda d_1 d_2}{d_1 + d_2}} \tag{3.34}$$

being n an integer number and d_1 and d_2, respectively, the distance from the receiver to the contribution area and the distance from the contribution area to the source. If $d_2 \gg d_1$ the following simplification can be obtained:

$$F_n = \sqrt{n\lambda d_1} \tag{3.35}$$

The circle defined by $n = 1$ is the most contributing one. The first Fresnel zone is an ellipsoid whose cross section radius F_1 at a distance d of a point P, defines the area of the wavefront that most contributes to build the wavefront in P. The radius increases with the distance and decreases with the frequency increase.

In order to have a notion of the quantities involved, the ellipsoid radius is depicted as a function of the path distance to the turbulent layer, L, in Figure 3.11a, and also, as a function of the height of the turbulent layer, in Figure 3.11b.

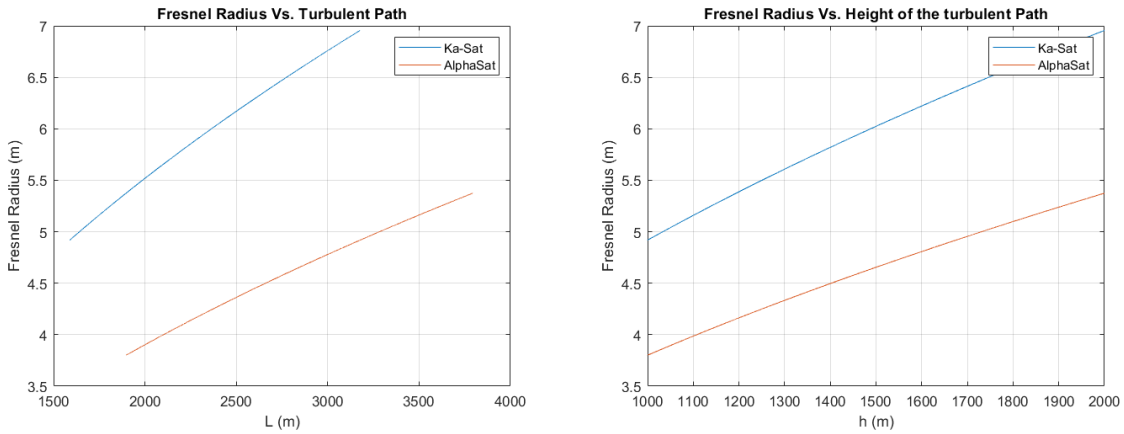

(a) First Fresnel radius as a function of the path length for the Ka-Sat and AlphaSat frequencies.

(b) First Fresnel radius as a function of the turbulent layer height for the Ka-Sat and AlphaSat.

Figure 3.11: Fresnel radius comparisons.

3.6 Scintillation spectrum

Similar to Guassian white noise, which is recognized as a sequence of serially uncorrelated random samples with zero mean and finite variance, the scintillation signal is based on the same characteristics however the spectrum is not flat [23].

The scintillation spectrum evaluates how fast the signal fluctuates around the mean value. It describes a relation between the fade-rate and the auto-correlation function $R(\tau)$ [21].

The power spectrum of the scintillation time series, $W_\chi(f)$, normally is represented by an asymptotic form, meaning that the first equation represents the spectrum when the frequency tends to zero and the second equation when the frequency tends to infinity [21].

$$W_\chi^0 = \frac{2.765}{\omega_0}\sigma^2(\chi) \quad (dB^2/Hz) \tag{3.36}$$

$$W_\chi^\infty = \frac{7.13}{\omega_0}\sigma^2(\chi)\left(\frac{\omega}{\omega_0}\right)^{-8/3} \quad (dB^2/Hz) \tag{3.37}$$

Notably, for the higher frequencies, the spectrum has a roll off factor with a frequency dependence, $f^{-\frac{8}{3}}$. This frequency is related to the wind velocity component that is perpendicular to the slant path, v_t. On the other hand, this frequency is called the Fresnel frequency and is given by:

$$w_0 = v_t\sqrt{\frac{2\pi}{\lambda L}} \quad (rad/s) \tag{3.38}$$

The frequency at which the two asymptotes intersect is called the corner frequency, f_c, [14] and establishes a relation with the Fresnel frequency: $w_c = 1.43w_0$ [21]. Given the equation above, the factor $\sqrt{\lambda L}$ stands out and gives the dominant eddy size. Figure 3.12 presents the theoretical spectrum of scintillation.

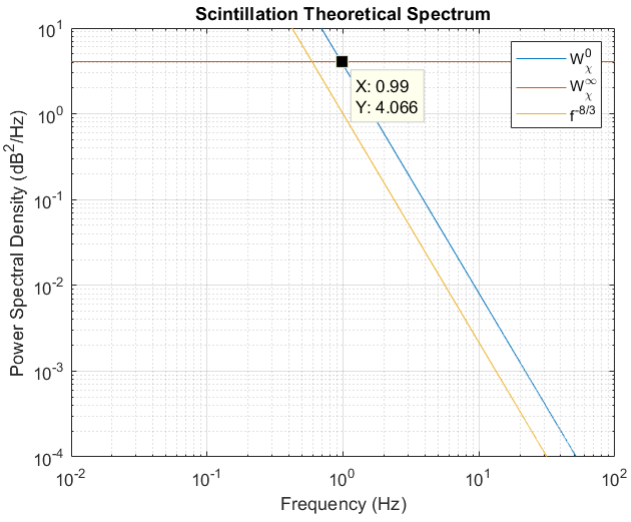

Figure 3.12: Scintillation Theoretical Spectrum.

Assessing Figure 3.12, based on the theory behind the scintillation spectral behaviour, mentioned in section 3.1, generally speaking, it corresponds to the expected: at the lower

frequencies the power spectrum density remains constant until it reaches the corner frequency f_c, where the spectrum falls with a slope about $f^{-8/3}$. The corner frequency can be useful to compute the wind velocity. It must be pointed out that the corner frequency increases with the beacon frequency.

3.7 Effects of the antenna aperture size

All equations mentioned above are based on a point receiver, which is an antenna with an infinitesimal diameter, D. However, it is necessary to take into account this parameter, both in the amplitude parameters as well as in the scintillation spectrum.

3.7.1 Effects on the scintillation amplitude

An aperture antenna delivers a signal that is the integration of the electric field over the reflector aperture. Haddon and Vilar showed that larger antennas have a smoothing gain, which is beneficial for scintillation amplitude (lower amplitudes) [21]. We can expect that spatial wavelengths shorter than the antenna diameter will be attenuated: the antenna acts as a low-pass spatial filter. The effects described above causes a reduction of the scintillation amplitude. The ratio between the variance and the measured variance by a point antenna, $G(x)$ (usually called smoothing gain or gain), is given by:

$$G(x) = 3.86(x^2+1)^{11/2} \sin\left[\frac{11}{6}\tan^{-1}\left(\frac{1}{x}\right)\right] - 7.08x^{5/6} \tag{3.39}$$

with x defined as:

$$x = 0.0584\frac{D^2\eta k}{L} \tag{3.40}$$

where η is the aperture efficiency, usually around 50 to 60%. It must be noted that the variable x is related to the square of the ratio of antenna diameter and the first Fresnel radius: the higher the D the larger is x, that is the antenna size is larger than the Fresnel radius. The turbulent layer distance, L, from the receiver is given by [31]:

$$L = \frac{2h}{\sqrt{sin\theta^2 + (2h/a_e)} + sin\theta} \quad (m) \tag{3.41}$$

where a_e is the effective earth's radius that equals 8.5M meters, h is the height of turbulence and θ is the elevation angle.

Another way to calculate the antenna averaging factor is to use the piecewise approach given by Karasawa [32]:

$$G(D_e) = \begin{cases} 1.0 - 0.7\left(\frac{D_e}{\sqrt{\lambda L}}\right) & for \quad 0 \leq \frac{D_e}{\sqrt{\lambda L}} \leq 1.0 \\ 0.5 - 0.2\left(\frac{D_e}{\sqrt{\lambda L}}\right) & for \quad 1.0 < \frac{D_e}{\sqrt{\lambda L}} \leq 2.0 \\ 0.1 \quad for \quad 2.0 < \frac{D_e}{\sqrt{\lambda L}} \end{cases} \tag{3.42}$$

where $D_e = \sqrt{\eta}D$ is the effective antenna diameter and D the physical diameter. The value of L is also given by equation (3.41), but, Karasawa suggested to use $h = 2000$ m for scintillation modelling [32].

To illustrate how the factor x affects the smoothing gain value, equation (3.39) was computed: results are displayed in Figure 3.13.

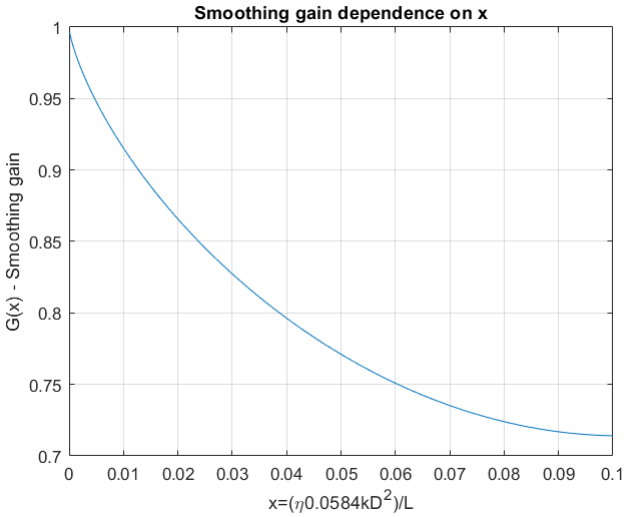

Figure 3.13: Smoothing gain dependence on x.

From figure 3.13 is concluded that the smaller the x the larger the smoothing gain. In our particle case, the beacon with the larger frequency has the smaller antenna diameter and vice-versa. Going back to equation 3.40, the diameter value has a greater weight in the equation. Inducing that the antenna with the larger diameter will have a higher x. This statement is proved using the values shown in the Tables (3.1, 3.2):The Ka-Sat receiver has a greater value of x.

Table 3.1: Beacon frequencies and receiver link parameters

	f (GHz)	θ (°)	D (m)	η(%)
Ka-Sat	19.7	39	1.5	0.6
AlphaSat	39.4	31.8	0.62	0.6

In order to compare the smoothing gains, equation (3.39) was plotted for the two frequencies. Considering the parameters given in table 3.1, the results of the smoothing gain are depicted in Figure 3.14a, as a function of h. The increase of h means that the turbulence is happening further away from the Earth station receiver. As previously shown, Figure 3.11b, for higher altitudes the Fresnel ellipsoids are bigger and the reflector integrates contributions from a larger area of turbulent eddies, therefore, the fields over all the antenna area are more correlated.

Table 3.2 summarizes the input data and the output parameter, x, from equation 3.39, using a turbulence height $h = 1000$ m.

Table 3.2: Calculation of the parameter x of equation (3.39).

Frequency (GHz)	h (m)	L (m)	k (rad/m)	x
19.7	1000	1588.8	412.59	0.0205
39.4	1000	1897.3	825.19	0.0059

The highest frequency link has a smaller x, and returning to Figure 3.13, it is straightforward that a smaller x corresponds to a higher $G(x)$. The smoothing gain value is a little bit higher for the Q-band.

As the turbulence height increases, the smoothing gain ratio between the two beacons approaches the value of 1, as can be seen in Figure 3.14b. So the scaling of the scintillation intensity is not strongly related to a possible physical variability of $G(x)$.

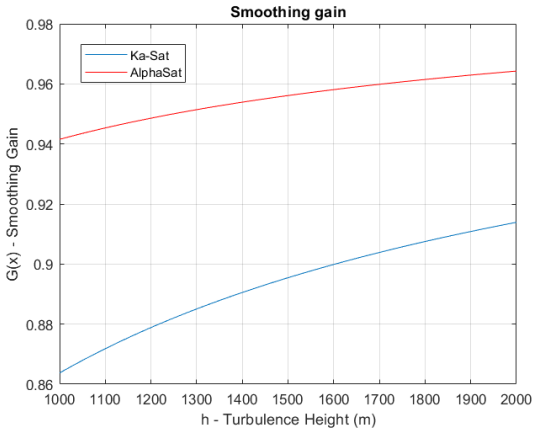

(a) Smoothing gain for the two frequency bands.

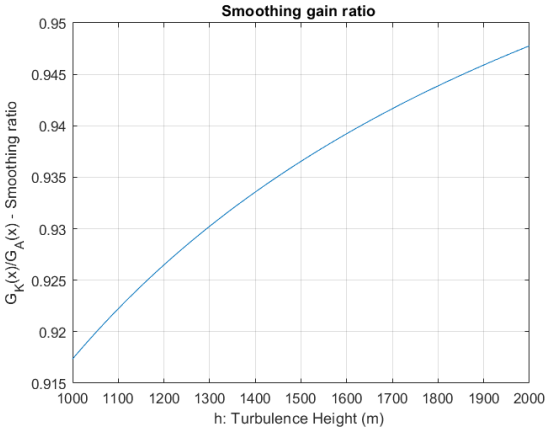

(b) Smoothing gain ratio between the two frequency bands.

Figure 3.14: Smoothing gain relations.

Other relation that is important is the impact of the elevation angle on the smoothing gain. For this purpose, the expression (3.39) was computed and the results are displayed in Figure 3.15.

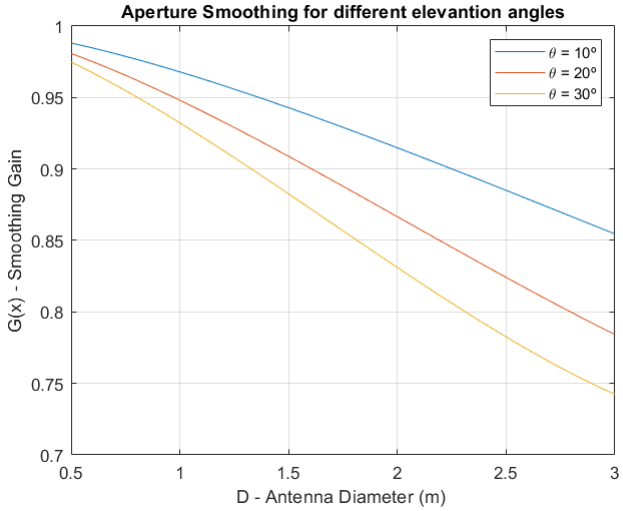

Figure 3.15: Smoothing gain as a function of the antenna diameter.

First, the most visible conclusion is, as seen before, that the larger the antenna diameter the smaller the smoothing gain is. Second: lower elevation angles means larger Fresnel radius

at the turbulence layer which leads to the influence of more uncorrelated eddies increasing the smoothing gain (closer to unity). The scintillation amplitude itself depends not only, as it is obvious now, from the aforementioned smoothing gain.

3.7.2 Effects on the scintillation spectrum

The size of the antenna not only impacts the scintillation amplitude but also impacts the power spectrum of the scintillation amplitude. The expression that relates the scintillation spectrum for an antenna with diameter D with the spectrum observed for a point receiver is [21]:

$$\frac{W_\chi^0(D)}{W_\chi^0(0)} = 4.66x^{4/3} - 2(x^2+1)^{7/6}\sin\left[\frac{7}{3}\tan^{-1}\left(\frac{1}{x}\right)\right] \tag{3.43}$$

$$\frac{W_\chi^\infty(D)}{W_\chi^\infty(0)} = 1.053\left(\frac{\omega_s}{\omega}\right)e^{-(\omega/\omega_s)^2} \tag{3.44}$$

where x is given in equation (3.40) and $\omega_s = 4.1391 v_t/D$ is the scintillation frequency from which a larger decay is observed [23]. The antenna also performs a time filtering on the scintillation amplitude. It is important to notice that ω_s is larger than ω_c, so in our case, the filtering effect cannot be observed because the power of the signal at this frequency is well below the noise floor of the beacon measurements. This fact is summarized in Table 5.5. The following Table 3.3, resulted from the computation of expression (3.43) for the two beacons and their parameters are detailed on Table 3.1.

Table 3.3: Critical frequencies of the scintillation spectrum for the two beacons: calculated for the described parameters

	f_s (Hz)	f_c (Hz)	f_0 (Hz)	v_t (m/s)	L (m)
AlphaSat	5.313	0.751	0.525	5	1897.7
Ka-Sat	2.196	0.579	0.405	5	1589.0

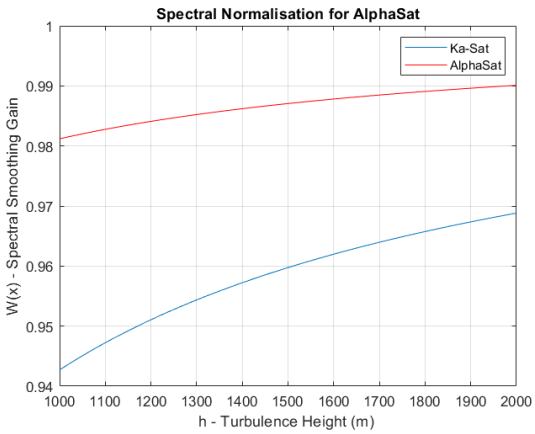

Figure 3.16: Low frequency spectrum normalization factor for the two beacons.

The impact of increasing the antenna diameter, for the lower scintillation spectrum fre-

quencies is not significant (Figure 3.16 proves this statement). It can be concluded that it is possible to compare the the scintillation spectrum's at the two frequencies without being concerned about this normalization factor.

3.8 Scintillation frequency scaling

A substantial part of this work is related to the scintillation phenomenon at two different frequencies. An investigation point is the relationship of the scintillation parameters - mainly scintillation amplitudes and scintillation intensity - between the two experiment frequencies: 19.68 and 39.4 GHz. It is desirable to perform a comparison between the two, and the preferable way is to compare the scintillation intensity [21]. The frequency scaling ratio is the ratio of the variance of the scintillation amplitude experienced at the two frequencies, due to a wave propagation along the same path simultaneously and measured during a time interval within which the turbulence can be modelled as a stationary random process [33].

So, let us assume two oblique links: one at frequency f_1, path length L_1 and elevation θ_1 and, eventually, a thin turbulent layer ΔL_1 and another link at frequency f_2, path length L_2 and elevation θ_2 and, eventually, a thin turbulent layer ΔL_2. For a turbulence pattern, described with a slab model or an exponential model, the frequency scaling, taking into account the equations, is given by [21]:

$$\frac{\sigma_1^2(\chi)}{\sigma_2^2(\chi)} \approx \left(\frac{f_1}{f_2}\right)^{7/6} \left(\frac{\sin\theta_2}{\sin\theta_1}\right)^{11/6} \frac{G(x_1)}{G(x_2)} \tag{3.45}$$

$$L \approx \frac{h}{\sin\theta} \quad (m) \tag{3.46}$$

with h being the turbulence height.

If the turbulence layer follows a thin layer model, frequency scaling is done with:

$$\frac{\sigma_1^2(\chi)}{\sigma_2^2(\chi)} \approx \left(\frac{f_1}{f_2}\right)^{7/6} \left(\frac{L_2\Delta L_2}{L_1\Delta L_1}\right)^{11/6} \frac{G(x_1)}{G(x_2)} \tag{3.47}$$

These equations are valid for a well-developed turbulence. As it can be observed, there is a frequency dependence similar for both cases, however, this is not the case with the path length. Assuming a fixed variance gain when plotting the variances in a log-log plot (scatter plot) we should get a straight line. In our experimental scenario, the path is not the same for both frequencies (at a height of 1 km the separation of the beams axis is of the order of a few hundred meters) so we expect that the variances have always a correlation but probably not so high as they should have for a propagation along the same path.

3.9 Data from literature

There is an extended database in Central Europe and some places in the USA, however, no data have been published at the Q-band at Portugal in spite of some results being already available at Ka-band. These data have been only partially analyzed to produce not much more than the ITU standard statistical Tables II-6 and II-7 for Earth-Space data (https://www.itu.int/en/ITU-R/study-groups/rsg3/Pages/dtbank-form-tables.aspx) [34].

The models describing the scintillation parameters have been developed using mostly data collected at frequencies lower than the Q-band. Some of these models are empirical (often curve fitting approaches) or semi-empirical by using meteorological parameters, namely N_{wet} or the temperature.

The following Table 3.4 shows different locations throughout the globe where scintillation measurements took place. It contains the satellite identification, the place, the available frequencies, plus the characteristics of the receiver and link parameters: the elevation angle, the antenna diameter and its aperture efficiency.

The results provided by these measurements helped to test and validate the different models available to predicted the scintillation parameters. No other big inputs were added to change/update the ITU models. It is important to state that to compare the standard deviation coming from different places a normalization, such as explained at section (3.8), is required.

Van de Kamp, [35], showed that global databases are essential for the development of semi empirical models for the long-term scintillation intensity from different sites, whose climates and operating frequencies are way apart.

Aveiro is a very privileged site to collect new data, because its climate characteristics are substantially different from the places with other data sets. The city is close to the sea, very humid and the seasons are well defined. Data at the frequencies of this project were little explored so this will be a significant contribution for the ITU global scintillation database.

This site has already been a part of a relevant project where scintillation was analyzed for different locations around Europe, such as: Spain (Madrid), Austria (Graz), Italy (Spino d'Adda and Tito Scalo) and France (Toulouse and some other sites).

In the southern area of France, two different experiments took place. The first one started in 2009 until 2011, in Toulouse where the signal from the satellite HotBird6 at 19.7 GHz was received. The other experiment was based on the analysis of the ASTRA-3B satellite data, not only in Toulouse, but throughout several places in the southern France. Some of this places were: Aussaguel, Le Fauga, Salon de Provence, Aire sur l'Adour (all these sites used 20.2 GHz).

In Austria, more precisely in Graz, some scintillation analysis was done at the Alphasat beacon frequencies. The statistical analysis in Madrid included data from an experiment with Eutelsat HB6 satellite and one year of data from the Ka-Sat: both experiments at ka-band. At Spino d'Adda, in Italy, during the ITALSAT experiment, scintillation was measured at the frequencies of 18.7 GHz, 39.6 GHz and 49.5 GHz. The AlphaSat campaign was made in Spino d'Adda and Tito Scalo at both beacon frequencies.

From the observation of the report for the scintillation statistical analysis, it is clear a high variability between the results of the different sites [36]. Anyway, the analysis in almost all the cases was very limited: often oriented to deliver the ITU tables.

Table 3.4: Sites where scintillation was analysed.

	Coordinates (N - E)	**f (GHz)**	θ (°)	**D (m)**	η (%)	**Satellite**
Austin	30.39 – 262.27	11.20	5.8	2.4		Intelsat - 510/602
Blacksburg	37.23 – 279.60	12.5 19.77 29.66	14	4 1.5 1.2		Olympus
Chibolton	51.45 – 5.49	11.20	7.1	3		Intelsat-V
Crawford Hill	40.39 – 285.81	19.04 28.56	38.6	7	0.73	Comstar
Darmstadt	49.87 – 8.63	12.5 19.77 29.66	27	1.8 3.7 3.7	0.5 0.5 0.5	Olympus
Eindhoven	51.45 – 5.49	12.5 19.77 29.66	26.8	5.5	0.92 0.78 0.44	Olympus
Kirkkonummi	60.22 – 24.40	19.77 29.66	12.7	1.8	0.63 0.38	Olympus
Lesive	50.22 – 5.25	12.5 19.77	27.8	1.8	0.6	Olympus
Louvain	50.76 – 4.62	12.5 29.66	27.6	1.8	0.6	Olympus
Martlesham	52.06 – 1.29	11 14.27	≈ 10	6.1		Intelsat-V ($\approx 60°$)
Martlesham	52.06 – 1.29	19.77 29.66	27.5	1.8 6.1		Olympus
Spino d'Adda	45.40 – 9.49	12.5 19.77	30.6	3.5		Olympus
Spino d'Adda	45.40 – 9.49	18.7 39.6 49.5	37.8	3.5		Italsat
Tokyo	35.6 – 139.7	4.17 6.39	5.5	22		Cas A
Upola	20.27 – 204.13	9.55 19.1 22.2 25.4 33.3	2.5	2.7 2.7 2.7 2.7 2.0		Mt. HaleaKala
Yamaguchi	34.18 – 131.55	11.45 14.27	6.5	7.6		Intelsat-V (60^{o})

3.10 Scintillation correlation

An important part of this work lays around the cross-correlation of the scintillation intensity or the standard deviation. Of course we are discussing not the amplitude correlation – even the amplitude auto-correlation becomes very small after a few seconds - but the standard deviation correlation. Having two antennas with different characteristics located in the same region but separated by a few meters it is expected that some correlation can be observed. According to the theory, the correlation should decrease if the antennas are separated by more than the Fresnel radius. Such issue has been discussed in [20]. In our case we have two converging beams that cross generously separated volumes at a large distance from the antennas. A plot of the separation of the beams as a function of the altitude is depicted in the following figure.

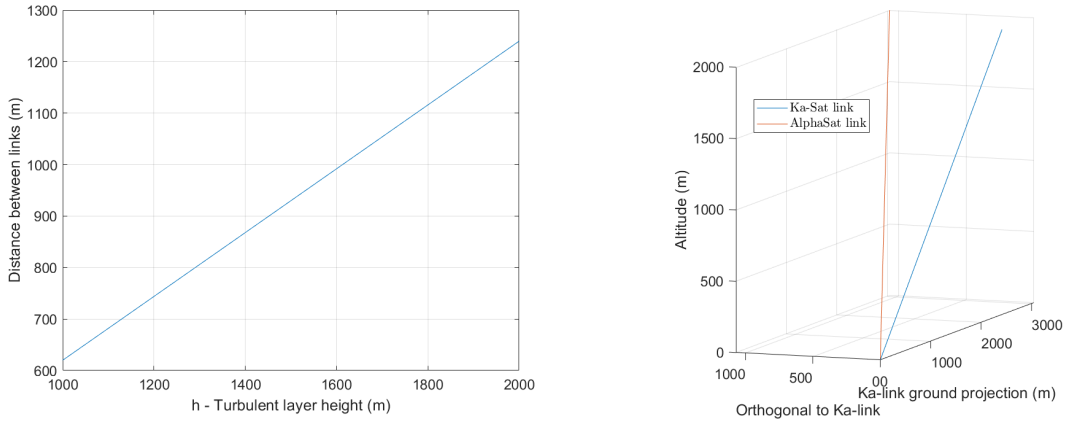

(a) Horizontal distance between the two links.

(b) 3D view of the two links.

Figure 3.17: Beam separation as a function of altitude.

The correlation of the scintillation standard deviation in this conditions has never been studied as far as the author knows. At a first sight, in Figure 3.17, we could observe the distance between the beams at typical layer altitude of 1000 to 2000 m is much larger than the input range L_0 so the antennas can observe eventually distinct eddies, unless the eddies travel quite fast or the turbulent areas have unusually large sizes.

Taking as reference a single turbulent eddy, as it passes through the Q-band antenna, only a few seconds later its influence on the signal will be observed in the Ka-band antenna. In order to verify this statement, was carefully selected a small period of time to observe the scintillation variance relation between the two beacons. Figure 3.18 proves visually that when the variance in one beacon increases after a few moments the same increment can be observe in the other.

In order to calculate how much time takes for the same turbulent eddy to get from one beacon to the other the cross-covariance was used. Cross-covariance measures the similarity of two time series as a function of the time offset between the two series. In this case, the offset is considered in time-lags. For the day in question, Figure 3.19 shows the correlation between the two standard deviations for a period of 5 minutes. The maximum value for the correlation, represented by the peak at the figure, evaluates the best resemblance of the two separate signals.

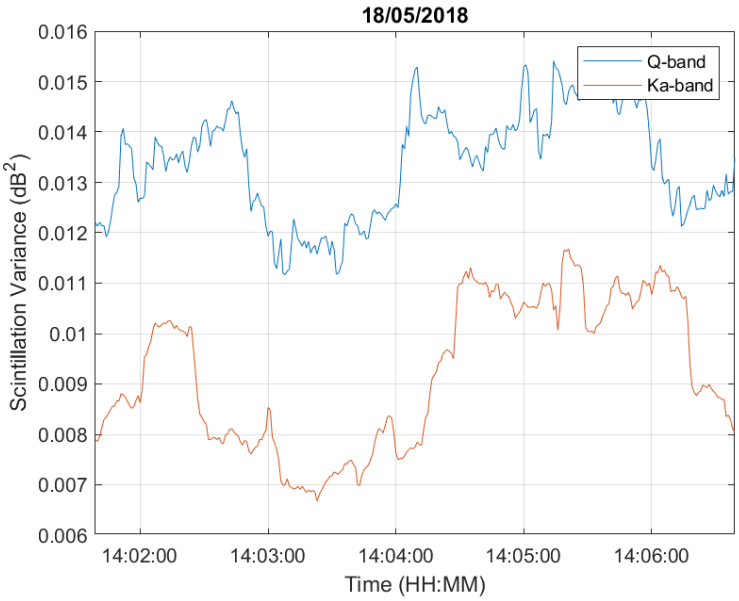

Figure 3.18: Variance for two different frequencies.

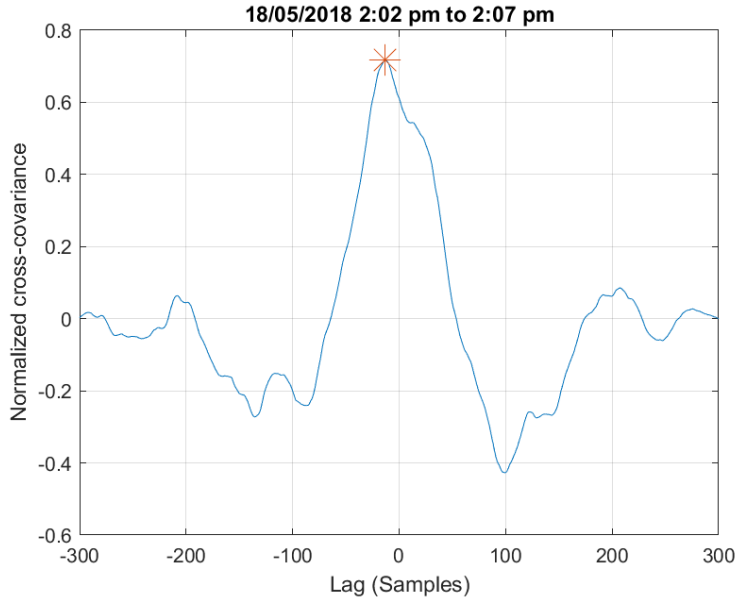

Figure 3.19: Cross - covariance.

In Figure 3.19 the maximum value is marked as 0.8 in a normalized scale. If the point were in the abscissa 0 the two signals would have no relative delay. In this case, the offset is -13 samples, meaning that one of the signals is 13 samples duration late in relation to the other. This subject will be further analyzed in a following chapter.

Chapter 4

Scintillation modelling

Section 4.1 introduces the general qualitative behaviour of the scintillation phenomenon, section 4.2 describes the amplitude and standard deviation distributions. A section 4.3 presents the following scintillation prediction models:

- ITU-R;
- Karasawa;
- Otung;
- Ortgies-T and Ortgies-N;
- van de Kamp.

4.1 Introduction

As discussed, the scintillation is due to the turbulence caused by the mixing of air masses with different humidity and temperature. The process develops in time and is carried by the wind. Often a frozen in assumption – that is, a special profile is assumed time invariant and moving across the link - is assumed for theoretical studies. The first models developed were purely empirical. The observation of the phenomenon has shown that it is, on average, more intense during the months with higher temperature and humidity, what makes sense: a warmer atmosphere is capable of retaining more water in the form of water vapour due to the higher water vapour saturation pressure. Also it has been observed that usually the early afternoon are periods with more intense scintillation often attributed to the sun heating causing more instabilities, such as the rising of hot air masses by a phenomenon called buoyancy. Also, more intense scintillation has been observed in the presence of clouds, [37] and [38], therefore, a model was introduced that takes into account the cloud liquid water content. The development of physical models naturally relies on the wet refractive index and a correlation between scintillation and the wet refractivity, has been observed but only for very long integration times (a few weeks).

The amplitude and the standard deviation statistical distributions have been, as well, studied in several locations in spite of the data being still scarce at Q-band. The amplitude distribution was initially assumed as Gaussian with a null mean value and the standard deviation has been assumed as log-normally distributed or gamma distributed in short periods

of stationarity. Later on, van de Kamp, [39] recognized that the fades are deeper (the distribution is asymmetric) if the scintillation amplitude becomes higher, so other distributions have been considered for the amplitude. There is also some evidence that the intensity of the scintillation increases with the rain attenuation [40] but the topic will not be explored: the experimental data will exclude periods with attenuation larger than 0.5 dB for the Ka-band and 1 dB for the Q-band (that is, only the dry scintillation will be analyzed).

4.2 Statistical analysis - theory

It is important to understand the genesis of the commonly-used prediction models. The most known ones are described in section 4.3. The focus of the models is to describe scintillation by the variance of the log-amplitude, σ_χ^2. This variable was shown to be correlated with meteorological parameters and to be impacted by their variability. This section is devoted to the basic principles behind the first comprehensive scintillation modelling.

In section 3.5 several equations allowed to consider multiple practical situations for the refractive structure of the link path giving a value for σ_χ^2. With this value, it is possible to calculate the probability distribution of the amplitude χ. This probability distribution is useful to analyze link budgets or to use in time series simulators.

For long durations the scintillation intensity of χ follows a probability distribution, that can be transformed into a cumulative distribution $P(\chi > \chi_0)$, such as:

$$P(\chi > \chi_0) = \int_{\chi_0}^{\infty} \int_0^{\infty} p(\chi|\sigma_\chi) p(\sigma_\chi) d\sigma_\chi d\chi \tag{4.1}$$

In order to compute this cumulative distribution it is necessary to know the conditioned probability distribution, $p(\chi|\sigma_\chi)$, of the amplitude χ and the probability distribution of the standard deviation.

4.2.1 Distribution of the amplitude (χ)

Literature shows that a more accurate estimation of σ_χ^2 is only possible for periods greater than 10 minutes, because shorter periods give doubtful results [41]. In addiction, Vilar and Banjo [42] verified that for a short period of scintillation, its distribution depends on the intensity, σ_χ. More intense scintillation periods have distributions that move way from the typical Gaussian distribution. In fact, it happens because larger periods of intense scintillation have fades with deeper amplitudes than the enhancements. This causes the distribution to have a negative skewness.

Models presented in this dissertation assume different types of distributions. Both Karasawa and ITU-R methods agree on a Gaussian distribution for χ in the short-term basis.

The Gaussian distribution is given by:

$$P(\chi|\sigma_\chi) = \frac{1}{\sqrt{2\pi}\sigma_\chi} e^{-(\chi^2/2\sigma_\chi^2)} \tag{4.2}$$

The reason why scintillation falls into a Gaussian probability density is explained by Strobehn [43]. Briefly, the amount of scattering that happens in turbulent medium and the distance between it and the receiver, are the responsible for the different distributions.

Other model, presented in section 4.1 is the Van de Kamp [38]. It describes the turbulent medium as the thin layer model and far from the receiver, resulting in a Rice-Nakagami distribution:

$$p(\chi) = \frac{\chi}{\sigma_\chi^2} e^{-(\chi^2+\chi_0^2)/2\sigma_\chi^2} I_0\left(\frac{\chi\chi_0}{\sigma_\chi^2}\right) \tag{4.3}$$

where $I_0(.)$ is the modified Bessel function.

4.2.2 Distribution of the standard deviation (σ_χ)

Once again, Karasawa and ITU-R [32] are in agreement and both present a Gamma distribution for the standard deviation, presented below:

$$p(\sigma_\chi) = \frac{(a/m_{\sigma_\chi})^a}{\Gamma(a)} \sigma_\chi^{a-1} e^{-a\sigma_\chi/m_{\sigma_\chi}} \tag{4.4}$$

where $a = m_{\sigma_\chi}^2/\sigma_{\sigma_\chi}^2$ and m_{σ_χ} is the mean value of σ_χ and $\Gamma(.)$ is a gamma function:

$$\Gamma(a) = \int_0^\infty x^{a-1} e^{-x} dx \tag{4.5}$$

Others, such as Vilar and Haddon, show that the standard deviation follows a log-normal probability distribution, such as [21]. The log-normal distribution is expressed as:

$$p(\sigma_\chi) = \frac{1}{ln(10)\sqrt{2\pi}\sigma_1\sigma_\chi} e^{-\frac{(log\sigma_\chi - m_{\sigma_\chi})^2}{2\sigma_1^2}} \tag{4.6}$$

with m_{σ_χ} being the mean value of $\log \sigma_\chi$ and σ_1 the standard deviation of $\log \sigma_\chi$.

If σ_χ is log-normal distributed, logically $\log \sigma_\chi$ is normally distributed, and therefore $\log \sigma_\chi^2 = 2 \log \sigma_\chi$ is also normally distributed and the variance will be log-normal. For sake of brevity the equation is omitted but can be found at [44].

Both distributions will be compared further on with our measured data, to verify if there is a relation.

4.3 Prediction models

In the last years, scintillation has been a subject of studies in order to predict its behaviour. As it can only be modelled statistically, several database were used to develop and test the models. Scintillation, as described previously, is the signal level log-amplitude fluctuations, χ, due to turbulent atmosphere, and its intensity is described by the variance σ_χ^2 (in decibels) in a short-term basis. However, in a long term basis, the meteorological conditions are not constant and scintillation cannot be considered a stationary process. So the σ_χ^2 ceases to follow a Gaussian distribution and assumes a log-normal one. Mousley and Vilar [21] developed a model based on the previous assumed distributions but, since it requires the full measurements of χ over the prediction period, it is not adequate in practical cases.

Other models, with easier approaches, followed up.

The Karasawa model

The Karasawa method predicts the standard deviation with [32]:

$$\sigma_{pre} = \sigma_{ref}\sqrt{f^{0.9}G(D_e)/\sin^{2.6}\theta} \tag{4.7}$$

The σ_{ref} value has been found to be related with local meteorological parameters, therefore, the scintillation can be predicted at other sites.

Additionally, this model gives the expressions to obtain the cumulative distributions of the scintillation amplitude. The model assumes that the short-term standard deviations follows a Gamma distribution, instead of the generally assumed Gaussian distribution.

The antenna smoothing gain, mentioned previously in equation (3.42), is needed for all the models.

The annual scintillation enhancement distribution y, exceeded for a time percentage of P, is given by:

$$y = -(0.0597log^3P - 0.0835log^2P - 1.258logP + 2.672)\sigma_{pre} \tag{4.8}$$

with σ_{pre} as the long-term signal standard deviation, considering a one-year period and where P ranges from 0.01% to 50%. However, for the signal fades the relation is given by:

$$y = -(0.061log^3P - 0.072log^2P - 1.71logP + 3.0)\sigma_{pre} \tag{4.9}$$

The reason why fade and enhancement have different expressions is due to the already described asymmetry in the short-term scintillation amplitude.

$$\sigma_{ref} = 3.42 \times 10^{-3} + 1.186 \times 10^{-4}N_{wet} \tag{4.10}$$

For this model the wet part of the refractivity is given by:

$$N_{wet} = \frac{22790RHe^{19.7T/(T+273)}}{(T+273)^2} \tag{4.11}$$

For our calculation we have used the steps given in [10]. Through equations (4.8) and (4.9) and considering a $\sigma = 0.1$ dB this model was simulated and the following Figure 4.1 shows that the fades are more pronounced.

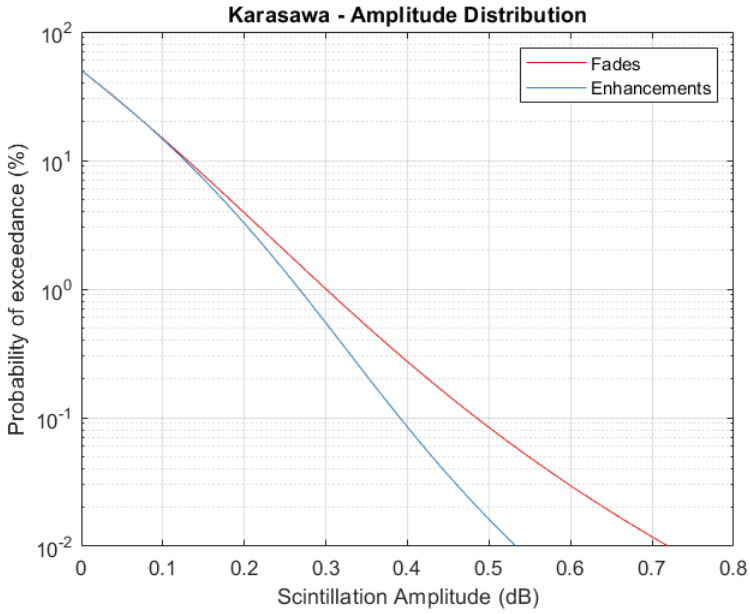

Figure 4.1: Fades and enhancements distribution: Karasawa model.

The ITU P.618-8 model

This model has a similar approach to the Karasawa one. It is used for links with elevation angles higher than 5° and frequencies ranging from 7 to 14 GHz. However, it has been tested up to 20 GHz at least [45].

The input parameters are:

- T: Average monthly temperature ($^{\circ}C$);
- RH: Average monthly relative humidity (%);
- f: frequency (GHz) and $4 \leq f \leq 20$;
- θ: elevation angle and $\theta \geq 5^{\circ}$;
- D: diameter of the earth-station antenna (m);
- η: antenna's aperture efficiency (%).

The standard deviation expression is:

$$\sigma_{pre} = \sigma_{ref} \sqrt{G(x) * f^{7/6} / \sin^{2.4} \theta} \tag{4.12}$$

and relies on an auxiliary calculation for the antenna averaging factor, through the equation (3.39) and the length of the turbulent path L at (3.41), calculated with $h = 1000m$. Additionally, the reference standard deviation, σ_{ref}, which is dependent on the meteorological data, is given by:

$$\sigma_{ref} = 3.6 \times 10^{-3} + 10^{-4} N_{wet} \quad (dB) \tag{4.13}$$

Differently from Karasawa, the N_{wet} is given by:

$$N_{wet} = \frac{22810 \times RH \times e^{17.5T/(T+240.97)}}{(T+273)^2} \quad (ppm) \tag{4.14}$$

For a time percentage, P, in between 0.01% and 50% the fade CCDF $A(P)$ is given by:

$$a(P) = -0.061(logP)^3 + 0.072(logP)^2 - 1.71logP + 3.0 \tag{4.15}$$

$$A(P) = a(P)\sigma_{pre} \quad (dB) \tag{4.16}$$

All the parameters are averaged values over a period of at least one month.

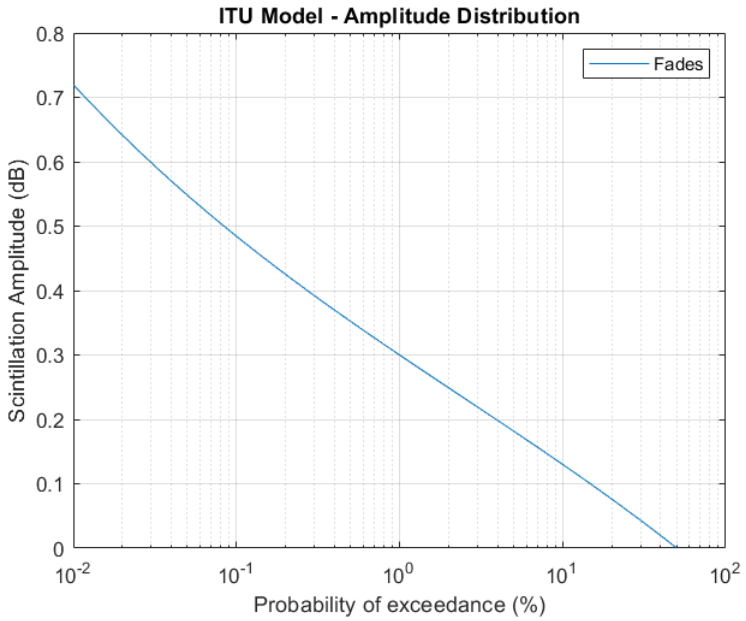

Figure 4.2: ITU model for scintillation fades depth.

For the simulation that can be observed in Figure 4.2, σ_{pre} was assumed to be 0.1 dB. Taking into account Figure 4.1 it is clear the similarity of both models.

Otung model

In the year 1996, Otung [46] proposed the following model that gives predictions for the annual and worst-month cumulative distributions of scintillation fades χ_- and enhancements χ_+ and, as well, the peak-to-peak scintillation amplitudes. This model resembles the ITU version: the main difference lays on the technique used to develop the standard deviation equations. Whereas the ITU model was developed empirically, the Otung expression is based on the Tatarsky's theory. This prediction model bases its calculations on the following standard deviation:

$$\sigma_{pre} = \sigma_{ref}\sqrt{f^{7/6}G(x)/\sin^{11/6}\theta} \quad (dB) \tag{4.17}$$

where $G(x)$ is the antenna averaging factor given on equation (3.39) and the reference standard deviation is σ_{ref}:

$$\sigma_{ref} = 3.6 \times 10^{-3} + 1.03 \times 10^{-4} N_{wet} \quad (dB) \tag{4.18}$$

where N_{wet} is the wet term of tropospheric refractivity:

$$N_{wet} = \frac{3.73 \times 10^5 e}{(T + 273)^2} \quad (ppm) \tag{4.19}$$

and e and T are the water vapour pressure (hPa) and the temperature averaged over one month.

The model has the advantage of giving the following annual distribution models with the standard error and correlation coefficient squared [46]. The next equations consider $0.01\% \leq P \leq 50\%$.

Annual distribution equations:

$$\chi_{-a}(P) = 3.6191 \exp\left[-9.50142 \times 10^{-4}/P - (0.40454 + 0.00285P)\ln(P)\right]\sigma_{pre} \tag{4.20}$$

$$\chi_{+a}(P) = 3.1728 \exp\left[-0.0359654P - (0.272113 + 0.0048P)\ln(P)\right]\sigma_{pre} \tag{4.21}$$

$$\chi_{pkpk_a}(P) = 15.6912 \exp\left[2.25734 \times 10^{-5}/P^2 - 0.011558P - 0.216784\ln(P)\right]\sigma_{pre} \tag{4.22}$$

$$\sigma_{\chi_a}(P) = 3.1728 \exp\left[-0.0359654P - (0.272113 + 0.0048P)\ln(P)\right]\sigma_{pre} \tag{4.23}$$

Worst-Month Distribution models:

Alongside with the annual distribution, the following distributions of scintillation values exceeded during $P\%$ for the worst-month, are as well display here. To clarify, equations (4.24), (4.26) and (4.27) are valid for $0.03 \leq P \leq 50\%$ and equation (4.25) is valid for $0.01 \leq P \leq 50\%$

$$\chi_{-wm}(P) = 6.8224 \exp\left[-10^{-4}(913.12/P + 1.8264^2) - (0.023027/P + 0.51664)\ln(P)\right]\sigma_{pre} \tag{4.24}$$

$$\chi_{-wm}(P) = 5.5499 \exp\left[-10^{-4}(946.864P + 4.4974P^2) - (0.023573P - 0.2261135)\ln(P)\right]\sigma_{pre} \tag{4.25}$$

$$\chi_{pkpkwm}(P) = 21.5895 \exp\left[(2.21698 \times 10^{-4}/P^2) - 0.0145353P - 0.204576\ln(P)\right]\sigma_{pre} \tag{4.26}$$

$$\sigma_{\chi w}(P) = 4.9157 \exp\left[(1.85218 \times 10^{-4}/P^2 - 0.0435448P - [0.26467 - 0.0078851P]\ln(P)\right]\sigma_{pre} \quad (4.27)$$

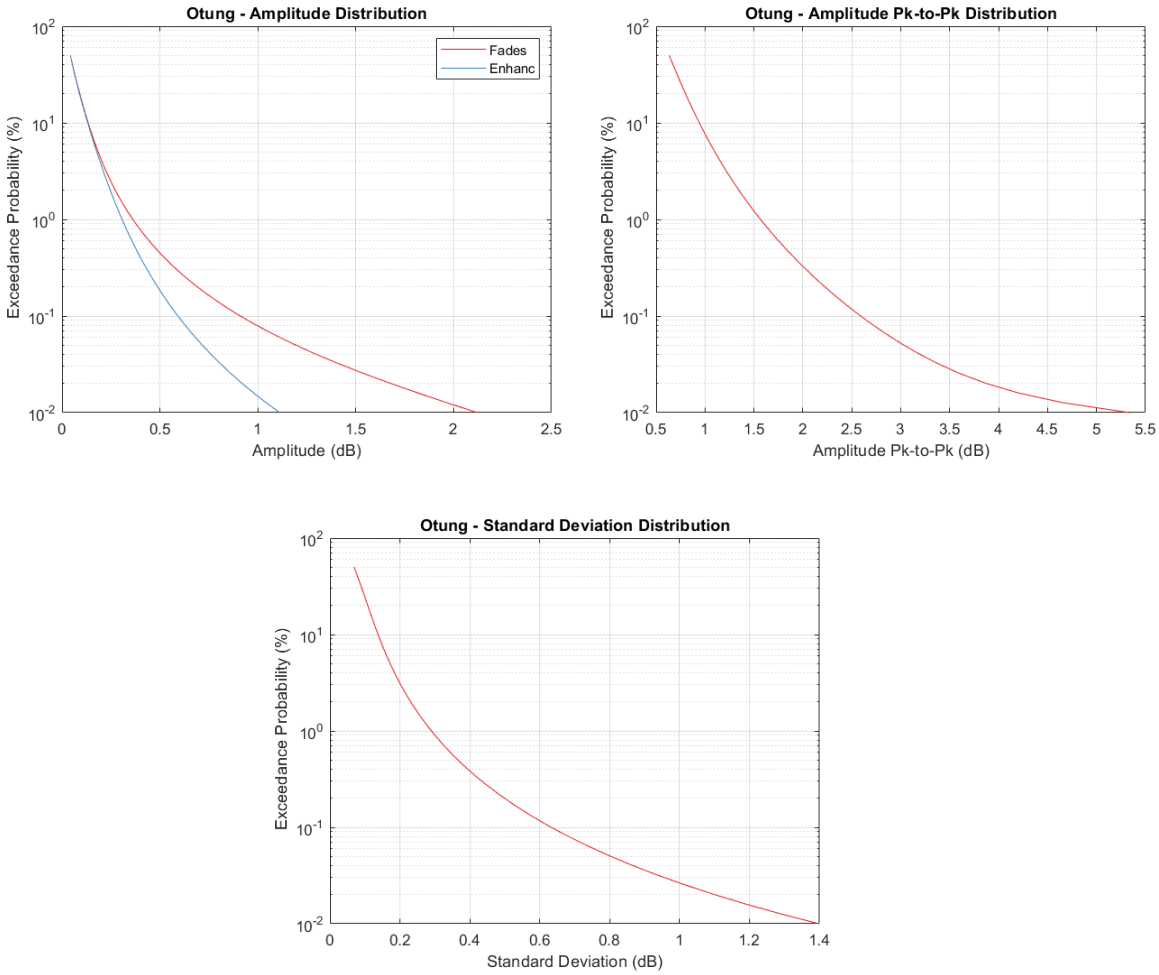

Figure 4.3: Otung model for scintillation amplitude (top-left), amplitude pk-to-pk (top-right) and standard deviation (bottom).

The equations were implemented with $\sigma_{ref} = 0.1$ dB and the results are depicted in the Figure 4.3, in order to compare the amplitude distribution with the other models.

As it can be seen, this model in particular gives higher values for the fades and enhancements in comparison with the ITU and the Karasawa models.

Ortgies-N and Ortgies T-model

Using data collected in Darmstadt at 12.5 GHz, 20 GHz and 30 GHz, during the Olympus campaign (Olympus satellite), Ortgies proposed another model [32].

Ortgies, first presented expressions for the monthly mean value of the variance, σ_χ^2, instead of the usual mean value of standard deviation, σ_χ. The main goal was, as well, to relate the

standard deviation to the surface N_{wet} (hence the name Ortgies-N) and is given by:

$$m = \left\langle \ln(\sigma_\chi^2) \right\rangle = \ln\left[G(x) f^{1.21} \sin^{-2.4}\theta\right] + (-13.45 + 0.0462\langle N_{wet}\rangle) \tag{4.28}$$

The second expression, relates to the surface temperature, T, and hence the name, Ortgies-T model.

$$m = \left\langle \ln(\sigma_\chi^2) \right\rangle = \ln\left[G(x) f^{1.21} \sin^{-2.4}\theta\right] + (-12.5 + 0.0865\langle T\rangle) \tag{4.29}$$

Van de Kamp model

The Van de Kamp model is somewhat different comparing to all the others mentioned above. Van de Kamp noticed an even better correlation between the scintillation and the presence of cumulus clouds than only with the wet refractivity. In fact, Tervonen *et al* [35] emphasized the same theory and proved that the average variation is more strongly correlated with the cumulus cloud activity along the propagation path. A new term indicating the average water content of heavy clouds W_{hc} is added to the model at the expense of the wet refractivity. The term heavy clouds is used to refer layered clouds with an integrated water content greater than 0.70 kg/m^2. An improved prediction model, according to the author, is given by:

$$\sigma_{ref} = 0.98 \times 10^{-4}(N_{wet} + Q) \quad (dB) \tag{4.30}$$

where Q is a long-term average parameter:

$$Q = -39.2 + 56\langle W_{hc}\rangle \tag{4.31}$$

and <> denotes long-term average, at least annual. The final prediction of the scintillation standard deviation is:

$$\sigma_{pre} = \frac{\sqrt{G(x) f^{0.45}}}{\sin^{1.3}\theta}\sigma_{ref} \quad (dB) \tag{4.32}$$

where G(x) is given in (3.39).

Van de Kamp demystifies the Gaussian short-term distribution of the scintillation signal, by affirming that the main cause of scintillation is the turbulence in clouds which are a thin layer far from the receiver which leads to a Rice-Nagakami distribution and, thus, the distribution is asymmetrical.

Finally, the model takes the following approach [35]:

- First, the distribution of signal fade, $y_f(P)$:

$$y_f(P) = \gamma(P) + \delta(P) \quad (dB) \tag{4.33}$$

- Second, the distribution of signal enhancement, $y_e(P)$:

$$y_e(P) = \gamma(P) - \delta(P) \quad (dB) \tag{4.34}$$

with following expressions to represent the fitted curves to the results:

$$\gamma(P) = (-0.0597 log^3 P - 0.0835 log^2 P - 1.258 log P + 2.672)\sigma_{pre} \tag{4.35}$$

$$\delta(P) = (0.100log^2P - 0.375logP + 0.297)\sigma_{pre}^2 \tag{4.36}$$

where σ_{pre} is the long-term standard deviation (dB).

The simulation for the model used $\sigma_{pre} = 0.1$ dB. Unlike the other models, the Van de Kamp has similar curves for the fades and enhancements distribution, as can be seen in Figure 4.4.

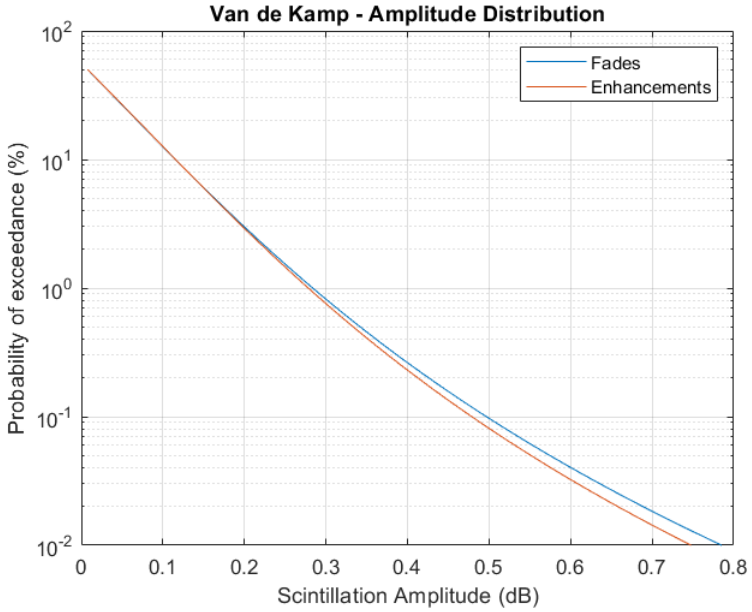

Figure 4.4: Fades and enhancements distributions: van de Kamp model.

Chapter 5

Experimental data processing and statistical analysis

5.1 Introduction

This chapter describes the experimental support aspects of this dissertation. Section 5.2 presents the overall project and some details. A description of the equipment used is available on section 5.3. Section 5.3 portrays the data available for this dissertation, and how it is stored. The following section, 5.4, describes the methods used to convert the measurements to physical data and, mainly, how scintillation is extracted, filtered and stored. The handling of meteorological data is, as well, detailed.

5.2 Experiment description

There has been a continued effort from ESA to support propagation campaigns in Europe: the support has been made by providing sources (satellite payloads) and funding for experimenters in Europe. The IT-Av (Instituto de Telecomunicações-Aveiro Pole) has been involved in an ESA project related with a large scale (continental) characterization of the earth-satellite propagation channel in Europe together with other researchers: see [47].

This campaign was started in the framework of the experimental opportunities offered by the Alphasat (Inmarsat4A-F4) satellite that carries dedicated Scientific Payloads to address propagation issues: channel measurements and advanced telecommunications experiments [48]. Other researchers, not involved directly in the consortium, have joined to the experimental campaign improving the geographical coverage of Europe [49].

Table 5.1: Geographical coordinates of the IT-Av beacon receivers.

Station	Geographical coordinates		
	Latitude	Longitude	Altitude
IT-Av	40.612^{o}N	8.662^{o}W	12 m

The city of Aveiro located geographical at the latitude and longitude in Table 5.1, has a continental maritime climate that is substantially different from the other sites, that usually have colder winters or are significantly continental.

Table 5.2: Beacons characteristics.

	Ka-Band	Q-Band
Frequency	19.680 GHz	39.402 GHz
Polarization	linear vertical	linear with a 45º angle
Larger gain zone	32.5ºN, 20ºE	45.4ºN, 9.5ºE
EIRP	19.5 dBW	26.5 dBW

The IT-Av experimental site has two beacon receivers measuring two distinct satellites (with two distinct frequencies) and a local dedicated meteorological station, with the characteristics displayed in Table 5.2.

One of the receivers monitors the Ka-band beacon at 19.68 GHz of the Ka-Sat geostationary satellite. The receiver uses a 1.5 m offset antenna and has an OMT able to separate two linear orthogonal polarizations that has allowed to study the depolarization properties of the channel [50]. The antenna is on the roof of the Department of Electronics, Telecommunications and Informatics (DETI). The front-end was recently refurbished with ESA funding and allowed to extend the attenuation dynamic range by 4 dB (Figure 5.1). The beacon signal is converted to an audio frequency signal and acquired by a LabView data acquisition card and a Labview application performs the two beacon channels (copolar and crosspolar) detection using FFT techniques: the data is stored at 8 S/s.

(a) Receiving antenna and front-end at DETI: Ka-band.

(b) Ka-band receiver indoor part: hardware and acquisition PC.

Figure 5.1: Ka-band receiver.

The second receiver monitors the Q-band beacon at 39.402 GHz from the Alphasat geostationary satellite. The receiver uses a 0.62 m Cassegrain antenna that is installed in an office, looking through a window. This solution has proved to be very convenient because of the more controlled room temperature (less gain variations), a cheaper development, less hardware degradation and easier maintenance. The receiver measures only one polarization (no OMT) and the analogue part–down to 142 MHz (last IF) is very small and compact, as can be observed in Figure (5.1b). The receiver requires an antenna pointing system because the satellite has an increasing inclination that must reach a maximum of 3º before it starts reducing again [51]. The beacon amplitude is detected with FFT techniques after being sam-

pled by a Software Defined Radio (SDR) and the data is stored at 8 S/s. More details can be found at [52].

Figure 5.2: An aspect of the Q-band beacon receiver: the antenna, down converters and antenna pointing actuators (left) and SDR, antenna controller, reference frequency source and data acquisition (right).

The meteorological station is made of separate parts (Figure 5.3). It comprises the measurement of the relative humidity, the temperature, the pressure, the wind speed and the rain rate with two sensors: a tipping bucket, providing a resolution of 6 mm/h and a drop counter, offering a resolution of 0.3 mm/h. These equipment's are all from Thies-Clima. The pressure sensor was built around the barometric BARO-A-4V-MINI module that performs incredible well by comparing the readings with the ones of a nearby meteorological station. The acquisition is made by the aforementioned LabVIEW card and a LabVIEW application. The two digital counters of the data acquisition card are used to count the number of tipped buckets or fallen drops in 1 second, thus, enabling the study of the effects of integration time on the cumulative distributions of rain rate.

Figure 5.3: Wind speed and wind shield containing temperature and humidity sensors (left); the two rain gauges (right).

5.3 Data description

The raw acquired data - beacon and meteorological data - is subject to a pre-processing software developed in the framework of the current project [53]. Its main goals are: loading the data, converting it to physical units, doing a quality inspection followed by a reparation of corrupted samples if needed or possible. After that, the equipment bias effects on the beacon measurements is removed by performing templates extraction (expected values in clear sky) followed by a bias removal using these templates.

This software is run on a day basis to explore the often observed daily variations. However, in order to process correctly the edges of each day -meaning the beginning and the end- three days are loaded: the day before, the day to be processed and the following day.

All the time series are stored with a corresponding flag that qualify the data into four categories:

- *Valid (0)*: Data with this flag did not suffer alterations in the pre-processing. Ready to be used in statistical analysis for the propagation channel;
- *Invalid (1)*: This data has inconsistencies and cannot be used in statistical analysis;
- *Repaired (4)*: Similar as the invalid, but were modified in the pre-processing and are ready to be used in the statistical analysis if the user wants;
- *Interpolated (5)*: When data could not be acquired for some reasons it was interpolated (usually used for short duration gaps).

Data is stored in MatLab data structures named: AlphaSat and KaSat (Table 5.3) and Meteo (Table 5.4). The first two are dedicated to the beacons sampled at a rate of 8 S/s and 1 S/s. The time stamps are also stored in the format *datenums* that are real time values represented by the difference between the collection instant and the date 0/1/0000.

All the data is stored in a single file per day using the following format: **ProYYYYMMDD**.mat.

The complete data structure for the two links is:

Table 5.3: Structure for the Ka-band data (left) and structure for the Q-band data (right).

CPA8	TS
	FLAG
CPA1	TS
	FLAG
NSD1	TS
	FLAG
TimeStamps1	-
TimeStamps8	-
XPD	In
	Qu
	FLAG

CPA8	TS
	FLAG
CPA1	TS
	FLAG
NSD1	TS
	FLAG
TimeStamps1	-
TimeStamps8	-

Table 5.4: Structure for the meteorological data.

Humidity	TS
	FLAG
Temperature	TS
	FLAG
Wind Speed	TS
	FLAG
Wind Direction	TS
	FLAG
Pressure	TS
	FLAG
Drop Counter	FLAG
	Counts
	Rain
	IntTime
Tipping Bucket	FLAG
	Counts
	Rain
	IntTime

5.4 Data processing

An important factor that limits the performance of communication systems is the thermal noise: either received by the antenna (clouds, rain or emission by gases) or generated inside the receiver. Also, the propagation beacon measurements are affected by noise so a ground floor scintillation variance is always present, even with no scintillation.

The variance induced by the thermal noise can be estimated by:

$$\sigma_{tm}^2 = \frac{(20 \log e)^2}{10^{\left((C/N)/10\right)}} \quad (dB^2) \tag{5.1}$$

Thermal noise and the scintillation must be decorrelated so the measured (total) scintillation variance, σ_t^2, must be given by:

$$\sigma_t^2 = \sigma_{tm}^2 + \sigma_\chi^2 \quad (dB^2) \tag{5.2}$$

where σ_{tm}^2 is the thermal noise variance and σ_χ^2 is the scintillation variance. Table 5.5 presents these values for both receivers.

Table 5.5: Thermal noise variance for the different bands.

	AlphaSat	Ka-Sat (until May of 2018)	Ka-Sat (from Jun of 2018 until now)
CNR (dB)	56 - 57	53	56 - 57
$\sigma^2_{tm}(dB^2)$	0.0015	0.003	0.0015
$\sigma_{tm}(dB)$	0.0387	0.0548	0.0387

The first goal of this dissertation is to extract the scintillation time series from the copolar attenuation time series stored at 8 S/s, for further statistical scintillation oriented analysis. Also the scintillation variance is computed and stored. The approach permits to speed up several statistical analyses by just loading the scintillation related data rather than calculating it each time a new statistical analysis is performed.

The copolar attenuation time series can contain the attenuation due to clouds and rain, and the scintillation. The attenuation time development is a very slow process: the Fresnel ellipsoid is filled with rain at a relatively low velocity and not all the volume at the same time. Such is not the case with scintillation, which is caused by a more agile physical mechanism. If the power spectrum of several events comprising attenuation is computed it is possible to observe a spectrum decaying at about 20 dB/decade down to a flat value in a certain frequency range and, then the spectrum decays again. The frequency at which the spectrum starts to become flat is about 0.01 to 0.025 Hz.

The following Figure 5.4 and Figure 5.5 show the signal for a brief period of time at 19 of June of 2017. In this day, it was observed some early night rain, followed by a moderate scintillation period. Observing this period of the day, it can be seen, as mentioned before, a slower section of events where the spectrum decays slower. This is due to the attenuation events. The next section of the spectrum belongs to the scintillation phenomenon and is the most relevant and the study topic of this dissertation.

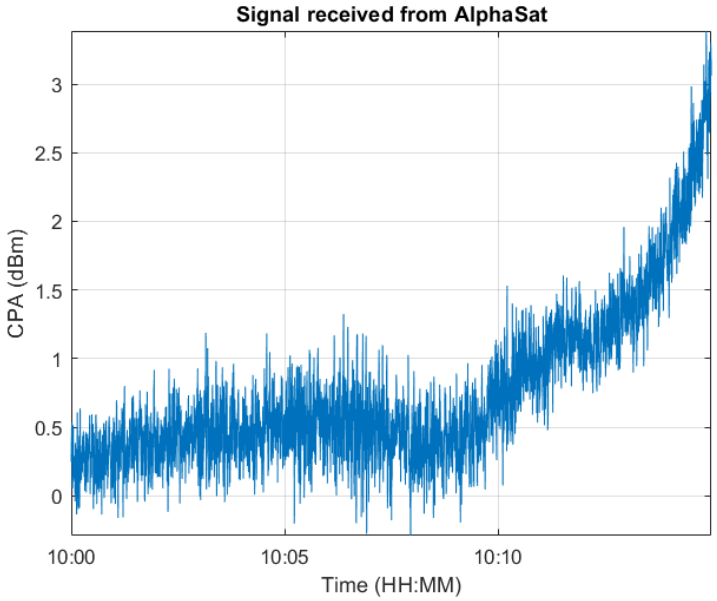

Figure 5.4: Copolar attenuation during a rain period.

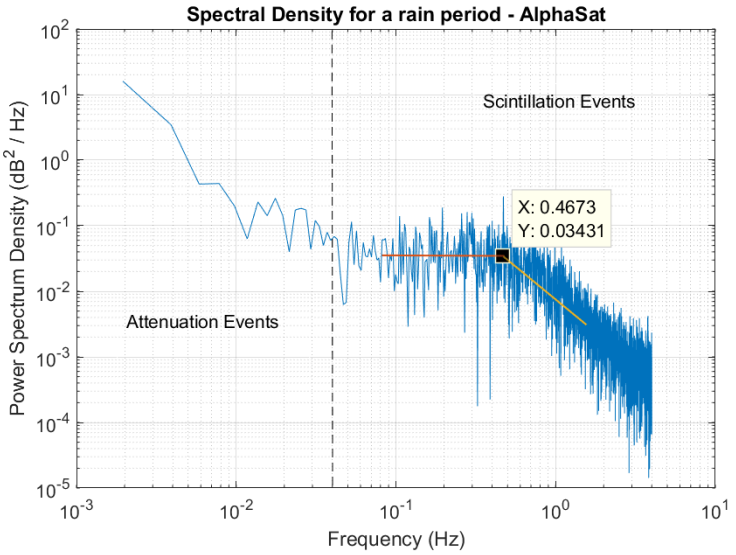

Figure 5.5: Corresponding signal spectrum from 19-Jun-2017 09:59:59 to 19-Jun-2017 10:14:59.

Usually, a low pass filter, with an integration time of several tens of seconds is used to estimate the attenuation and an high pass filter, with similar properties, is used to extract the superimposed scintillation time series. A widely accepted low-pass filter of the type raised-cosine -cos^2- is used for this purpose. After some trials, a raised cosine filter with a number of coefficients given by $f_s \times blocklength$, where $f_s = 8$ Hz and $blocklength = 28.76$ (seconds) was used to perform the task of separating the bulk attenuation effects (or eventually very slow gain variations of the receiver) and the scintillation time series. The attenuation data was decimated to 1 S/s and stored, to be used to exclude the scintillation data periods collected when the attenuation exceeds a defined threshold.

Figure 5.6 is the resulting signal from the low-pass filter.

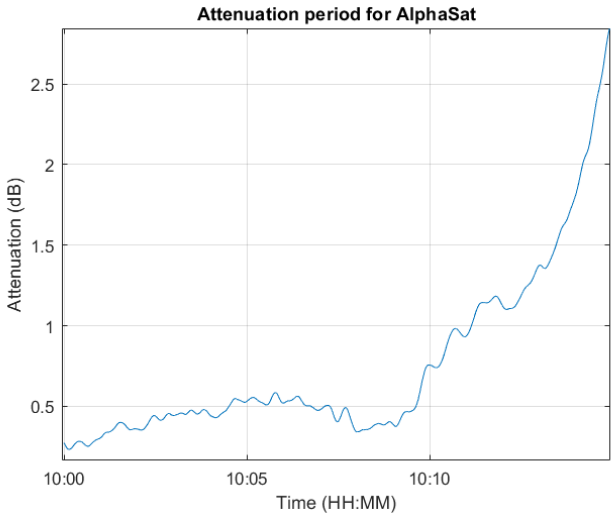

Figure 5.6: Extracted copolar attenuation (CPA) for 19-Jun-2017.

In order to obtain the scintillation signal we could have used a high-pass filter, but instead we opted to subtract the attenuation resulting from the low-pass filter from the initial time series (CPA). The following Figure 5.7 shows the final scintillation time series.

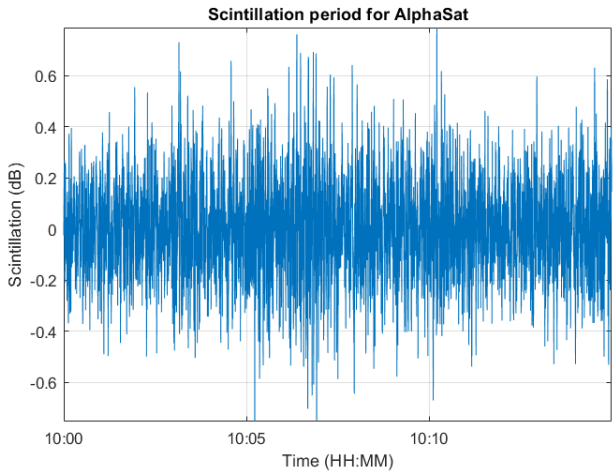

Figure 5.7: Extracted scintillation: positive values are fades and the negative ones enhancements.

Normally, the standard deviation or variance time series of the scintillation must be calculated. The standard deviation was performed by a moving average window with a block length of one minute that ran through all the daily scintillation time series. This function *movstd* is already built in MATLAB. Figure 5.8 shows the standard deviation signal. Finally, the standard deviation was decimated (as the attenuation) to 1 S/s.

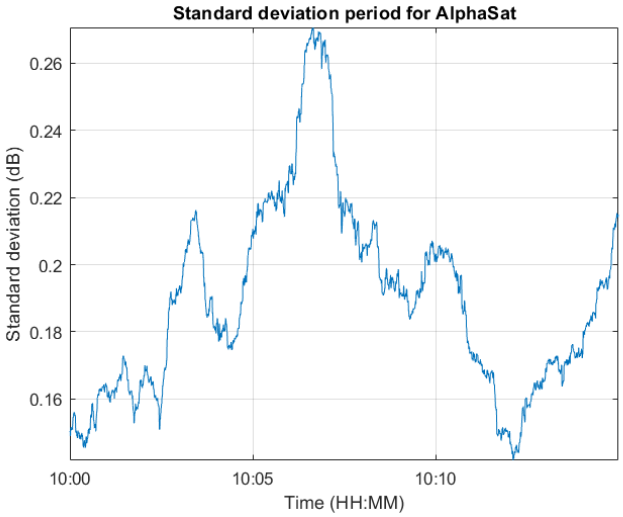

Figure 5.8: Scintillation standard deviation.

The meteorological data, except the rain rate, was filtered with a moving window using a similar filter but with a filter sized $f_s * blocklength$, where $f_s = 8$ Hz and $blocklength = 60 * 5$ (seconds) (that is 5-minute integration time).

Exceptionally, the water vapour density ρ that is not measured, was calculated from the other existing meteorological variables according:

$$\rho = \frac{216.7e}{T} \quad (g/m^3) \tag{5.3}$$

where e is the vapour pressure and T the temperature.

All the following structures in described Tables 5.6, 5.7, 5.8 and 5.9, containing the above described data, are stored in a single *.mat file per day with the (self describing) name **ProYYYYMMDDScint**.mat

Table 5.6: Structure for the Q-band beacon (left) and Ka-band beacon (right).

Qband	Scint	TS
		FLAG
	Attn	TS
		FLAG
	Stdev	TS
		FLAG
	TimeStamp	-

Kband	Scint	TS
		FLAG
	Attn	TS
		FLAG
	Stdev	TS
		FLAG
	TimeStamp	-

Table 5.7: Structure for the meteorological data.

Meteor	Hum	TS
		FLAG
	Press	TS
		FLAG
	WS	TS
		FLAG
	WD	TS
		FLAG
	DropCounter	TS
		FLAG
	Temp	TS
		FLAG
	AH	TS
		FLAG
	TimeStamp	TS

Table 5.8: Structure with the radio refractivity data.

Nwet	TS
	FLAG

Table 5.9: Auxiliary information about the data processing.

Info	FilterType	raised-cosine low pass filter	-
	IntegrationTimeMeteo	300	seconds
	WindowMovStd	481	samples
	IntegrationTimeMovStd	60	seconds

5.4.1 Dry scintillation validation

The scintillation time series was processed in order to consider only dry periods. An attenuation threshold was applied to discriminate between rain and clear sky periods. For the Ka band the threshold was 0.5 dB and for the Q-band 1 dB. Every time that the attenuation series reaches exceeds this values, the scintillation samples are replaced by NaN.

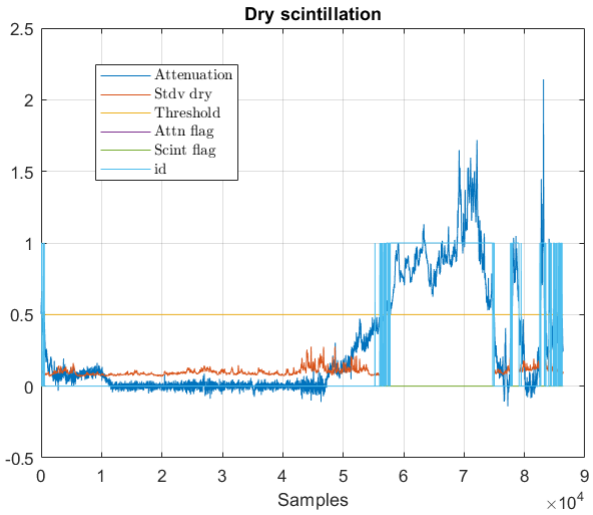

Figure 5.9: Dry scintillation validation.

The scintillation time series goes through other validation using the corresponding flags created during the scintillation extraction. Wherever the flag is equal to 1, the final scintillation time series is replaced with a NaN.

The Figure 5.9 shows a variable *id* that means: if the attenuation flag or the scintillation flag is equal to 1 or the attenuation is above the threshold, the scintillation samples must not be included for statistical calculations.

5.4.2 N_{wet} calculation

The N_{wet}, that is included in the data structures, was calculated following the ITU recommendation: see equation (2.6), [10]. Here, we presented an example for the N_{wet} in Figure 5.10.

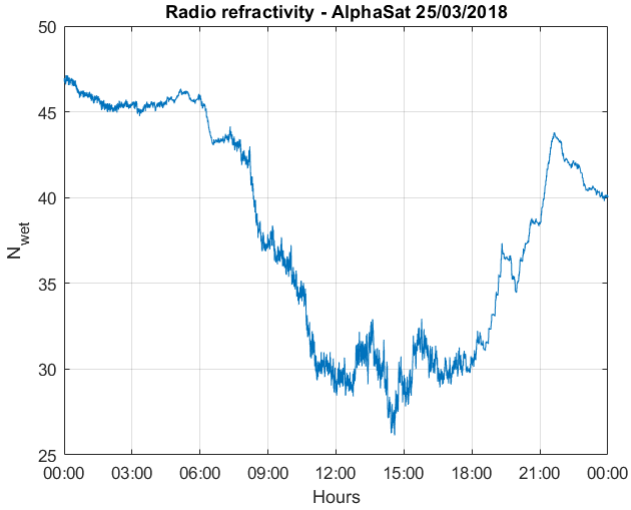

Figure 5.10: Radio refractivity in ppm.

The input parameters to calculate the N_{wet} value are the temperature ($^{\circ}C$) , relative humidity (%) and pressure (hPa). Throughout the day these values change resulting also in the variation of N_{wet}.

In order to understand this variation, all variables were normalized and plotted in Figure 5.11.

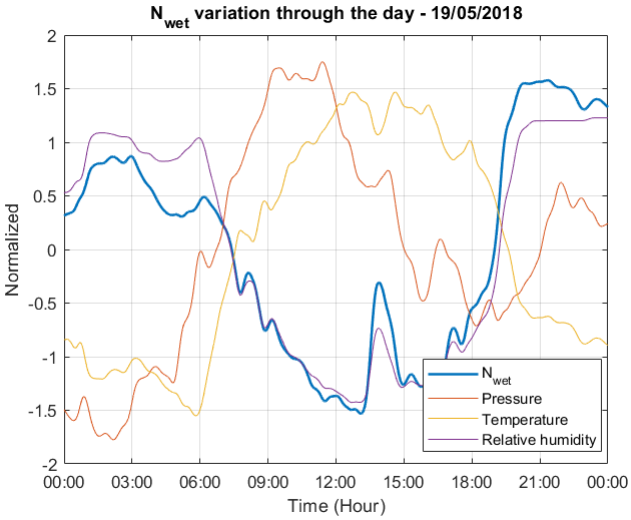

Figure 5.11: Radio refractivity along with temperature, relative humidity and pressure.

During the night, the temperature and pressure are low and the relative humidity is high, which leads to a higher value for the radio refractivity. During the day the N_{wet} seems to follow the relative humidity curve. The combination of this variables in the scintillation study is calculated in the next chapter.

Chapter 6

Data analysis and models evaluation

6.1 Introduction

This chapter describes the methods used to perform the data analysis and processing. Section 6.2 analyses the relationship between the scintillation standard deviation and the meteorological parameters gathered locally. Also, it is shown an in-depth study of different linear regressions used to test the correlation between the scintillation standard deviation and the meteorological parameters. Section 6.3, rates the fitting of the available models and compares the results between the two beacons frequencies received at Aveiro. In section 6.4 it is studied the scintillation behaviour throughout the day. Followed by section section 6.5 where is observed the diurnal variation in a larger scale. The following section 6.6 it is dedicated to the scintillation frequency scaling. An important aspect about the scintillation phenomenon is its spectrum. The last section 6.7 explores the analysis of the scintillation spectrum parameters.

6.2 Scintillation standard deviation and meteorological parameters

The relationship among the measured meteorological parameters and the scintillation measured in the two links will be explored. The literature about this subject is scarce and often, most of the meteorological data, used in the available publications, is not collected at the same site and the quality control is out of the scope of the propagation experimenter. At IT-Av the meteorological equipment has been available all the time, the data has been screened and the quality asserted.

The relationship of the scintillation with the following meteorological parameters will be analyzed:

- Relative humidity;
- Water vapour density;
- Temperature;
- Pressure;
- Wet refractivity N_{wet}.

A set of 2D histograms were produced for the two beacons, relating the standard deviation and the listed meteorological parameters. The time series of the hourly integrated values were

used and the statistics were performed in a monthly and yearly basis. The 2D histogram can also be used to derive the probability density function of each variable in the histogram.

For example, Figure 6.3 correlates the standard deviation with the water vapour density in a annual basis.

The 2D histograms were generated using a built-in function called *histcounts2* available in MATLAB. The input parameters are: the standard deviation time series and the time series for the meteorological parameter in evaluation, plus the respective edges.

The edges values used are displayed in the Table 6.1.

Table 6.1: Edges used in 2D histograms.

Variable	**Standard deviation**	**Amplitude**	**Pk to Pk Amplitude**	**Temperature**
edges	0.01:0.01:1	-3:0.02:3	0:0.01:6	0:1:35
Variable	**Relative humidity**	**Water vapour density**	**Pressure**	**Nwet**
edges	1:1:100	0:0.5:30	980:1:1045	0:2:110

The following plots were obtained from the 2D probability density function normalized to the maximum value and the contour lines are logarithmically spaced. Equation (2.6) illustrates the usually assumed principal indicator of scintillation. The N_{wet} histogram, in Figure 6.1, is expected to be proportional to the scintillation intensity at least in a long term basis. The higher the ground measured atmospheric refractivity the larger should be the scintillation amplitude and consequently the scintillation variance.

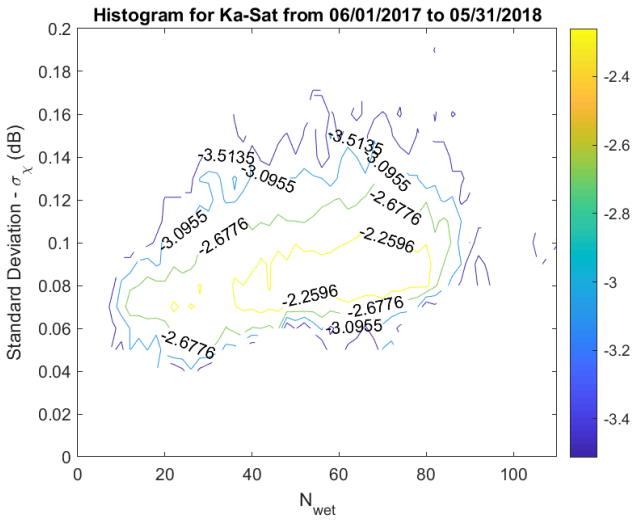

Figure 6.1: 2D Histogram for N_{wet}.

The correlation coefficients between the scintillation intensity and the ground based atmospheric variable are listed in Table 6.2. Through the already mentioned equation (2.6), it is obvious a positive correlation with temperature. For this reason, the higher the temperature the most likely is the observation of more intense scintillation. Figure 6.2 illustrates the correlation described.

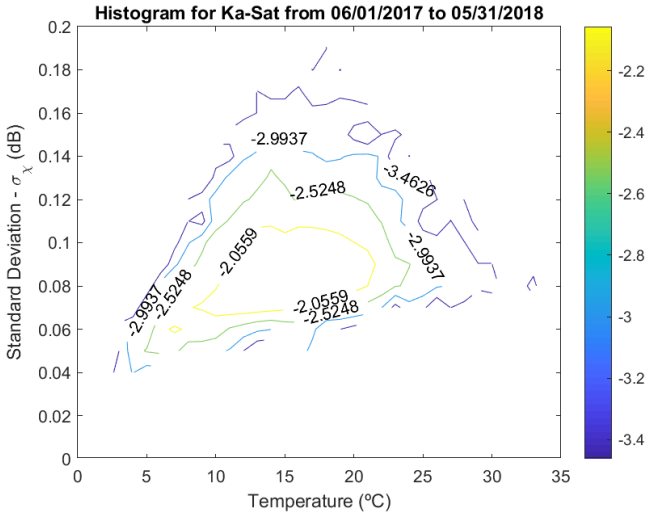

Figure 6.2: 2D Histogram for the temperature.

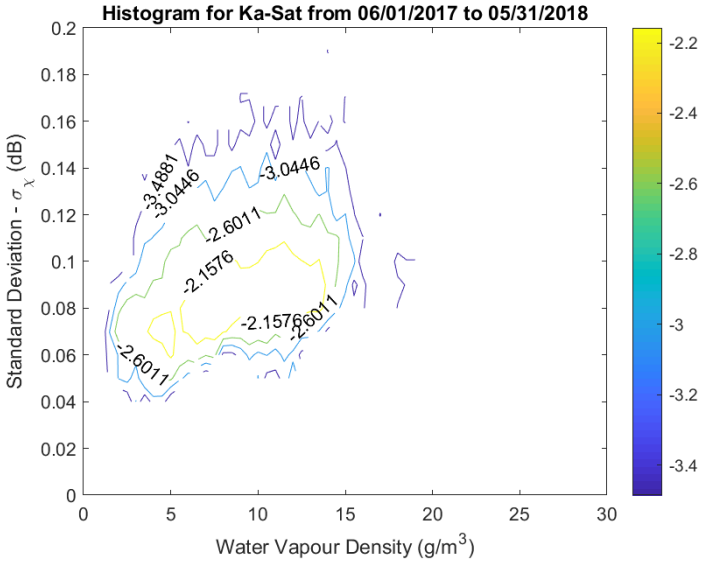

Figure 6.3: 2D Histogram for the water vapour density.

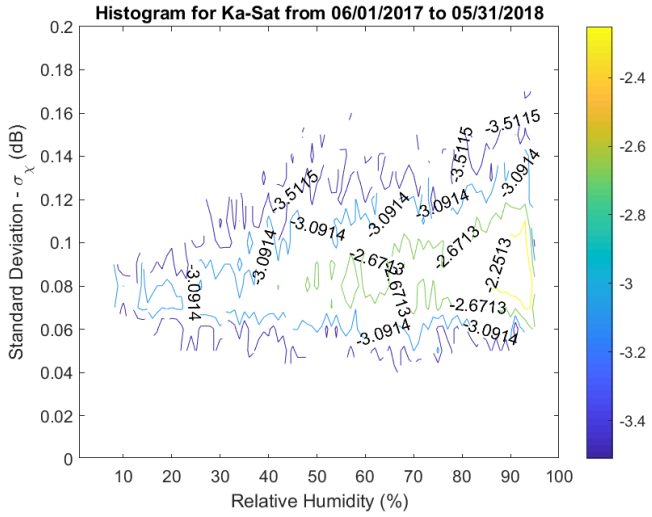

Figure 6.4: 2D Histogram for the relative humidity.

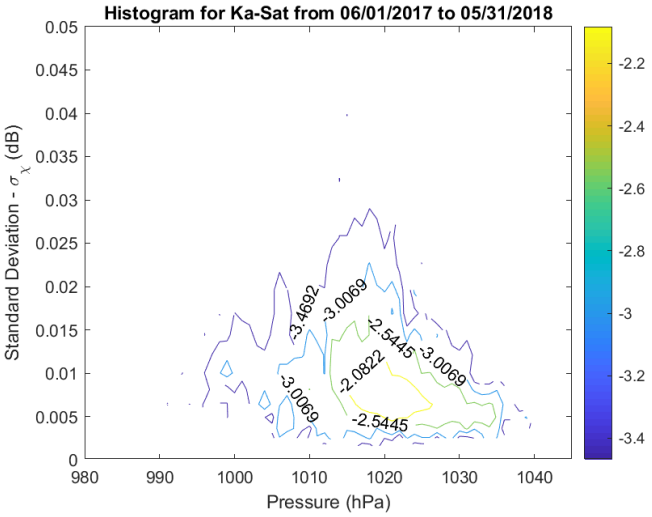

Figure 6.5: 2D Histogram for the atmospheric pressure.

Table 6.2: Correlation between scintillation standard deviation and the meteorological parameters.

Meteorological Parameters	Correlation at Ka-band	Correlation for Q-band
Temperature ($^{\circ}C$)	0.34	0.36
Pressure (hPa)	-0.31	-0.29
Water Vapour Density (g/m^3)	0.33	0.35
Relative Humidity (%)	0.14	0.12
N_{wet}	0.33	0.34

Table 6.2 summarizes the correlation between the standard deviation and the meteorological parameters, displayed in the Figures 6.2, 6.5, 6.3, 6.4 and 6.1 confirming the conclusions discussed in this section. A not negligible correlation between the referred meteorological parameters and the scintillation variance is observed for an integration time of 1 hour. It is well known that the weather change is only perceived at ground level when other observations has already changed: for example high altitude clouds, pressure changes, etc. The monthly analysis also depicts the same trend in spite of a more "unstable" results due to a smaller number of samples. It is interesting to observe that the standard deviation shows a somewhat higher correlation with other parameters, rather than the relative humidity.

The scintillation phenomenon arises from several meteorological parameters that contribute to the turbulence. As an attempt to model the relationship between them a linear regression was tried. In this particular case a MATLAB function, called *fitlm*, creates a multivariate linear regression in the following form:

$$y = \beta_0 + \beta_1 X_1 + \beta_2 X_2 + \beta_3 X_3 + \beta_4 X_4 + \beta_5 X_5 + \epsilon \tag{6.1}$$

where β_n are the regression coefficients and β_0 is the intercept. The X_n are known as the regressors which, in this situation, are the meteorological parameters. The last part of the equation, ϵ, is the error of the model. It captures all the terms that influence the y value other than the X_n [54].

The results of the estimated coefficients are shown in the first column. The **SE** (estimation standard error) column measures how precise the estimation of the coefficients is. The smaller the value the more precise the **Estimate** value is. The *tStat* values are calculated by dividing the coefficients (**Estimate** column) by the standard error (**SE** column).

In statistics, the null hypothesis is a theory that states if there is no relationship among the measured variables. The *pValue* or significance, verifies and proves if this statistical hypothesis is false or not. This test attempts to show if the results are impractical conclusions. If the *pValue* is higher than 0.05 it means that the null hypothesis is verified meaning that the coefficient is insignificant for the model.

Figure 6.6 shows that the variable **WaterVapour** has a **pValue** equal to 0.1447, which discloses that this variable does not contribute to the model.

Another important parameter that helps to evaluate the model veracity is the R-squared. This value is known as the coefficient of determination. Usually, the R-squared value is between 0 and 1 and measures how much of y is explained by the linear relation [54]. As seen, the R-squared value is 0.232 which is considered a low value, leading to conclude that the model has a weak linear relation.

To prove that the correlation coefficients of table 6.2 are in agreement with the R-squared value, this value was calculated through:

$$R^2 = r_{y,X_n}^T r_{X_n,X_n}^{-1} r_{y,X_n} \tag{6.2}$$

where r_{y,X_n} is a vector with all the correlation coefficients of table 6.2 and r_{X_n,X_n} is a correlation matrix that contains the correlation between each X_n variable. To obtain this matrix a MATLAB function was used *corrcov* and for the correlation coefficients was used *corrcoef*. The final value, 0.232, equals the one in Figure 6.6. This confirmation of the R-squared value and the higher value of the pValue lead to try new models.

Linear regression model:
Stdv ~ 1 + Pressure + Temperature + RH + Water_Vapour + Nwet

Estimated Coefficients:

	Estimate	SE	tStat	pValue
(Intercept)	1.6852	0.066154	25.474	5.8806e-138
Pressure	-0.0015957	6.4529e-05	-24.728	2.2152e-130
Temperature	0.0018077	0.00026752	6.7572	1.5004e-11
RH	-0.00049266	0.00017092	-2.8825	0.0039558
Water_Vapour	-0.028278	0.019387	-1.4586	0.1447
Nwet	0.005874	0.003444	1.7056	0.088125

Number of observations: 8423, Error degrees of freedom: 8417
Root Mean Squared Error: 0.0426
R-squared: 0.232, Adjusted R-Squared 0.232
F-statistic vs. constant model: 509, p-value = 0

Figure 6.6: Linear regression results for all the meteorologic parameters.

The next attempt begins with discarding from the model the variable that had higher pValues remaining the fundamental variables. However, was thought that as the N_{wet} is calculated from the other variables we could be adding the same weight from the same variables again. Results obtained by removing the WaterVapour and the N_{wet} are displayed in Figure 6.7:

Linear regression model:
Stdv ~ 1 + Pressure + Temperature + RH

Estimated Coefficients:

	Estimate	SE	tStat	pValue
(Intercept)	1.6588	0.066377	24.99	5.0195e-133
Pressure	-0.0016029	6.4809e-05	-24.733	1.9795e-130
Temperature	0.0039377	0.00010367	37.982	1.6173e-291
RH	0.00040339	2.1769e-05	18.53	3.6309e-75

Number of observations: 8423, Error degrees of freedom: 8419
Root Mean Squared Error: 0.0428
R-squared: 0.225, Adjusted R-Squared 0.225
F-statistic vs. constant model: 816, p-value = 0

Figure 6.7: Linear regression for the fundamental meteorological parameters.

Attending to the **pValue** column the RH value decreased, meaning that the probability of being significant to the model increased. However, the R-squared remains small which created doubts about the models order.

To contour this issue the models order was change to 2.

$$y = \beta_0 + \beta_1 RH + \beta_2 P + \beta_3 T^2 + \epsilon \tag{6.3}$$

Figure 6.8 shows an increase in the Temperature effect on the model. However, the R-squared continues to not be satisfactory.

```
Linear regression model:
    Stdv ~ 1 + Pressure + RH + Temperature^2

Estimated Coefficients:
                      Estimate        SE         tStat      pValue
                    ____________    ___________    _______    ___________

    (Intercept)        1.7105        0.066867      25.581    4.6473e-139
    Pressure        -0.0016276     6.5375e-05     -24.897     4.453e-132
    RH              0.00044338     2.2296e-05      19.886     4.9508e-86
    Temperature^2   0.00012058     3.3915e-06      35.554    4.4199e-258


Number of observations: 8423, Error degrees of freedom: 8419
Root Mean Squared Error: 0.0432
R-squared: 0.211,  Adjusted R-Squared 0.211
F-statistic vs. constant model: 750, p-value = 0
```

Figure 6.8: Linear regression results for a model of order two.

Returning to the equation (2.6) it is noticeable the dependence with the pressure of the water vapour content. Discarding the N_{wet} is also discarding all contributions of the pressure of the water vapour content. Noting that is better to have a model of lower complexity and less terms, which makes using the N_{wet} a good option, to consolidate all the water vapour content contributions into a variable.

Adding again the N_{wet} to the model it is visible a improvement on the R-squared, in Figure 6.9.

```
Linear regression model:
    Stdv ~ 1 + Pressure + Temperature + Nwet

Estimated Coefficients:
                      Estimate        SE         tStat      pValue
                    ____________    ___________    _______    ___________

    (Intercept)        1.6691        0.066029      25.279    5.8729e-136
    Pressure        -0.0015942     6.457e-05      -24.69    5.2964e-130
    Temperature      0.0026237     0.00011082     23.674    5.1756e-120
    Nwet            0.00053271     2.6332e-05      20.23     6.7126e-89


Number of observations: 8423, Error degrees of freedom: 8419
Root Mean Squared Error: 0.0426
R-squared: 0.231,  Adjusted R-Squared 0.231
F-statistic vs. constant model: 843, p-value = 0
```

Figure 6.9: Linear regression results adding the N_{wet}

Ortgies-T and Ortgies-N, two well known models described in section 4.3, link the scintillation standard deviation with the surface temperature and the N_{wet}. In the same note, the

following linear regression, in Figure 6.10, studies the Temperature and the N_{wet} relation with the scintillation standard deviation.

```
Linear regression model:
    Stdv ~ 1 + Temperature + Nwet

Estimated Coefficients:
                    Estimate        SE        tStat       pValue
                   __________    __________    ______    __________

    (Intercept)      0.039402      0.001756    22.438     2.394e-108
    Temperature      0.0027794    0.00011457    24.259    1.0265e-125
    Nwet            0.00058224    2.7188e-05    21.415     4.0864e-99


Number of observations: 8423, Error degrees of freedom: 8420
Root Mean Squared Error: 0.0441
R-squared: 0.175,  Adjusted R-Squared 0.175
F-statistic vs. constant model: 895, p-value = 0
```

Figure 6.10: Linear regression results.

The main conclusion taken from the histograms and the regressions is that the scintillation standard deviation is, indeed, correlated to the meteorological parameters. However, to model it other parameters are necessary besides the meteorological ones measured only at ground level. The use of meteorological profiles such the ones of ERA-5 would be interesting.

6.3 Scintillation distributions

6.3.1 Distribution of the standard deviation

Following the section 4.2.2, this section presents the long-term scintillation standard deviation probability density results. As discussed before, several standard probability distributions have been suggested. The first goal is to compare our data with the most known PDFs, such as: Normal, Log-normal, Gamma and Rice-Nakagami. The theoretical probability density functions are plotted together with the experimental ones for one year and for the two beacons, in Figure 6.11.

Observing the two figures, it can be concluded that for the Q-band, a log-normal distribution is the best fit to the Aveiro data. However, for the Ka-band, the Gamma and the log-normal distributions seems to perform better (almost with similar performance) but not enough to fit the data.

Table 6.3 shows the distributions parameters for all the distributions plotted in Figure 6.11.

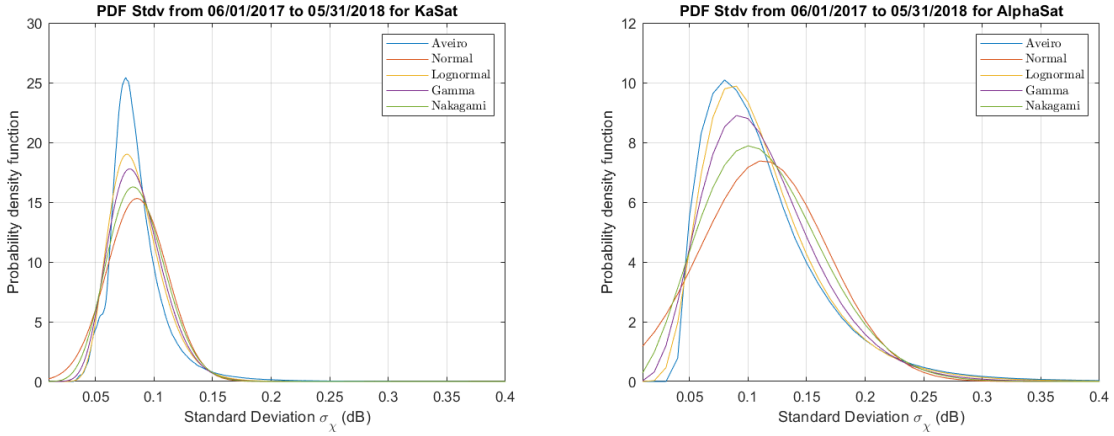

(a) Probability density function: Ka-band.

(b) Probability density function: Q-band.

Figure 6.11: Models distributions comparison with Aveiro distribution.

Table 6.3: Distributions parameters

	AlphaSat	Ka-Sat
Normal distribution	$\mu = 0.118$	$\mu = 0.094$
	$\sigma = 0.056$	$\sigma = 0.027$
Lognormal distribution	μ = -2.226	μ = -2.398
	σ = 0.427	σ = 0.253
Gamma distribution	a = 5.402	a = 14.788
	b = 0.022	b = 0.006
Nakagami distribution	$\mu = 1.405$	$\mu = 3.493$
	$\Omega = 0.017$	$\Omega = 0.009$

6.3.2 Distribution of the scintillation amplitude

The aforementioned scintillation prediction models overpredict the long-term average scintillation standard deviation. These models seem not to be adequate to describe the scintillation at the site. The scintillation prediction model by van de Kamp [35] uses the water content of heavy clouds W_{hc}, therefore, this model will be tuned to match our data, as this correlation has been, at least, visually observed at IT-Av site.

Comparison with reference distribution models

The cumulative distribution have been derived for a full year. These distributions were converted to the complementary cumulative distribution function, CCDF. The following plots represent the ITU [45], Karasawa, Otung and the Van de Kamp models. All these models were described in section 4.3. The only model that includes another meteorological variable besides the N_{wet} is the Van de Kamp one that requires also the liquid water content of clouds W_{hc}. In this simulation, the water content of heavy clouds, was considered $W_{hc} = 0.94$ (kg/m^2) and was obtained roughly from the maps in [38]. The input parameters are displayed in Table 6.4:

Table 6.4: Parameters used for plotting the models - Ka-band.

Parameters	G(x)	h (m)	θ (°)	D (m)	N_{wet} (ppm)	σ_{ref} (dB)	σ_{pre} (dB)
ITU	0.8615	2000	39.63	1.5	51.4	0.0087	0.0792
Karasawa	0.9088	2000	39.63	1.5	51.4	0.0095	0.0528
Otung	0.8615	2000	39.63	1.5	51.4	0.0089	0.0709
Van de Kamp	0.8615	2000	39.63	1.5	51.4	0.0064	0.0405

Since the ITU model [45] does not present an equation to predict the enhancements this prediction is not included in the figures.

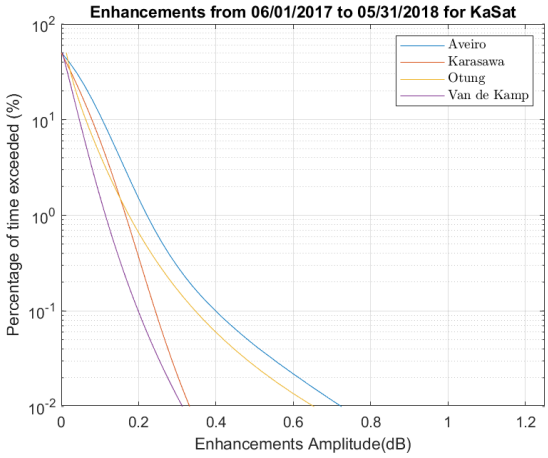

(a) CCDF for the enhancements: Ka-band.

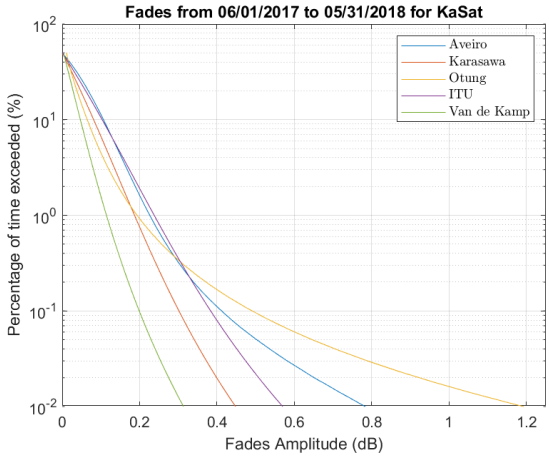

(b) CCDF for the fades: Ka-band.

Figure 6.12: Complementary cumulative density function comparison between models and Aveiro data - Ka-band.

Figure 6.12 set out an acceptable prediction using the Otung model: from all the models tested, it is the one that gets closer to our data. The van de Kamp and the Karasawa models underpredict in the two situations. The ITU model has an acceptable prediction for the fades, even though it still underpredicts the values.

The same mentioned procedure was done for the Q-band, with the following parameters from Table 6.5:

Table 6.5: Parameters used for plotting the models - Q-band.

Parameters	G(x)	h (m)	θ (°)	D (m)	N_{wet} (ppm)	σ_{ref} (dB)	σ_{pre} (dB)
ITU	0.9423	2000	31.8	0.62	51.4	0.0087	0.1556
Karasawa	0.9515	2000	31.8	0.62	51.4	0.0095	0.1112
Otung	0.9423	2000	31.8	0.62	51.4	0.0089	0.1321
Van de Kamp	0.8423	2000	39.63	1.5	51.4	0.0064	0.0739

The results are plotted in Figure 6.13 and are similar to the Ka-band, being that the model that best describes our data, is still the Otung one. The other ones, underpredict the distribution with the exception for the ITU model. The latter, gives an overprediction till a certain percentage and then an underprediction for lower percentages.

A convenient method to study scintillation variability through the year is to observe the monthly CCDFs. Based on the statistics contained in section 4.2 the corresponding PDFs must be calculated first in order to derive the CCDF. For each month, the data is loaded to compute the final histogram matrix. Later, the resulting matrix goes through a cumulative sum, followed by a normalization, to get the cumulative probability distribution. Again, the scintillation amplitude was divided in two ranges: the fades (positive values) and the enhancements (negative values).

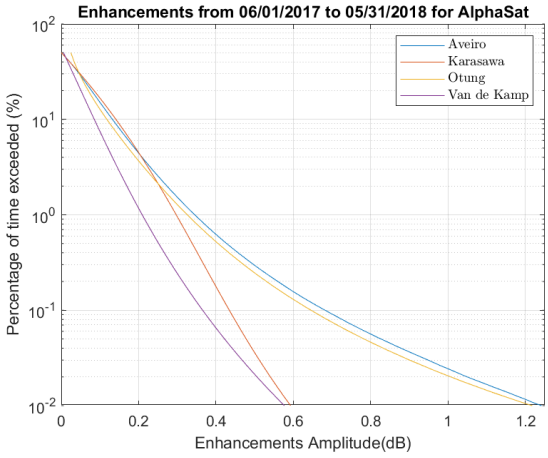

(a) CCDF for the enhancements: Q-band.

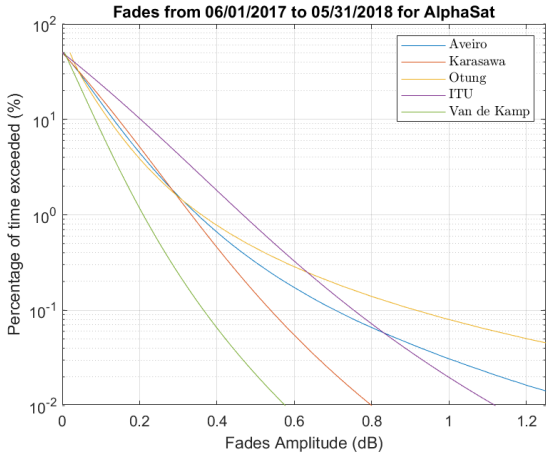

(b) CCDF for the fades: Q-band.

Figure 6.13: Complementary cumulative density function comparison between models and Aveiro data - Q-band.

The first conclusion taken, from Figure 6.14 and Figure 6.15, is that the fades are deeper in relation to the enhancements for the same period of time. For both cases, the month with higher levels of scintillation amplitude is June. This month, can be a warm and humid month which contributes for a higher refractivity value producing eventually large scintillation amplitudes.

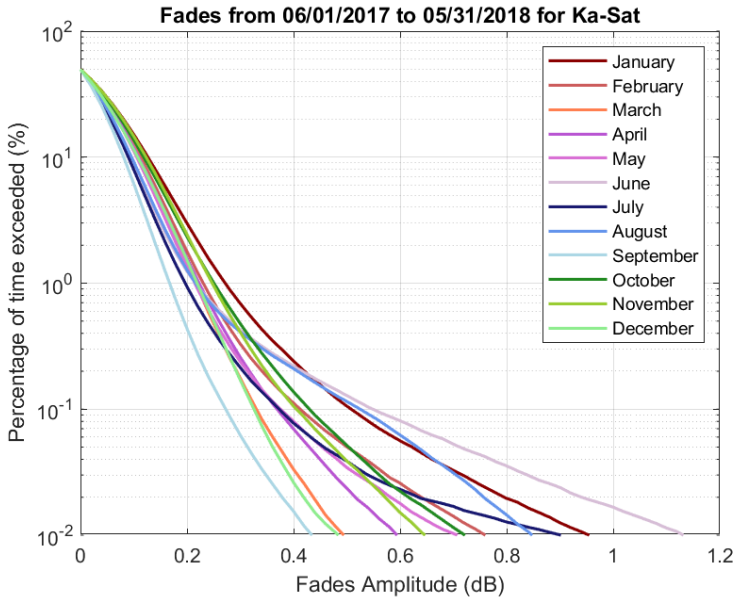

Figure 6.14: Complementary cumulative density function for the fades: Ka-band.

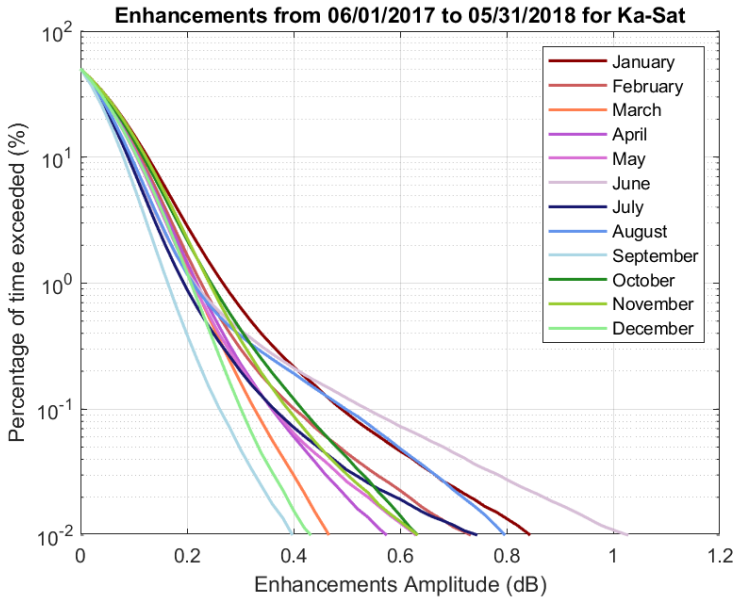

Figure 6.15: Complementary cumulative density function for the enhancements: Ka-band.

Figure 6.16 is in agreement with the previous conclusions. It shows that in comparison with the other months, June is the one that has the higher scintillation intensity values for the majority of time. Given these points, it is expected that this month, should be the one with the higher N_{wet} value. To prove it for each month was found it average value.

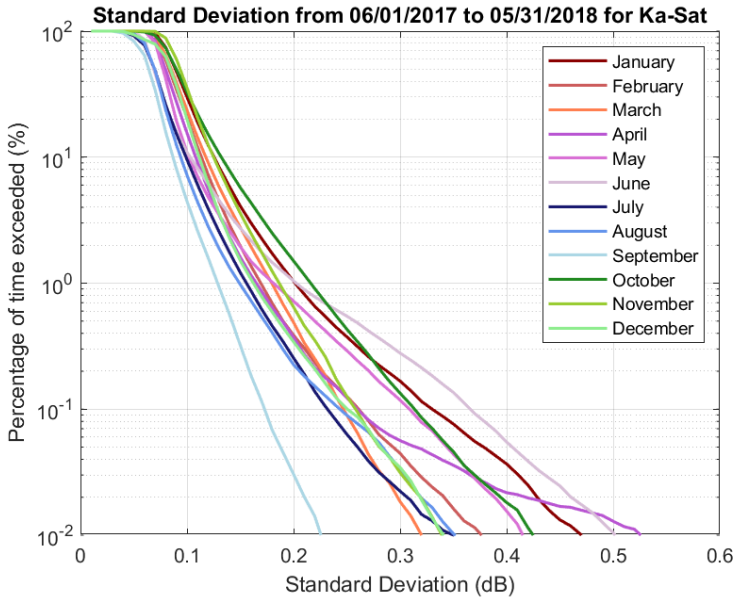

Figure 6.16: Complementary cumulative density function for the standard deviation.

Table 6.6 exhibits the results along with the average temperature and average relative humidity. June has, indeed, the highest average N_{wet}: 73.25 ppm.

However, observing again Table 6.6, the month with the lowest N_{wet} value is February, which is not in agreement with Figure 6.16 where is clear that September is the month with the lowest scintillation intensity. Unfortunately, from this, can be concluded that scintillation is not only related with the refractivity value.

Table 6.6: Monthly averages of temperature, relative humidity and N_{wet}.

Month	Average temperature ($°C$)	Average RH (%)	Average N_{wet} (ppm)
January	10.47	70.64	41.52
February	10.02	57.76	33.24
March	11.47	65.87	41.24
April	13.43	71.88	49.48
May	15.30	71.16	54.79
June	19.03	76.89	73.25
July	18.73	73.37	68.08
August	18.61	73.07	67.22
September	16.52	76.10	62.80
October	17.55	59.82	49.07
November	12.96	61.07	41.33
December	10.81	64.29	39.20

6.4 Scintillation diurnal variation

After studying the phenomenon in a long-term period, the main point of this section is to analyze the hourly dependence. A routine was produced to calculate the mean value of σ_χ for the same hour of the day in a monthly basis. For example, for the month of July, the values correspond to a matrix of 31x24 values, where each row corresponds to a day of the month and each column corresponds to an hour of the day. The following figure, plots the hourly standard deviation mean value, in UTC (data is collected in an UTC time reference for easy exchange with other experimenters).

It is noticeable a pattern between the two frequency bands, for both months of Figure 6.17. Around midnight is the period presenting a scintillation somewhat more intense, as well as, in the afternoon. Observing all the months in discussion, not displayed in this dissertation for reasons of brevity, the common ground between them is the afternoon period with a peak around 2:30 pm. It starts around 10 am and finishes close to 8 pm. An interesting detail is that for the warmer months the starting point skews a little for the left, beginning the scintillation earlier.

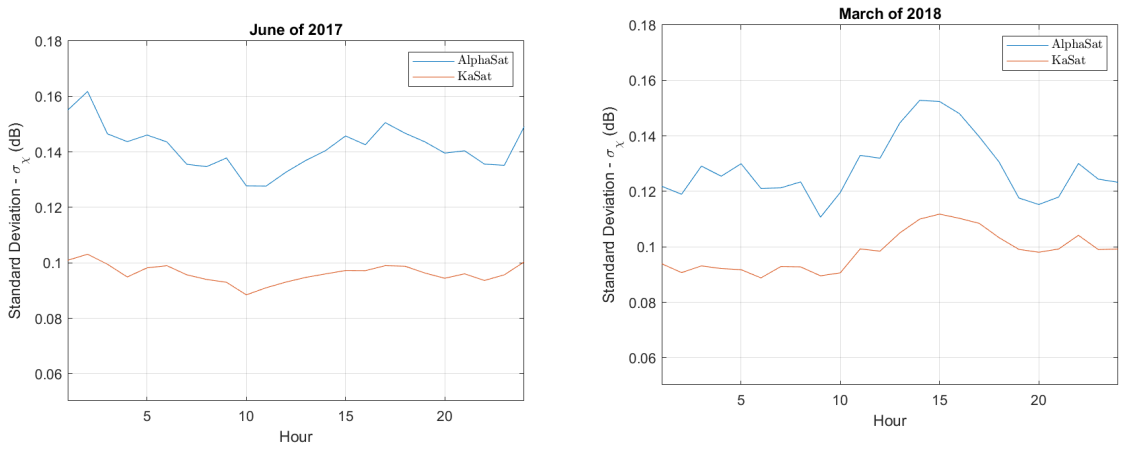

(a) Diurnal variation for the month of June of 2017. **(b)** Diurnal variation for the month of March of 2018.

Figure 6.17: Scintillation standard deviation diurnal variation.

To complement the above observation, the σ_χ mean value for each hour is plotted in the following picture, for the all the months.

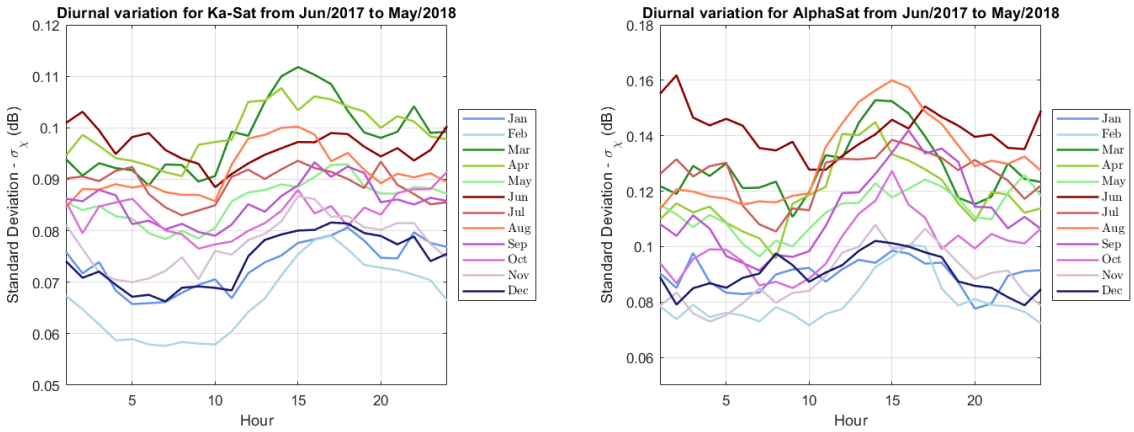

(a) Diurnal variation for the Ka-band. **(b)** Diurnal variation for the Q-band.

Figure 6.18: Annual diurnal variation of the scintillation standard deviation.

The standard deviation trend is more pronounced observing all months together, as can be seen in Figures 6.18a and 6.18b. The standard deviation has also a nocturnal period with increased intensity with a peak around 3 pm.

6.5 Autocovariance analysis

The autocovariance measures the signal similarity with a delayed version of itself. This section reports a test and preliminary results on the application of the autocovariance to the scintillation standard deviation time series. The main goal is to observe the correlation of a month with itself and the remaining months of the year. With that in mind the standard deviation time series for each day, from June 2016 to May 2019, were read and concatenated into an array. However, the length for the original scintillation standard deviation time series is 86400 samples per day so, the final array with the 3 years of data would amount up to 94176000 values. The manipulation of this volume of data would not be efficient, so the solution was to decimate the signal and to just use one sample per minute. The autocovariance can be computed using the MATLAB function called *xcov*.

For each month, the previous 2 month and following 2 months are selected from a 3 year data array. In Figure 6.19, as an example, the month of August is selected along with more 4 months (2 months before plus 2 moths after the one under analysis).

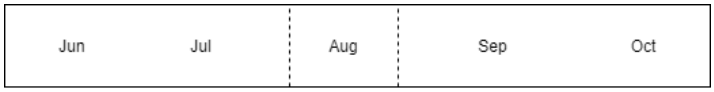

Figure 6.19: Representation of the input array.

The *xcov* returns the autocovariance of the time series x. It delays x by (2N - 1)/2 samples, where N is equal to the length of the longer input sequence (5 months in samples). This delay is also know as lag. The autocovariance $c(m)$ is function of the lag imposed on the comparison signal, where $m = 1, ..., 2N - 1$. Because the lag value is 4.5 months, the lag(0) point was considered to be the middle of the input array. In the example the middle point corresponds

to: "16-Aug-2017 12:00pm".

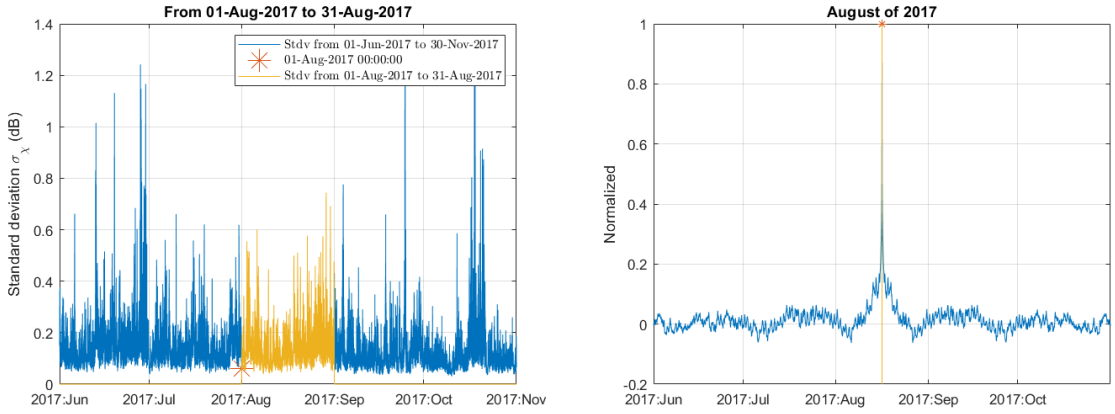

(a) Input array for the analysis of August 2017. **(b)** Output sequence from xcov.

Figure 6.20: Autocovariance for January 2018.

Figure 6.20a shows the input array with August highlighted and figure 6.20b the output autocovariance sequence.

Autocovariance is widely used in pattern recognition. In the scintillation analysis the autocovariance can help to recognize monthly dependence or even diurnal variations.

Figure 6.20b shows precisely a symmetry pattern, having as reference the lag(0). This point has the maximum value of covariance, leading to a obvious conclusion: when the series is not delayed it is fully correlated with itself. However, adding delay changes the scenery. Quickly the correlation decreases.

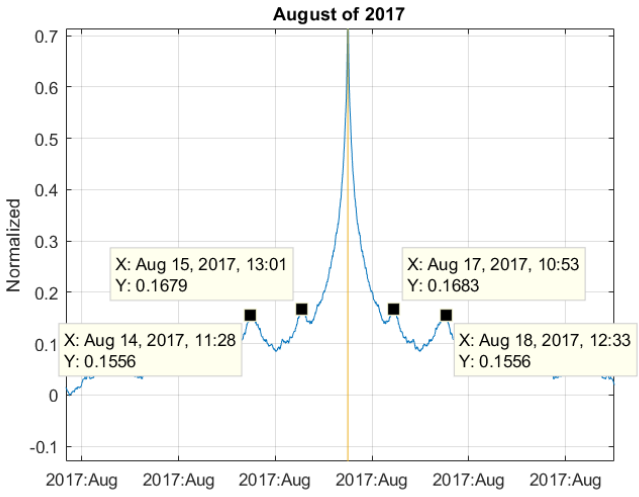

Figure 6.21: Figure 6.20b zoomed in.

Observing closely the Figure 6.20b, Figure 6.21 shows an important correlation between the noon of the different days. Recalling Figure 6.18b, this time of the day is when scintillation

begins to occur during the day.

This process was applied to every month. To abbreviate this analysis another month in a different season was selected. In this case, November, is a low scintillation month (see Figure 6.18b) and less stationary than August (see Figure 6.22a and Figure 6.20a)

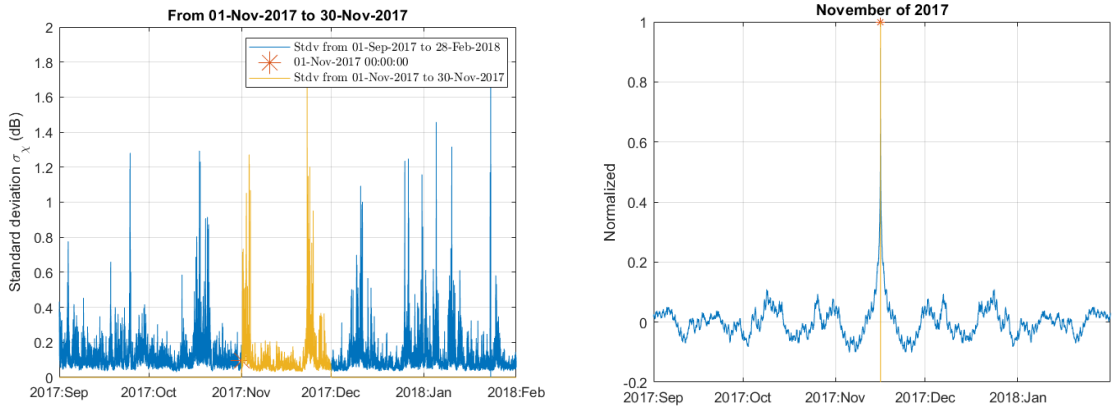

(a) Input array for the analysis of November 2017.

(b) Output sequence from xcov.

Figure 6.22: Autocovariance for November 2017.

Figure 6.22b displays a much more "wavy" curve in comparison with 6.20b. This is explained by all the abrupt decays and rises typical of the scintillation standard deviation values captured in November.

6.6 Scaling of scintillation intensity

The numerical relation between the scintillation variance at the two frequencies is established by the ITU-R and Karasawa prediction models.

The relationship between the variance at frequency f_1, and frequency f_2 is given by the following equation.

$$\frac{\sigma_1^2}{\sigma_2^2} = \left(\frac{f_1}{f_2}\right)^a \left(\frac{\sin\theta_2}{\sin\theta_1}\right)^b \frac{G(x_1)}{G(x_2)} \tag{6.4}$$

where $G(x_n)$ is the smoothing gain factor from the ITU recommendation, calculated with equation (3.39). However, this value is dependent on the height of the turbulence. It is necessary to assume a value for this parameter to calculate the antenna averaging factor. For this calculation the height was considered to be 1000 m.

Assuming the turbulence height equal for the two links, the final value for the smoothing factor is displayed in Figure 3.14a. For the AlphaSat the smoothing factor is 0.94 and for the Ka-Sat 0.86.

Replacing the respective values in equation (6.4), the final scaling is 0.286. The variance time series for the Ka-Sat is displayed in a scatter plot in function of the variance for the AlphaSat.

The scatter plot of σ_1^2 and σ_2^2, for one particular month, is depicted in Figure 6.23.

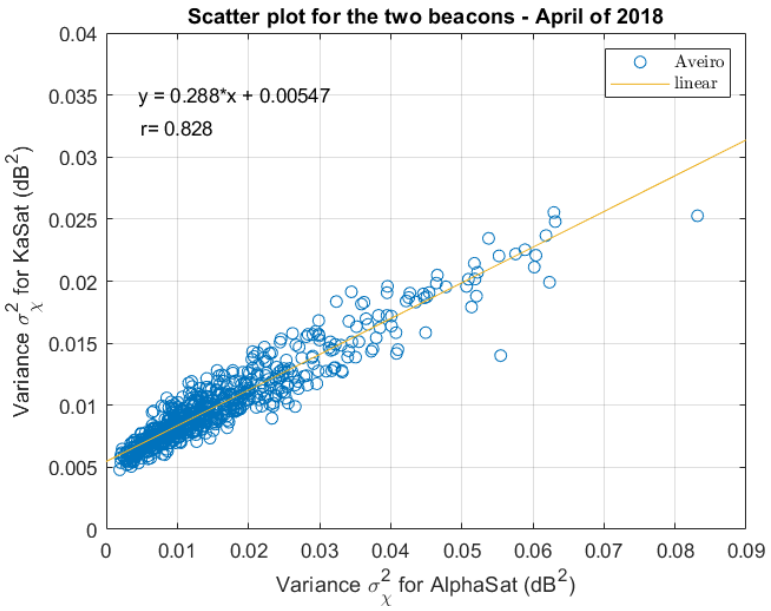

Figure 6.23: Ka-band variance versus Q-band variance.

It is possible to compute the linear relation between the two variances.

$$y = 0.288x + 0.00547 \tag{6.5}$$

The equation shows a slope of 0.288 that represents the scaling ratio between the two frequencies. The theoretical predictions, i.e. equation (6.4), match very well the experimental data in what concerns the variance scaling.

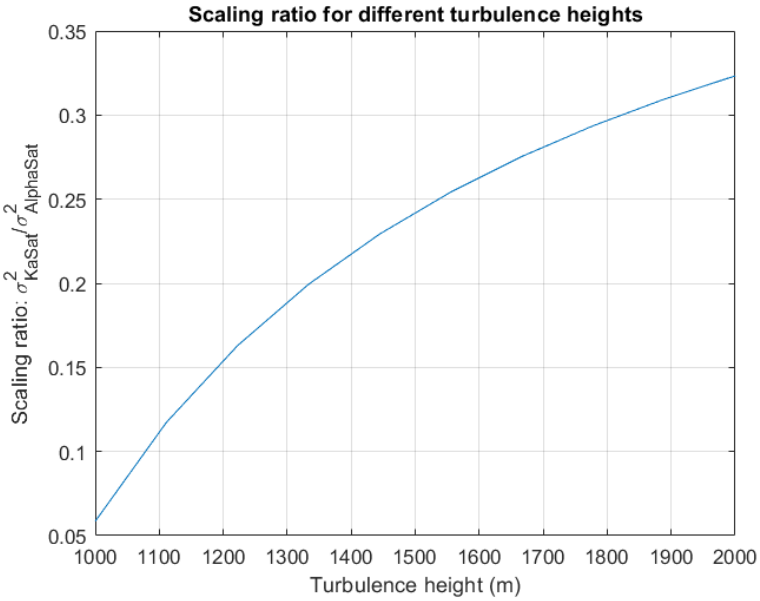

Figure 6.24: Scaling ratio in function of the turbulence height.

The observed ratio is displayed in Figure 6.24. Accordingly to the figure the higher the turbulence the higher the scaling ratio.

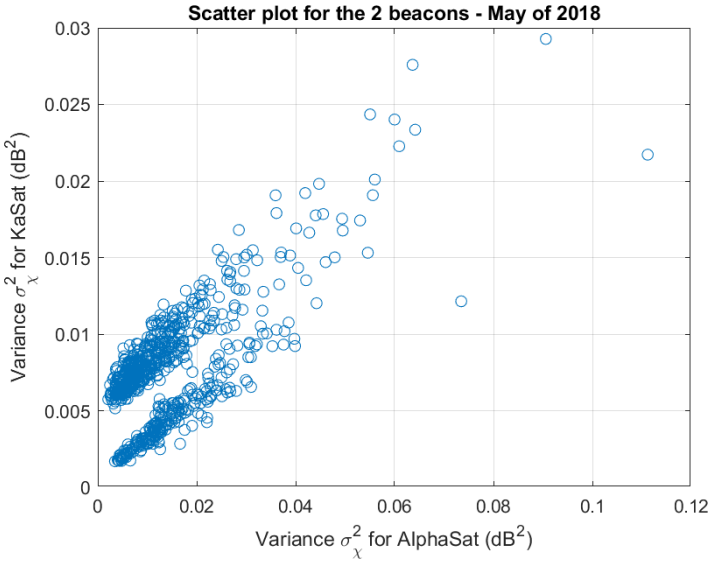

Figure 6.25: Ka-Band variance versus Q-band variance: May 2018.

The month depicted in Figure 6.25 has a peculiarity that distinguishes it from the other months: the scatter plot is sliced in the middle. The Ka-band receiver has been upgraded in the last 10 days of this month, and the CNR was improved. This created two visible data sets corresponding to two distinct values CNR.

Finally, the annual scatter plot of the two frequencies is displayed bellow in Figure 6.26.

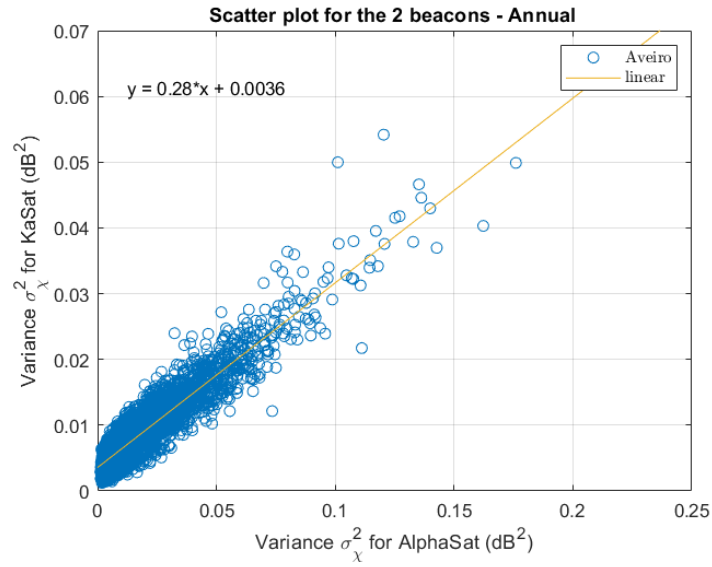

Figure 6.26: Ka-band variance versus Q-band variance: one full year.

6.7 Spectral analysis

A spectral analysis for the dry scintillation data available, between June of 2017 and May of 2018 was carried out. The Q-band scintillation periods with a standard deviation 4 times higher the standard deviation induced by the thermal noise ($\sigma_{threshold} = 0.0387 \times 4 = 0.1548$ dB) were selected and, from these ones, only those lasting 15 minutes or more were selected for spectral analysis. Shorter periods were discarded.

The tool used to calculate the spectrum is a built-in MATLAB function named *pwelch*. In order to used it, the 15 minutes blocks of standard deviation are split, by the function, into 2.5 minutes blocks and an Hamming window is used.

As discussed in section 3.6, the theoretical scintillation spectrum is characterized by having two distinct parts: a flat part followed by a decay zone. Frequency ranges were defined to access the two spectrum ranges (vertical green line in Figure 6.27).

The flat section was considered from 0.05 Hz to 0.4 Hz and the decay area from 0.4 Hz up to 1 Hz. One of the interesting values that can be extracted from the spectrum is the corner frequency, which is the frequency where the two spectrum sections intersect (circle marker in Figure 6.27). The first line (red) is the mean value of that spectrum section. The second line is the result of a polynomial curve fitting.

The fitting results into a first degree equation (n=1):

$$p(x) = p_1 x^n + p_2 x^{n-1} + ... + p_n x + p_{n+1} \tag{6.6}$$

where p_1 gives the spectrum slope.

The corner frequency is achieved by doing the intersection between equation (6.6) and the flat line.

The wind velocity was averaged for one hour around the selected scintillation periods.

A total of 384 spectra were obtained: all were scrutinized visually, remaining 227 spectra for further analysis.

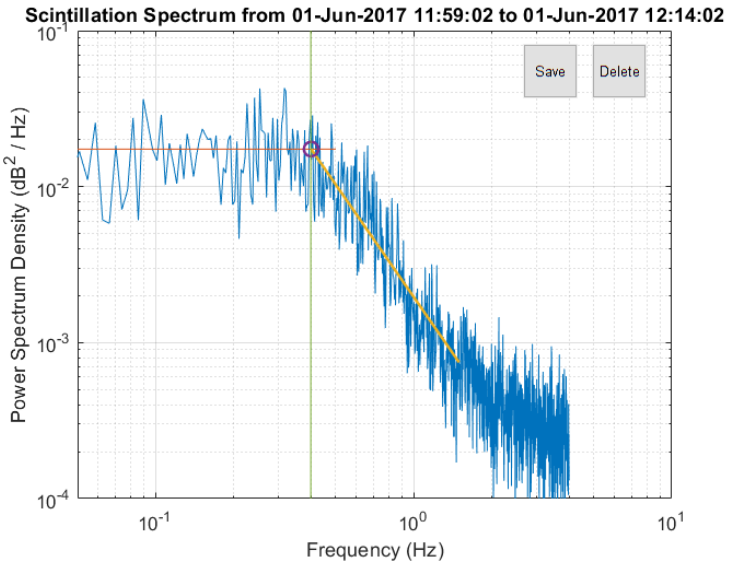

Figure 6.27: Spectrum validation.

The visual inspection consisted of deleting the spectra with absolute roll-off factors smaller than 1, plus spectra with unusual shapes, principally in the flat part that are caused by weak periods of scintillation or eventually not well developed turbulence periods. This was done interactively with the aid of two added buttons to the figure (see Figure 6.27).

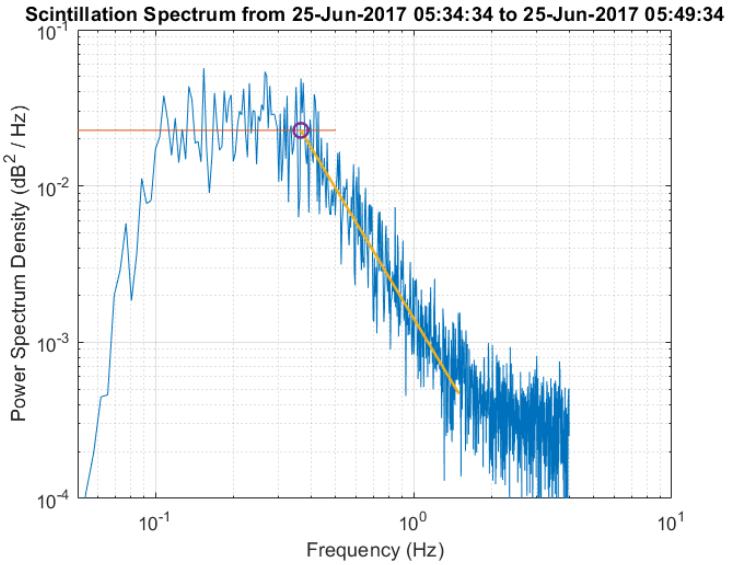

Figure 6.28: Q-band scintillation spectrum.

An example of a selected spectrum is plotted in Figure 6.28, where it is clear the flat part for the lower frequencies, followed by a roll-off factor, as described theoretically in equation (3.36).

For this case, in particular, the corner frequency has a value of 0.3006 Hz and the spectrum rolls of with a slope of -2.4097. The Kolmogorov model gives rise to a slope of $-11/3$ for the turbulence spectrum that is related to the power spectral density scintillation slope measured above. For the scintillation spectrum the usual theoretical value is -2.6667, that is close to the experimental value here displayed.

For the Ka-band the standard deviation periods were selected concurrently with the ones of the Q-band. It is expected that if scintillation is occurring at one frequency it is occurring at the other, too. Figure 6.29 confirms the previous statement. The scintillation power is, however, lower for the Ka-Sat because the scintillation amplitude is also lower.

For this spectrum, the roll factor is -1.883 and the corner frequency is 0.3291 Hz. The following Figure 6.30 shows precisely that the scintillation amplitude is higher in the Q-band. Focusing on the all amplitude excursion, the Q-band reaches a pk-to-pk amplitude of 0.7 dB, thus the Ka-band only reaches 0.5 dB.

For the same periods, the probability density function (6.31) shows that the scintillation captured expresses for the Ka-band has smaller absolute roll-off factors. In fact, it is unlikely to have absolute roll off factors higher than 2.666 as expected from theory.

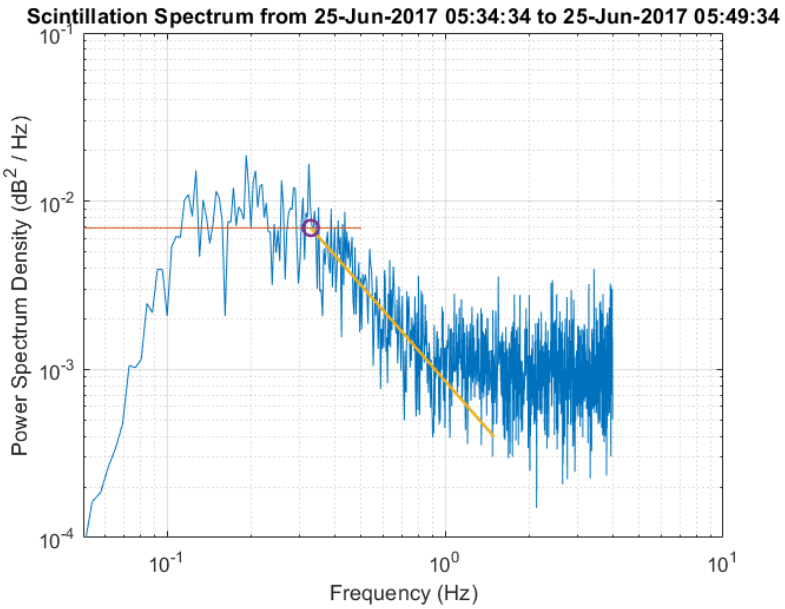

Figure 6.29: Ka-band scintillation spectrum.

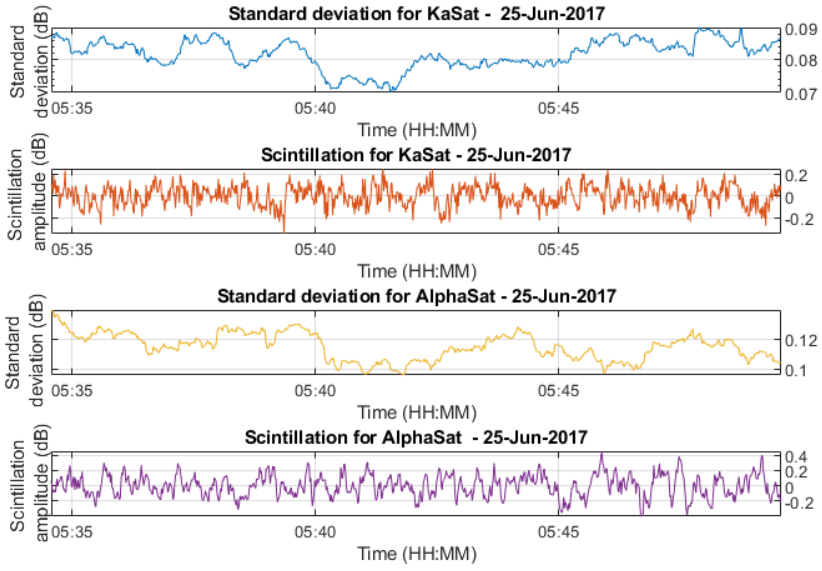

Figure 6.30: Scintillation and standard deviation for one period in analysis.

Taking these results into account, an attempt was made to find better periods for the spectral observation, with the Ka-Sat data. The spectrum search was done the same way as mentioned previously, however in this case shorter periods were selected where the standard deviation had to be above 0.110 dB.

The yellow line in Figure 6.31 is the result from this improvement.

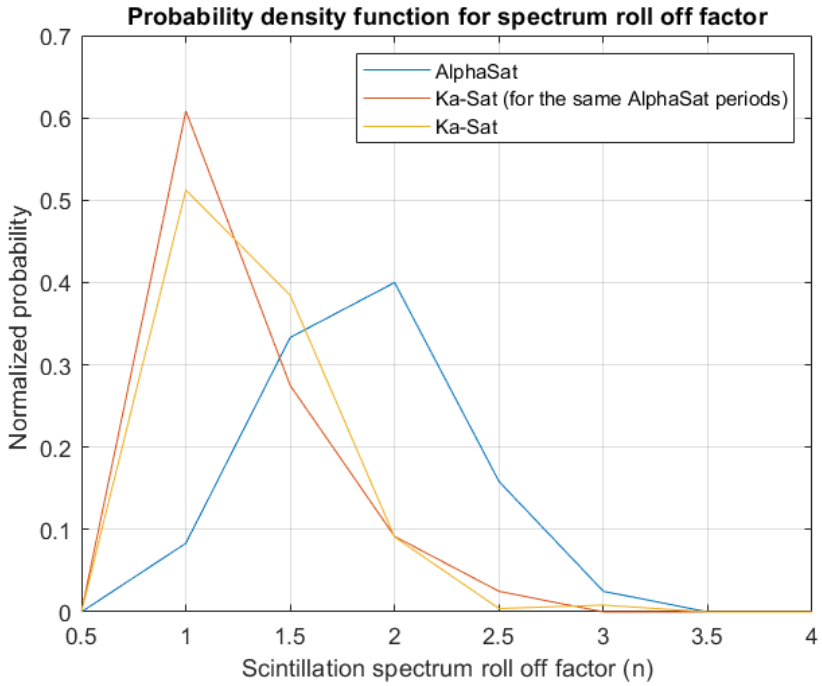

Figure 6.31: Probability density function for the spectrum slopes database: 1-Jun-2017 to 31-May-2018.

In this last analysis there is a slight change in the Ka-band statistics. However, the probability of having an absolute roll-off factor of 2.666 continues to be sparse. To reach higher roll-off factors, the scintillation period that is being analyzed needs to be sufficiently stationary and strong in intensity. What is happening here is that for the Ka-Sat probably these requirements are not being met. In fact, the scintillation intensity is smaller at Ka-band and the noise spectral density is higher, thus, a few (precious) dBs of dynamic range are missing in the spectrum.

6.7.1 Corner frequency dependence on wind velocity

Equation (3.38) presents the relation between the corner frequency of the scintillation spectrum and the wind velocity. Through this equation it is possible to estimate the corner frequency knowing the transverse component of the wind velocity.

As mentioned before, the meteorological station located at IT-Av, measures the wind speed at ground level (Figure 5.3) but the ideal values would be the ones measured at the turbulence height. A solution encountered was selecting not only the speed values for the 15 minutes time window but those in one hour window expecting that these two velocities could be correlated.

The total wind velocity v can be split into two components: the transverse velocity v_t, which is perpendicular to the Earth-space path and the v_a which is parallel to the Earth-space path (see Figure 6.32 and Figure 6.33).

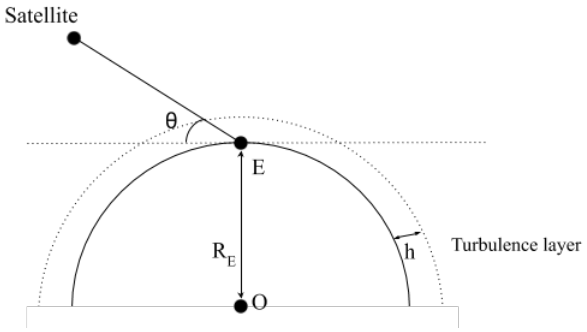

Figure 6.32: Geometrical representation of the Earth, Earth-Station (E) and the communication link to the satellite (S).

Figure 6.33 shows α, the angle between the total wind velocity and the transverse velocity, therefore,

$$v_t = \|v\| \cos \alpha \tag{6.7}$$

where θ is represented in Figure 6.32 and α is:

$$\alpha = 90^\circ - \theta \tag{6.8}$$

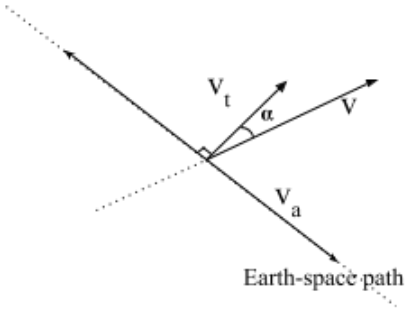

Figure 6.33: Geometrical representation of wind speed components.

For the elevation angles of Ka-Sat and AlphaSat links, the values for this angle are respectively: $\alpha = 51^\circ$ and $\alpha = 58^\circ$. The resulting values of the wind velocity extracted simultaneously with the spectra were multiplied by the cosine of the respective α.

The transverse wind velocity is computed and plotted in scatter plots in function of the corner frequency (see Figures 6.34 and 6.35).

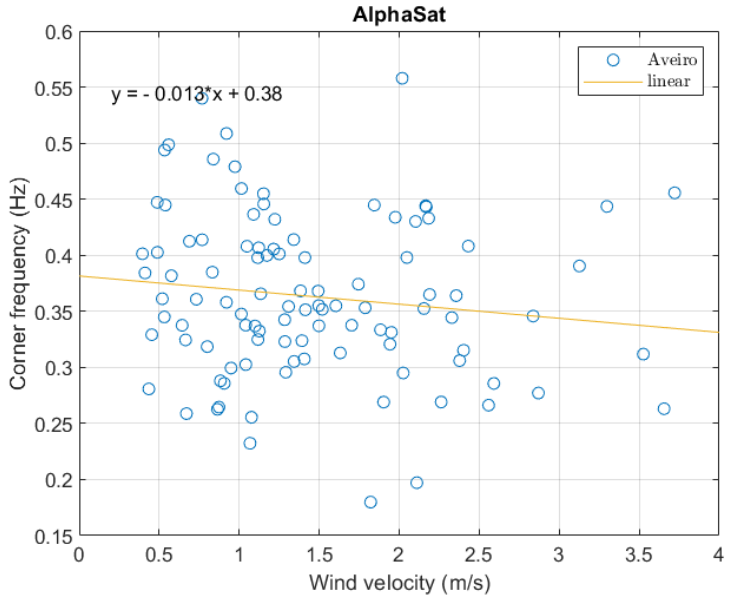

Figure 6.34: Corner frequency versus the wind velocity for the Q-band.

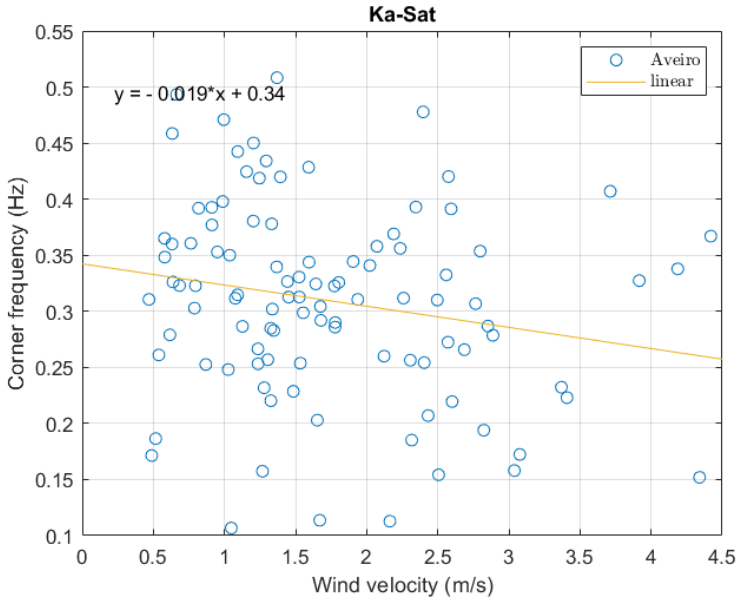

Figure 6.35: Corner frequency versus the wind velocity for the Ka-band.

As we can see there is almost no evident relationship between the two parameters, as the correlation coefficients are -0.14 for the AlphaSat and -0.18 for the Ka-Sat: it seems that the wind velocity measured at the ground level can not be used to predict the corner frequency.

The resulting corner frequencies of the spectrum for the two beacons are displayed in a scatter (Figure 6.36) plot where it is visible a linear relation. The line slope is 0.59 representing the ratio between the corner frequencies.

Since the wind transverse velocity is proportional to the corner frequency (see equation 3.38) and also considered to be equal for the both links, the relation between the corner frequencies can be found:

$$f_{c_{Qband}} = f_{c_{Kaband}} \sqrt{\frac{\lambda_{Kaband} L_{Kaband}}{\lambda_{Qband} L_{Qband}}} \tag{6.9}$$

Considering a turbulence height of 1000 m the respective L values are available on Table 3.2.

As a conclusion: from Figure 6.36 our experimental ratio is 0.59. Through the theoretical equation (6.9) the ratio is 0.77, such discrepancy can be a result of all approximations due to not having available the direct measurements of the wind velocity at the turbulence layer.

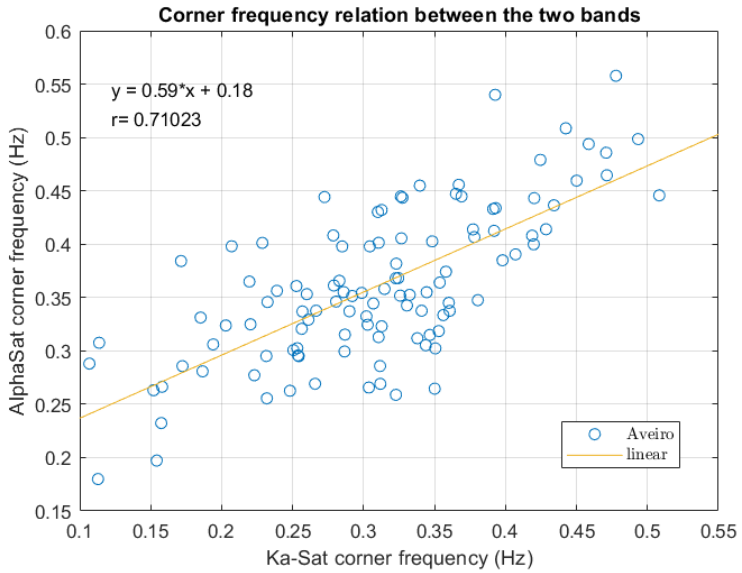

Figure 6.36: Scatter plot of the corner frequencies at Q-band and Ka-band.

6.7.2 Corner frequency dependence on spectrum slope

In Figure 6.37 seems that the roll-off factor is systematically lower at Ka-band. The results must be seen with some precaution because, in this band, the scintillation intensity is lower than the one at Q-band and the spectrum sinks into the noise floor at a lower frequency than the one at Q-band. Thus, the higher frequency range in the decay zone can be overestimated leading to a underprediction of the roll-off factor n.

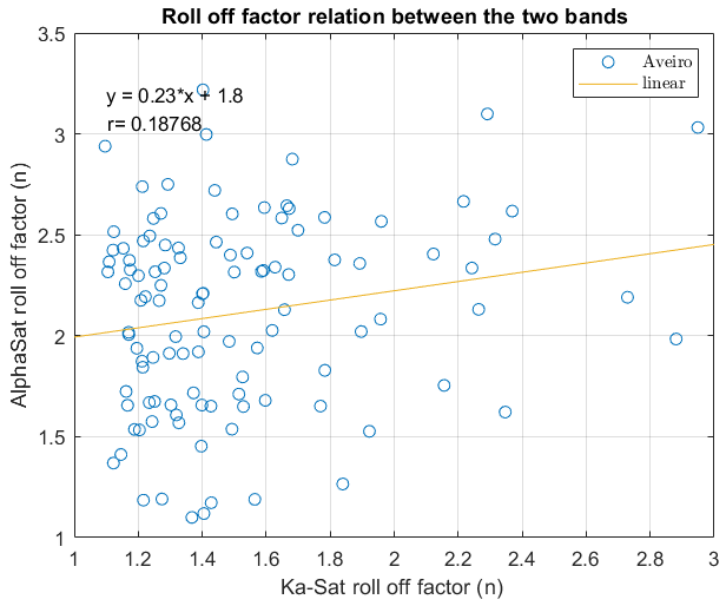

Figure 6.37: Roll off factor relation between the two links.

Maybe it is advisable to review the frequency ranges, or even decide the better values on an event basis, or being more conservative keeping only the more intense events (shorter database). This was not made due to lack of time for another iteration on this subject.

Figures 6.38, 6.39 show that there is not a strong dependence between these two parameters: in fact there is no theoretical support for such dependence.

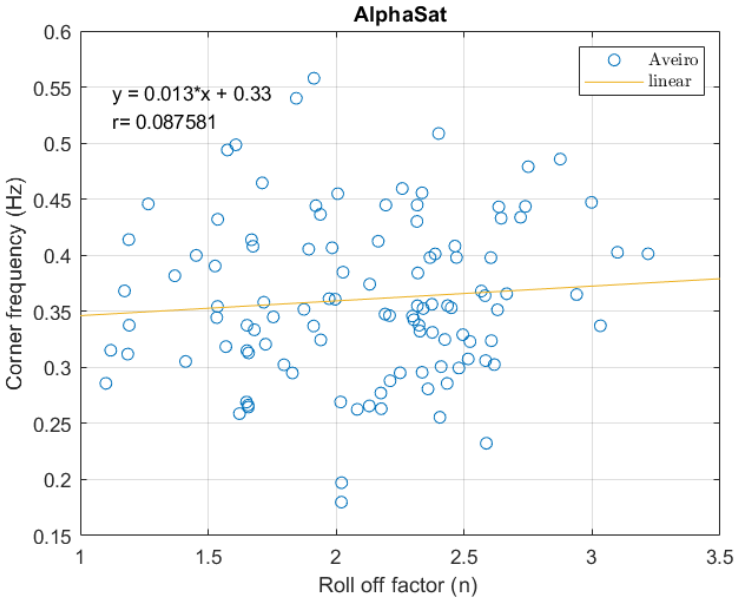

Figure 6.38: Q-band corner frequency as a function of the roll of factor.

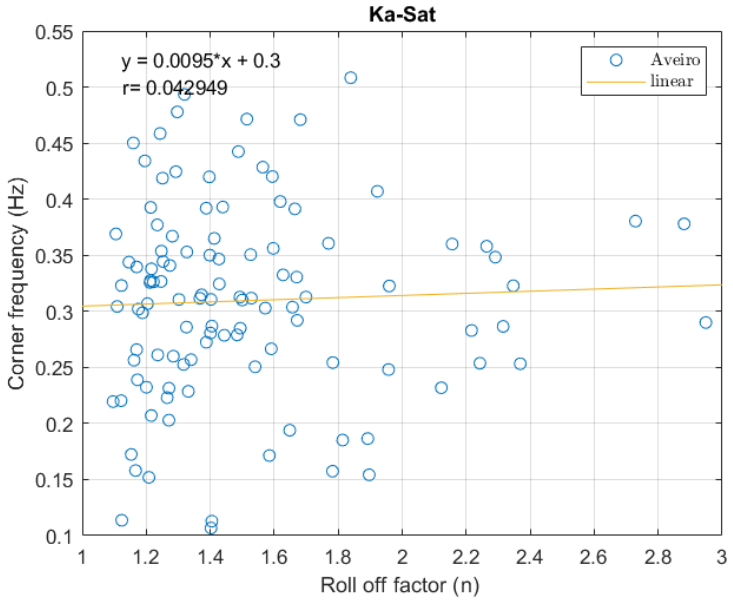

Figure 6.39: Ka-band corner frequencies as a function of the roll of factor.

The roll off factor has to do with the structure of the turbulence and the corner frequency with the wind speed: unless some physical basis supports a relation between these quantities, the observed poor correlation is acceptable.

Chapter 7

Final conclusions and future work

7.1 Conclusions

A set of data with a very significant duration - two years - was analyzed. The volume of data mounts to 19.4 GB: includes meteorological data and signal amplitude of two beacons, one in the Ka-band and another in the Q-band. The manipulation of these data required the development of relatively complex tools given not only the temporal extension of the data but also a multivariate analysis on diverse parameters. The data in the Q-band are original, very significant in the context of the international database in this framework and will contribute to enrich the ITU database.

In addition, an individual beacon analysis and a joint analysis of the two beacons were performed. The unique feature of this analysis is that, unlike others that use beacons installed in the same satellite, and therefore, the signal is conditioned by the same volume of atmosphere, in this case, the links converge at the receiving point and have an angular separation of 17^{o}. Consequently, essentially different volumes will condition the signal received at each earth station. Also, an almost unique future between experimenters is that meteorological parameters are measured at the site and not tens of km away, therefore, the data quality is controlled by the experimenter. An already significant correlation (and with very similar values) was found on an hourly basis between scintillation intensity and temperature, absolute humidity and pressure, raising questions about the modelling of the reference scintillation intensity.

The analysis of the monthly and diurnal variation of the scintillation intensity was made. Usually, summer months or autumn/spring moths (often with clouds) are the most scintillating days: a fact often observed. The daily variation shows a more intense scintillation intensity during periods of daylight, starting at the end of the morning and extending into the afternoon: a more evident effect in the warmer months. A not-so-common fact is a resurgence, although moderate, of scintillation within the first 3 hours of the day. It seems the atmosphere has evolved to a new state in the stability conditions, after the afternoon and before the end of the morning.

The amplitude distributions and the variance models, found in the literature, seem not to be adequate at high percentages. Probably, this phenomenon has a more climatic complexity that the attenuation has, for example. In addition, no significant differences in the distribution of fades and enhancements were found.

The frequency scaling factor conforms very well with the ITU models, even if the concurrent

data is collected in slightly distinct link paths. With respect to the spectral properties of the scintillation, a few conclusions can be drawn. The slope factor is very variable, looking like the Kolmogorov spectrum does not always suit the propagation scenario. The relationship between the corner frequency and the wind speed measured at ground level is disappointing. However, the correlation of the corner frequencies is quite good, thus, the wind at both links must be very similar in the concurrent point of view.

7.2 Future work

The database was largely explored, but, a few things can still be done. The use of the ERA database is recommended to analyze possible better correlations with height integrated quantities such as water vapour or dependencies of the corner frequency with the wind. Also, the analysis of the wind speed vector could be interesting to explain aspects of the temporal correlation of scintillation intensity between the two beacons. It seems, from a visual and quantitative analysis, that large turbulent areas pass through both links, giving a very similar bulk effect in both cases and a small temporal delay, in some periods, is due to the internal structure of these large areas (some inner areas with less turbulence). It may not be unrelated to the observations, the fact that the dominant wind direction is nearly perpendicular to the line joining the intersections of the links with the turbulent layer.

The analysis of a new year of data, whose logging was recently concluded, can be very important, mainly, concerning the extraction of the roll-off factor and corner frequency at Ka-band. Mainly, due to the better CNR (that has been improved), more significant scintillation events can be identified and the extraction of the parameters of the spectrum, in this band, can be enhanced. Also, probably it is recommended a more versatile definition of the frequency ranges, using distinct values for the Ka and Q bands, in order to get the asymptotes.

Also, low-pass filtering the scintillation signal, at least at Ka-band, with a cutoff frequency of 2 Hz or even a lower frequency is recommended to get a lower spectrum floor (in fact, at this frequency, it seems there is no more signal power in the spectrum).

Bibliography

[1] F. Jorge, "Separação das contribuições de chuva e gelo para o XPD na banda Ka," 2012.

[2] C. Ahrens, *Essentials of Meteorology: An Invitation to the Atmosphere*. Chapman & Hall, 1995.

[3] ESA. Satellite frequency bands - Telecommunications. [Online]. Available: https://www.esa.int/Our_Activities/Telecommunications_Integrated_Applications/Satellite_frequency_bands

[4] B. G. Evans, "The role of satellites in 5G," in *2014 7th Advanced Satellite Multimedia Systems Conference and the 13th Signal Processing for Space Communications Workshop (ASMS/SPSC)*. IEEE, sep 2014, pp. 197–202. [Online]. Available: http://ieeexplore.ieee.org/document/6934544/

[5] Y. Niu, Y. Li, D. Jin, L. Su, and A. V. Vasilakos, "A survey of millimeter wave communications (mmWave) for 5G: opportunities and challenges," *Wireless Networks*, vol. 21, no. 8, pp. 2657–2676, nov 2015. [Online]. Available: http://link.springer.com/10.1007/s11276-015-0942-z

[6] A. I. Sulyman, A. T. Nassar, M. K. Samimi, G. R. Maccartney, T. S. Rappaport, and A. Alsanie, "Radio propagation path loss models for 5G cellular networks in the 28 GHZ and 38 GHZ millimeter-wave bands," *IEEE Communications Magazine*, vol. 52, no. 9, pp. 78–86, sep 2014. [Online]. Available: http://ieeexplore.ieee.org/document/6894456/

[7] P. Sobieski, A. Latoux, and G. Brusaard, "Results of the European Space Agency OTS Propagation Campaign," in *14th European Microwave Conference, 1984*. IEEE, oct 1984, pp. 129–134. [Online]. Available: http://ieeexplore.ieee.org/document/4132023/

[8] B. Arbesser-Rastburg and A. Paraboni, "European research on Ka-band slant path propagation," *Proceedings of the IEEE*, vol. 85, no. 6, pp. 843–852, jun 1997. [Online]. Available: http://ieeexplore.ieee.org/document/598408/

[9] A. Paraboni, G. Masini, M. Mauri, R. Polonio, and C. Riva, "Summary of propagation results obtained in 5 years of ITALSAT experiment in Milano," *International Journal of Satellite Communications*, vol. 17, no. 2-3, pp. 169–175, 1999.

[10] ITU-R, "The radio refractive index : its formula and refractivity data," *ITU-R*, vol. 10, pp. 453–10, 2012.

[11] H. Sizun, *Radio Wave Propagation for Telecommunication Applications.* France Télécom Recherche et DéveloppementBelfortFrance: Springer, Berlin, Heidelberg, 2005, vol. 136, no. 1. [Online]. Available: https://link.springer.com/book/10.1007/b137896

[12] L. J. Ippolito Jr., *Satellite communications systems engineering: atmospheric effects on satellite link design and performance.* John Wiley & Sons Ltd Registered, 2008.

[13] M. Tahir, Y. Piao, M. Aslam, and A. Rahim, "Tropospheric scintillation estimation using 10 years meteorological data," *China Communications*, vol. 12, no. 3, pp. 43–49, 2015.

[14] S. A. Borgsmiller, "Effects of Atmospheric Scintillation in Ka-Band Satellite Communications," Ph.D. dissertation, Georgia Institute of Technology, 1998. [Online]. Available: borgsmiller.net/scott/docs/thesis.pdf

[15] R. Stull, *Practical Meteorology - An Algebra-based survey of atmospheric science.* The University of British Columbia, jan 1858, vol. v1.02b.

[16] K. H. Shakthi Murugan and M. Sumathi, "Millimetre Waves over Free Space Optics System for 5G Application," *J. Opt. Commun.*, pp. 1–5, 2018.

[17] T. Bergeron, "On the Physics of Fronts," *Bulletin of the American Meteorological Society*, vol. 18, no. 9, pp. 265b–275, sep 1937. [Online]. Available: http://journals.ametsoc.org/doi/10.1175/1520-0477-18.9.265b

[18] A. D. Panagopoulos, P.-D. M. Arapoglou, and P. G. Cottis, "Satellite Communications At KU, KA, ans V Bands: Propagation Impairments And Mitigation," *Communications*, vol. 6, no. 3, pp. 2–14, 2004.

[19] G. Gallinaro, A. Vernucci, and C. Moreau, "Protocols and Signalling for Fade Mitigation Techniques (FMT) in DVB-RCS Multi-beam Systems," European Space Agency, Tech. Rep., 2005. [Online]. Available: http://emits.sso.esa.int/emits-doc/ESTEC/AO-1-5331-RD2.pdf

[20] M. Evans, "Measurement of the tropospheric scintillation decorrelation scale-length at millimetre wave frequencies," *11th Int. Conf. Antennas Propag.*, no. 480, pp. 825–829, 2005.

[21] E. Vilar, P. Lo, J. Haddon, and T. Moulsley, "Measurement and modelling of amplitude and phase scintillations in an Earth–space path," *J. Inst. Electron. Radio Eng.*, vol. 55, no. 3, p. 87, 2010.

[22] C. Riva and M. Rytir, "Step-by-step procedure to extract scintillation from total or excess attenuation time series," Politecnico di Milano andNorwegian Defence Research Establishment, Tech. Rep., 2016.

[23] G. Brussaard and P. A. P. A. Watson, *Atmospheric modelling and millimetre wave propagation.* Chapman & Hall, 1995.

[24] G. Mie, "Beiträge zur Optik trüber Medien, speziell kolloidaler Metallösungen," *Annalen der Physik*, vol. 330, no. 3, pp. 377–445, 1908.

[25] A. Ishimaru, *Wave propagation and scattering in random media.* Academic Press, 1978.

[26] C. Ho and A. Wheelon, "Amplitude Scintillation due to Atmospheric Turbulence for the Deep Space Network," *Interplanet. Netw. Prog. Rep.*, vol. 42-158, pp. 1–21, 2004. [Online]. Available: https://ntrs.nasa.gov/search.jsp?R=20040095332

[27] N. Tikhonov, M. A. Vorontsov, and G. Carhart, "Characterization of optical turbulence (Cn2) data measured at the ARL A_LOT facility," *Inf. Sci. (Ny).*, no. September, 2005.

[28] H. O. Ka-Leung, "Atmospheric millimetre wave propagation thesis presented for examination for the degree of PhD in the University of London." Ph.D. dissertation, University College London, 1977. [Online]. Available: http://discovery.ucl.ac.uk/1349341/1/459411.pdf

[29] E. Vilar and J. Haddon, "Measurement and modeling of scintillation intensity to estimate turbulence parameters in an Earth-space path," *IEEE Trans. Antennas Propag.*, vol. 32, no. 4, pp. 340–346, 2004.

[30] R. Cole, K. HO, and N. D. Mavrokoukoulake, "The Effect of the Outer Scale of Turbulence and Wavelength on Scintillation Fading at Millimeter Wavelengths," *IEEE Transactions on Antennas and Propagation*, vol. 26, no. 5, pp. 712–715, 1978.

[31] CCIR, "Recommendations and reports of the CCIR," International Radio Consultative Committee, Tech. Rep., 1986.

[32] C. Riva and F. S. Marzano, "Scintillation modelling : a review abstract," *Cost 280, PM4002*, pp. 1–25, 2002.

[33] M. Touw, S and Herben, "Short-term frequency scaling of clear-sky and wet amplitude scintillation," *IEE Proc-Microw. Antennas Propag*, vol. 143, no. 6, 1996.

[34] C. Riva, A. Rocha, F. Jorge, and S. Mota, "Report on the statistical analysis of propagation measurements," Tech. Rep., 2016.

[35] M. M. Van De Kamp, J. K. Tervonen, E. T. Salonen, and J. Pedro V Polares Baptista, "Improved models for long-term prediction of tropospheric scintillation on slant paths," *IEEE Trans. Antennas Propag.*, vol. 47, no. 2, pp. 249–260, 1999.

[36] F. Cuervo, K. Plimon, L. Castanet, X. Boulanger, C. Riva, L. Luini, P. Dvorak, J. Riera, P. Garcia, G. Siles, A. Rocha, F. Jorge, and S. Mota, "Development of high order propagation models for multimedia satellite communications systems report on the statistical analysis," ESTEC, Tech. Rep., 2016.

[37] A. Savvaris, C. N. Kassianides, and I. E. Otung, "Observed effects of cloud and wind on the intensity and spectrum of scintillation," *IEEE Trans. Antennas Propag.*, vol. 52, no. 6, pp. 1492–1498, 2004.

[38] M. M. Van De Kamp, C. Riva, J. K. Tervonen, and E. T. Salonen, "Frequency dependence of amplitude scintillation," *IEEE Trans. Antennas Propag.*, vol. 47, no. 1, pp. 77–85, 1999.

[39] M. van de Kamp, "Asymmetric signal level distribution due to tropospheric scintillation," *Electron. Lett.*, vol. 34, no. 11, p. 1145, 2002.

[40] E. Matricciani and C. Riva, "18.7 GHz tropospheric scintillation and simultaneous rain attenuation measured at Spino d'Adda and Darmstadt with Italsat," *Radio Sci.*, vol. 43, no. 1, pp. 1–13, 2008.

[41] T. J. Moulsley and E. Vilar, "Experimental and Theoretical Statistics of Microwave Amplitude Scintillations on Satellite Down-Links," *IEEE Trans. Antennas Propag.*, vol. 30, no. 6, pp. 1099–1106, 1982.

[42] P. Banjo and E. Vilar, "Measurement and Modeling of Amplitude Scintillations on Low-Elevation Earth-Space Paths and Impact on Communication Systems," *IEEE Trans. Commun.*, vol. C, no. 8, pp. 774–780, 1986.

[43] J. W. Strohbehn, T.-i. Wang, and J. P. Speck, "On the probability distribution of line-of-sight fluctuations of optical signals," *Radio Sci.*, vol. 10, no. 1, pp. 59–70, 1975.

[44] M. M. J. L. van de Kamp, *Climatic Radiowave Propagation Models for the design of Satellite Communication Systems*, Eindhoven, 1999, no. november.

[45] P. Series, "ITU-R P.618-10 Propagation data and prediction methods required for the design of Earth-space telecommunication systems," *Itu-R*, vol. 13, 2009.

[46] I. E. Otung, "Prediction of Tropospheric Amplitude Scintillation on a Satellite Link," *IEEE Trans. Antennas Propag.*, vol. 44, no. 12, pp. 1600 – 1608, 1996.

[47] S. Ventouras, F. P. Fontan, A. Rocha, F. Jorge, A. Z. Papafragkakis, A. D. Panagopoulos, C. I. Kourogiorgas, D. D. Vanhoenacker, A. Graziani, and A. Martelucci, "Large Scale Assessment of Ka/Q band atmospheric channel across Europe with ALPHASAT TDP5: A new propagation campaign," in *2016 10th European Conference on Antennas and Propagation, EuCAP 2016*. Davos, Switzerland: IEEE, apr 2016, pp. 1–5. [Online]. Available: http://ieeexplore.ieee.org/document/7481979/

[48] F. D. Cola, A. Pandolfi, G. D. Paolo, T. Alenia, J. R. Castro, E. Benzi, A. Martellucci, M. Schmidt, J. Ebert, F. Cuervo, S. Falzini, E. Coviello, E. D. Viti, C. Riva, and G. Codispoti, "Alphasat Aldo Paraboni Mission: IOT Campaign Execution and Results," in *Proceedings of the 20th Ka- and Broadband Communications, Navigation and Earth Observation Conference*, no. October 2013, 2014, pp. 89–98.

[49] S. Ventouras, R. Reeves, E. Rumi, F. P. Fontan, F. Machado, V. Pastoriza, A. Rocha, S. Mota, and F. Jorge, "Large Scale Assessment of Ka / Q Band Atmospheric Channel Across Europe with ALPHASAT TDP5 : The Augmented Network," in *European Conference on Antennas and Propagation*, 2017, pp. 1–5.

[50] F. Jorge, C. Riva, and A. Rocha, "Physical Methods for the Separation of the Contributions to the Earth-Space Cross-Polarization Discrimination Using Single-Polarized Satellite Beacon Signals," *IEEE Transactions on Antennas and Propagation*, vol. 66, no. 12, pp. 6510–6524, dec 2018. [Online]. Available: https://ieeexplore.ieee.org/document/8368147/

[51] A. Rocha, S. Mota, L. Cupido, and F. Jorge, "Affordable Programmed Satellite Pointing System for Propagation Experiments," *IEEE Transactions on Instrumentation and Measurement*, pp. 1–1, 2019. [Online]. Available: https://ieeexplore.ieee.org/document/8746805/

[52] A. Rocha, T. Pereira, S. Mota, and F. Jorge, "Alphasat experiment at Aveiro," in *2016 10th European Conference on Antennas and Propagation (EuCAP)*. IEEE, apr 2016, pp. 1–5. [Online]. Available: http://ieeexplore.ieee.org/document/7482017/

[53] J. R. O. Flávio, "Ferramenta de Pré-Processamento e Análise de Dados de Propagação Terra-Satélite nas Bandas Ka e Q," p. 108, 2016.

[54] J. L. Devore, *Probability and Statistics for Engineering and the Sciences*, 8th ed., C. Learning, Ed. California Polytechnic State University, San Luis Obispo: Richard Stratton, 2012.

Appendix A

Paper submitted to ITU Journal: ICT Discoveries - *Special issue on* "Propagation modelling for advanced future radio systems - Challenges for a congested radio spectrum", *under review*

A QUICK OVERVIEW OF A NEW SCINTILLATION DATABASE

Ana Pinho, Susana Mota, Armando Rocha
Departamento de Electrónica, Telecomunicações e Informática/Instituto de Telecomunicações, Universidade de Aveiro, Campus Universitario Santiago 3810 193, Portugal

Abstract *– This paper explores a new Ka and Q-band dry scintillation database and ancillary meteorological data collected at Aveiro, Portugal in two converging Earth-satellite propagation paths and frequencies. The measurement equipment, the parameters of both links and the processing procedure of the database are described first. The dependencies of the hourly averaged scintillation standard deviation with respect to several meteorological parameters, measured at the ground level, and with respect to the wet refraction index are analyzed. The diurnal variation of the hourly averaged scintillation standard deviation –in a monthly and yearly basis- is explored. The yearly amplitude distributions –fades and enhancements- are presented and compared against some available models. The scatter plot of the concurrent hourly averaged scintillation standard deviation is analyzed and a frequency scaling factor derived tentatively.*

Keywords – Scintillation, modelling, diurnal variability.

1. INTRODUCTION

A microwave signal crossing the atmosphere is subject to several impairments such as attenuation, depolarization and scintillation. The scintillation is caused by the scattering of tiny atmospheric refractive index irregularities in turbulent layers that evolves over time and drift through the propagation path carried by the wind. The phase and amplitude distorted wave front is integrated by the receiving antenna aperture giving rise to the more often observed signal amplitude fluctuations around a mean value computed typically in 1-minute to 5-minutes.

The modelling of scintillation is important because it can disturb the fade mitigation systems and the scintillation fades can impact the availability of terminals with very small fade margins.

Scintillation long term data at Q-band and databases collected with concurrent satellite links are yet relatively scarce in the literature.

2. EXPERIMENTAL SCENARIO

Two propagation experiments have been active at our site: one using the Ka-Sat satellite Ka-band beacon at 19.68 GHz and another one with the Alphasat satellite Q-band beacon at 39.402 GHz. More information can be found at [1]. The receivers are fully independent: they do not share any hardware.

The general characteristics of the links are given in the following table: where the CNR_0 (dB-Hz) is the carrier to noise spectral density ratio in clear sky.

Table 1 - Ka and Q-band receiver characteristics

Parameter	Ka-Band	Q-band
Antenna Diameter (m)	1.50	0.62
Elevation(º)	39.63	31.9
Azimuth (º)	153.95	134.6
CNR_0 (dB-Hz)	57.7	53.0
Polarization Quasi-V (º): tilt angle	19.5	12.3

The site coordinates are 40^0 37´ N and 8^0 39' W being the Q-band receiver about 3 m bellow the Ka-band receiver (in an office bellow the roof). The angular aperture between the two links is about 17^0. Recently the K-band receiver front-end was refurbished and the CNR_0 has been improved by about 4 dB. A small meteorological station is also co-sited and measures temperature, relative humidity, rain rate, wind speed and atmospheric pressure.

Q-band beacon data is logged by a *MATLAB* application to a set of files and the Ka-band beacon and meteorological data are logged by a *Labview* application to another set of files. The beacon data copolar amplitude time series are stored at a sampling rate of 8 S/s.

3. DATA ANALYSYS

The raw experimental data is loaded together and pre-processed by a dedicated tool to perform the pre-processing [2]. This step aims to check the quality of the data and to derive the attenuation by using the measured copolar levels and the estimated copolar levels that would be observed in the absence

of attenuation. All the pre-processed time series are stored in a single day file.

For the scintillation analysis, first, the pre-processed data files are loaded and the scintillation time series is obtained by a high pass filter, based on raised cosine filter with a 0.025 Hz cut-off frequency. Then, the wet refractivity, N_{wet}, is calculated using the temperature, T(ºC), relative humidity, H(%), and pressure, P (hPa), all integrated with a 10 minutes integration time, according [3]:

$$N_{wet} = 72\frac{e}{T+27} + 3.75x10^5\frac{e}{(T+273)^2} \quad (1)$$

The water vapour pressure, e, is related with H by

$$e = \frac{e_s H}{100}\ (\text{hPa}) \quad (2)$$

The water vapour saturation pressure, e_s, can be calculated from the temperature and the pressure but the equations, also found at [3], are omitted here for brevity.

The scintillation variance is calculated in a one-minute non-overlapping time windows. Finally, the scintillation and meteorological data time series are stored in separate files. Statistical data on scintillation parameters is derived by dedicated tools that have been developed in *MATLAB*.

It must be pointed out that, due to the finite CNR_0, the gaussian noise introduces a bias on the scintillation variance, given by [4]:

$$\sigma_n^2 = 75.44x10^{-\frac{CNR-10log_{10}(8)}{10}}\ (\text{dB}^2) \quad (3)$$

where 8 is the sampling bandwidth. The calculations, using the values found in Table 1, gives respectively, 0.0010 e 0.003 dB² for the Q-band and Ka band.

The measured variance, σ_m^2, is related to the atmospheric induced variance, σ_{atm}^2, by the equation:

$$\sigma_m^2 = \sigma_{atm}^2 + \sigma_n^2\ (\text{dB}^2) \quad (4)$$

From this point on, the variance (or standard deviation) presented through the paper, are the measured one.

4. RESULTS AND ANALYSYS

The scintillation is usually characterized by the distribution of the amplitude, χ (dB), or by the standard deviation, σ_χ, computed in the aforementioned time window. This last one is often calculated only for dry periods, i.e., so the periods with attenuation larger than 0.5 dB were excluded from the statistical calculations.

4.1 Meteorological dependencies

The joint distributions of the hourly averaged scintillation standard deviation and meteorological parameters were calculated. The following plots, Fig. 1 to Fig. 3, were obtained by calculating the decimal logarithm of the normalized histogram and the contour lines are logarithmically spaced.

Fig. 1 presents the Q-band scintillation standard deviation versus the atmospheric pressure. The higher the pressure the lower the scintillation variance. High pressure means usually clear sky, dry and stable weather: conditions that are not prone to atmospheric instability. As we can see the higher the scintillation standard deviation is, the more sensitive to the pressure. In the following pictures, the scintillation variance ground floor is above the expected minimum value, therefore, a residual scintillation is always present. The hourly correlation between the two-time series is already not negligible. A similar plot is obtained for the Ka-band.

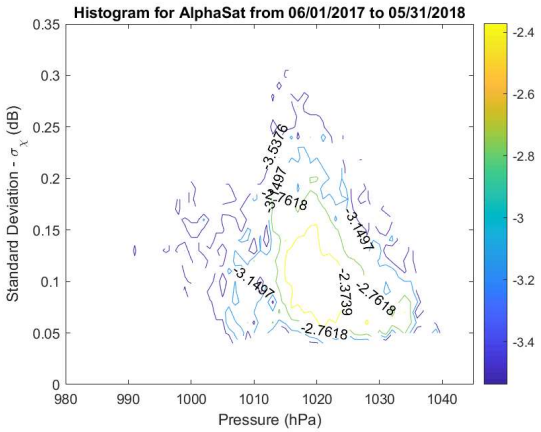

Fig. 1 – Scintillation standard deviation at Q-band versus atmospheric pressure

Fig. 2 shows the scintillation standard deviation at Ka-band versus N_{wet}. As we can see, there is also a clear with N_{wet}: the higher the wet refractive the higher the scintillation standard deviation. The N_{wet} parameter, averaged in a long term basis, has been used to model de distribution of the scintillation standard deviation[5]–[7].

Fig. 3 depicts the scintillation standard deviation at the Q-band versus temperature. There is a clear trend that shows the effect of the temperature: the higher the temperature the higher the scintillation standard deviation. That is higher temperatures are associated with increased atmospheric instability. Exactly the same trend is observed at Ka-band (not

depicted).

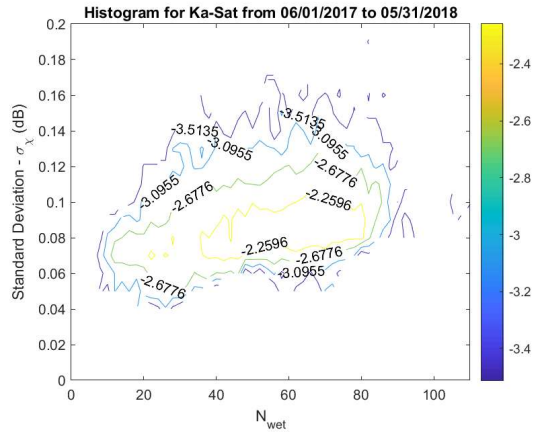

Fig. 2 – Standard deviation at Ka-band versus Nwet

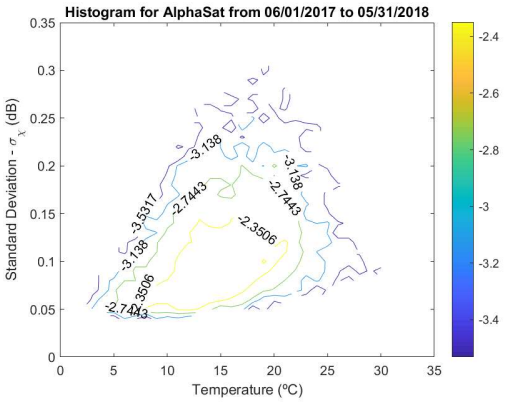

Fig. 3 – Standard deviation at Q-band versus temperature

The correlation of the standard deviation with the several meteorological related variables is summarized in Table 2.

Table 2 – Correlation between scintillation standard deviation and meteorological parameter

Meteorological parameter	Correlation Ka-band	Correlation Q-band
Pressure (mB)	-0.31	-0.29
Nwet	0.33	0.34
Temperature (ºC)	0.34	0.36
Water vapour (g/m^3)	0.33	0.35
Relative humidity	0.14	0.12

The most uncorrelated variable is the relative humidity. The variables N_{wet}, temperature and water vapour content have similar correlations being the corresponding correlations at Q-band slightly higher. The models usually use longer averaged meteorological parameters as input data, however, a noticeable correlation is observed already with hourly data. The Ortgies-T model proposal seems to deserve attention as the correlation of the standard deviation with temperature is similar to that of the usually used N_{wet} as a modelling parameter.

4.2 Diurnal variation

The diurnal variation of the standard deviation (the time is given in UTC) has been calculated in a monthly and yearly basis. The trend is the same along all months with somewhat more striking diurnal variations during the months with average higher temperatures.

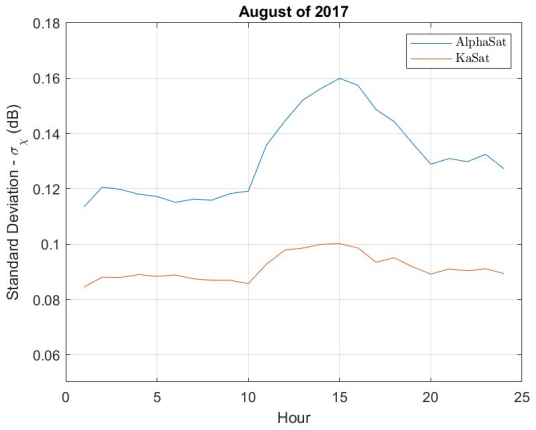

Fig. 4 – Month averaged diurnal variation of the Q and Ka band scintillation standard deviation: August

The most scintillating periods of the day are from 10am to 8pm as can be observed in Fig. 4: this latter hour occurs a little bit earlier during winter.

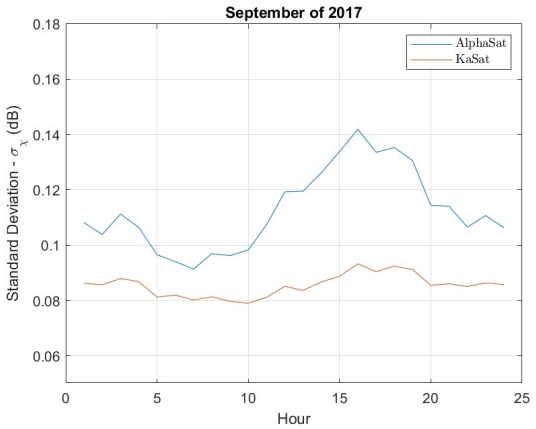

Fig. 5 – Month averaged diurnal variation of the Q and Ka band scintillation standard deviation: September

Often higher scintillation periods, however not as intense as those of the afternoon, also occurs close to the midnight –usually after- as it can be observed in Fig. 5. The lowest scintillation periods occur from 5am to 9am and 10pm to 11pm. Some turbulent

processes must be occurring in the atmosphere between the more quite end of the day and the early morning. The day variations are very similar at both frequencies as can be easily observed.

Lowest scintillation periods occur during the coldest months with clear sky, foggy weather, very dry periods (even windy ones) and also very weak – drizzle- and long lasting rain. The worst and most sustained periods scintillation periods occur during uniform cloud cover and hot weather, not necessarily leading to rain. Burst scintillation periods are observed during showery weather with dense and sparse clouds: often a rain shower is preceded by an increased scintillation period that is probably due to turbulence in developing rain cells caused by air masses down/updrafts and shear winds.

4.3 Distribution of fades and enhancements

The monthly distribution of the scintillation amplitude enhancements, χ^+ (dB), and fade depth, χ^-, for a full year are depicted in Fig. 6 and Fig. 7 for the Q-band.

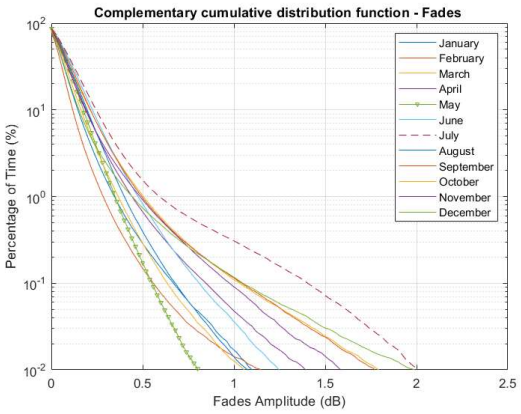

Fig. 6 – Monthly cumulative distributions of the fades for the Q-band

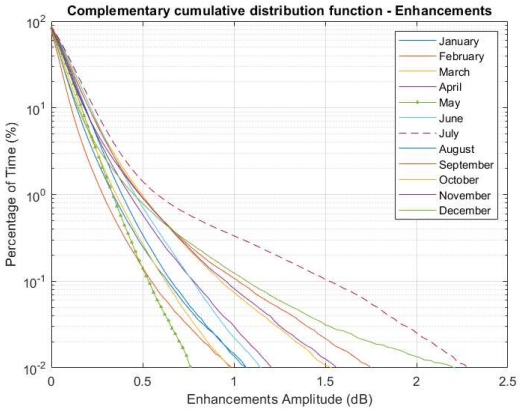

Fig. 7 – Monthly cumulative distributions of the enhancements for the Q-band

As discussed in [4] for the same probability the fades are, in general, deeper than the enhancements. However, in spite of being true along an average year, the difference is very small and it is not verified all the months.

There is a significant variability of the cumulative distributions from month to month but there is no clear distinction between late spring, summer and early fall from the other periods. Higher temperatures but clear sky and higher pressures are balanced by lower temperature but often cloudier conditions during the other periods. That is: the seasonality is not so acute as with rain attenuation.

4.4 Concurrent standard deviation at the two bands

As described above the two converging links have an angular difference of about 17º and the distance between the points where the links cross a plane at 1000 m altitude is several hundreds of meters. A very high correlation between the scintillation variance at the two frequencies has been always observed, meaning that the turbulent volumes must be present over very large distances.

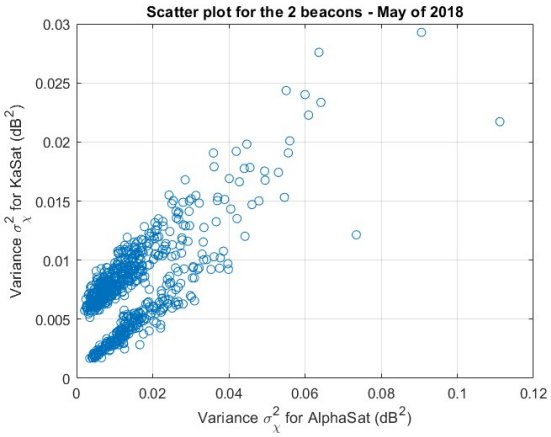

Fig. 8 – May 2018 scatter plot of the hourly averaged scintillation variance at the two frequencies

Fig. 8 depicts the high correlation mentioned above, with the peculiarity that the Ka-band receiver has been upgraded during this month: for the last 10 days of the month an higher CNR_0 was already available. It is notorious the presence of two data sets being the lower set collected already with the better CNR_0 (estimated to be about 4 dB).

The annual scatter plot results presented in Fig. 9 show the high correlation between the two vari-

ances that was, nevertheless, expected from the diurnal variation discussion in section 3. The obtained annual correlation was 0.772 and is quite similar throughout all the months.

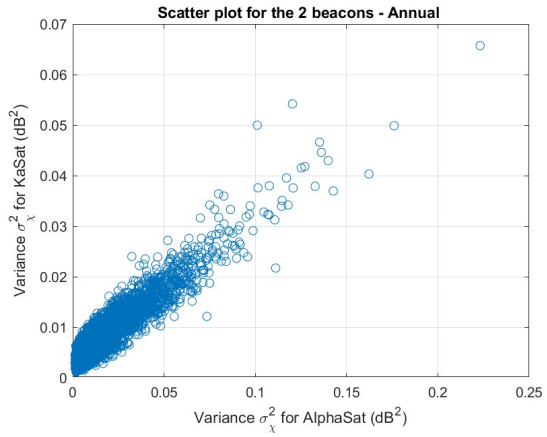

Fig. 9 – Year scatter plot of the hourly averaged scintillation variance at the two frequencies

A frequency scaling factor for the variance was estimated, for example for the April data depicted in Fig. 10, by performing a linear fitting to the variances scatter plot. A value of 0.288 was obtained for the slope that is very close to the variance scaling factor obtained by using the frequencies, elevation angles and antenna reduction factors that can be found in several models.

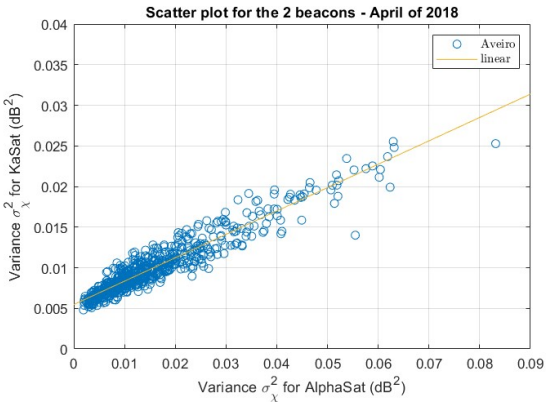

Fig. 10 – A month scatter plot of the variance at the two bands and a linear fitting to the data

5. SCINTILLATION MODELS

A few essays of some available scintillation models has been performed such has the scintillation fades and enhancements using the Otung [7], ITU [8] (only for fades), van de Kamp [9] and the Karasawa [5] models. Fig. 11 and Fig. 12 were obtained for the Ka-band using the year averaged N_{wet}=51.5, the antenna variance averaging factors of about 0.86 and 0.95 (respectively for the Ka and Q-band) both computed for a turbulent layer height as recommended in the corresponding model and, finally, assuming the antennas efficiency of 60%. The water liquid content used for the van de Kamp model was 1 kg/m^2. The data here presented corresponds to a full year: from 1/6/2017 to 31/05/2018.

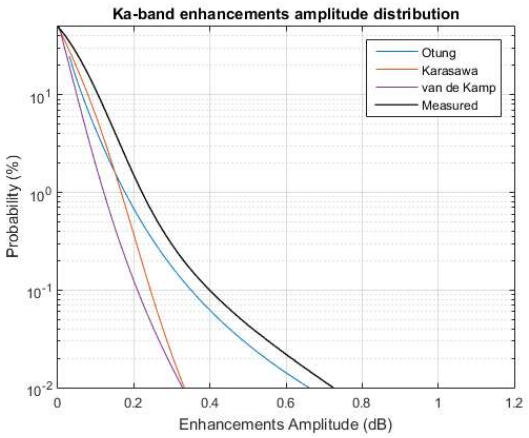

Fig. 11 – Cumulative distribution of the enhancements at Ka-band and the predictions of the models for one year

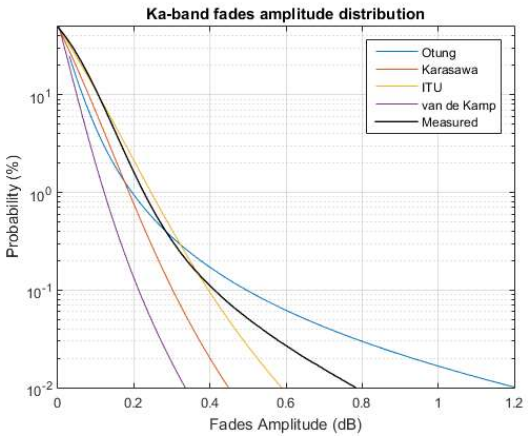

Fig. 12 – Cumulative distribution of the fades at Ka-band and the predictions of the models for one year:

The Otung model seems to give the better predictions for the enhancements while the van de Kamp and Karasawa models under predicts both the fades and enhancements. The ITU models performs reasonably well with the fades.

The performance of the available models will be systematically evaluated in future work.

6. CONCLUSION

A scintillation database has been collected at Aveiro, Portugal. In spite of an already existing database at Ka-band, the new one now comprises the Q-band.

The experimental conditions were described in detail to understand the potentials and limitations of the database.

The correlation of the hourly averaged scintillation standard deviation and local meteorological data has been analyzed. A positive correlation was found with ambient temperature and the water vapour density and a negative one with the atmospheric pressure.

The diurnal variation is more observable during the summer months and the scintillation is more intense from 10am to 8am. The monthly fade and enhancements distributions show a significant variability. There is a high correlation between the hourly scintillation variance at the two frequencies in spite of the angular separation of the two links.

The variance frequency scaling seems to be well described by the theory. The best fade and enhancements model to describe the experimental data seems to be the Otung one.

ACKNOWLEDGEMENT

This work was developed in the framework of the European Space Agency (ESA) funded project Large Sale Assessment of Ka/Q Band Atmospheric Channel Using the Alphasat TDP5 Propagation Beacons, ESA ITT AO/1-7963/14/NL/LvH.

The authors are grateful to ESA and ESA Technical Officer, Dr. Antonio Martelluci for funding the refurbishment of the Ka-band terminal front-end at our site which extends significantly the dynamic range of the receiver.

REFERENCES

[1] A. Rocha, T. Pereira, S. Mota, and F. Jorge, "Alphasat experiment at Aveiro," *2016 10th Eur. Conf. Antennas Propagation, EuCAP 2016*, pp. 3–7, 2016.

[2] J. Flávio, A. Rocha, S. Mota, and F. Jorge, "Alphasat Experiment at Aveiro : Data Processing Approach and Experimental Results," in *European Conference on Antennas and Propagation*, 2017, pp. 2376–2380.

[3] Rec ITU-R P.453-13, "The radio refractive index : its formula and refractivity data P Series Radiowave propagation," vol. 13, 2017.

[4] M. M. J. L. van de Kamp, "Climatic Radiowave Propagation Models for the design of Satellite Communication Systems," Eindhoven University of Technology, 1999.

[5] Y. Karasawa, M. Yamada, and J. E. Allnutt, "A new prediction method for tropospheric scintillation on Earth-space paths," *IEEE Trans. Antennas Propag.*, vol. 36, no. 11, pp. 1608–1614, 1988.

[6] M. M. J. L. Van De Kamp, C. Riva, J. K. Tervonen, and E. T. Salonen, "Frequency dependence of amplitude scintillation," *IEEE Trans. Antennas Propag.*, vol. 47, no. 1, pp. 77–85, 1999.

[7] I. E. Otung, "Prediction of tropospheric amplitude scintillation on a satellite link," *IEEE* Transactions *on Antennas and Propagation*, vol. 44, no. 12. pp. 1600–1608, 1996.

[8] Rec ITU-R P.618-13, "Propagation data and prediction methods required for the design of Earth-space telecommunication systems," 2009.

[9] M. M. J. L. van de Kamp, "Asymmetric signal level distribution due to tropospheric scintillation," *Electron. Lett.*, vol. 34, no. 11, p. 1145, 1998.